NUMERICAL INVESTIGATIONS ON THE USE OF MULTI-ELEMENT BLADES IN VERTICAL-AXIS WIND TURBINES

A Dissertation
Presented to
The Academic Faculty

by

Elhadji Alpha Amadou BAH

In Partial Fulfillment
of the Requirements for the Degree
Doctor of Philosophy in the
School of Aerospace Engineering

Georgia Institute of Technology
May, 2015

NUMERICAL INVESTIGATIONS ON THE USE OF MULTI-ELEMENT BLADES IN VERTICAL-AXIS WIND TURBINES

Approved by:

Dr. Lakshmi N. SANKAR, Advisor
School of Aerospace Engineering
Georgia Institute of Technology

Dr. Daniel SCHRAGE
School of Aerospace Engineering
Georgia Institute of Technology

Dr. Jeff JAGODA
School of Aerospace Engineering
Georgia Institute of Technology

Dr. Samuel SHELTON
Strategic Energy Institute
Georgia Institute of Technology

Dr. Mark COSTELLO
School of Aerospace Engineering
Georgia Institute of Technology

Date Approved: December 05, 2014

I begin with the name of God, the most Gracious, the most Merciful.

… Indeed He is a servant grateful and thankful. – ***Quraan 17:3***

To my beloved Mother, Fatoumata Binta BAH,
May the Almighty admit you in His Divine and Eternal Mercy.
To my entire family.

And your Lord has decreed that you worship not except Him and to the parents good treatment. If one or both of them reach old age [while] with you, say not to them [so much as] "uff" (a word of disapproval or irritation) and do not repel them and speak to them a noble word. – ***Quraan 17:23***
And lower to them the wing of humility out of mercy and say, "My Lord, have mercy upon them as they brought me up [while I was] small." – ***Quraan 17:24***

And We have enjoined upon man good treatment to his parents. His mother carried him with hardship and gave birth to him with hardship, and his gestation and weaning [period] is thirty months. [He grows] until, when he reaches maturity and reaches [the age of] forty years, he says, "My Lord, enable me to be grateful for Your favor which You have bestowed upon me and upon my parents and to work righteousness which You approve and make righteous for me my offspring. Indeed, I have repented to You and indeed, I am of the Muslims." – ***Quraan 46:15***

ACKNOWLEDGEMENTS

The Ultimate Praises belong to The Originator and Sustainer of all that exists. Peace and Blessings, words of salutation to the servants of His. May His Peace and Blessing be upon the servants of His. Peace and Blessings, words of salutation for the servants of His. May His Mercy be upon the servants of His. May us be among them.

Thereafter I wish to express my profound gratitude and thanks to my advisors Prof. Lakshmi Sankar and Prof. Jeff Jagoda for their support and guidance. It has taken them a great deal of patience to get me on orbit. The best word is the word of God. With the lack of sufficient words to say "thanks," I ask the The All-Knowing to reward them with the best that only He can reward with. It has been a great honor and pleasure to work under their supervision. They have always made themselves available to answer all questions and solicitations and provide the best support and guidance. I include in these words of thanks Prof. Mark Costello, who served on the proposal and defense committees as well as Prof. Daniel Schrage and Prof. Sam Shelton who served on the defense committee. I also thank my colleagues, past and present, and friends for their help. Just to name a few: Dr. Matthieu Masquelet, M. Balaji Muralidharan, Dr. Ritu Marpu, M. Jeewoong Kim, Miss Eliya Wing, M. Muhammad Ali, M. Liu Zhang, Miss Chong Zhou, Dr. Safayet Ahmed, Dr. Shahnewaz Siddique, M. Talha Khan, the list goes on and on. The community around the AlFarooq Masjid has been a great benediction and a source of comfort. I am grateful to everyone from the imams to other Brothers and Sisters for their invaluable contributions to make this place a real Piece of Heaven on Earth.

The School of Aerospace Engineering, administration and staff, contributes to sustaining a good working environment. These efforts are greatly appreciated.

Finally, should there be an earthly Paradise, it would be with those dearest to me. To my family at large, my love and gratitude go to you for all that words cannot express. God Bless you. May He grant us the best of this world and the best of the hereafter.

It goes without saying that good days and difficult times have come to pass. The most difficult of all is the departing of my Mother. To God belong who He has taken back to Him, to Him belong those yet but surely to return Him. To God we belong, to Him we shall return. May her new life be a life of rest, a life filled with the great promises of her Lord. When the day comes that we are re-united, may it be under the Pleasure and Mercy of the Almighty. Until then, my prayers to God for you, for myself, and for all will be the food for my heart and soul. Sufficient for us is God [Alone] and He is the Best Disposer of affairs.

TABLE OF CONTENTS

LIST OF TABLES

LIST OF FIGURES

LIST OF SYMBOLS AND ABBREVIATIONS

AEP	Annual Energy Production
AoA	Angle of Attack
BEM	Blade Element Moment theory
CFD	Computational Fluid Dynamics
CoE	Cost of Energy
DES	Detached-Eddy Simulations
DMST	Double Multiple Streamtube model
DNS	Direct Numerical Simulations
ECR	Energy Capture Ratio
HAWT	Horizontal-Axis Wind Turbine
LB	Leishman-Beddoes
LES	Large Eddy Simulations
OWC_P	Overall Weibull Power Coefficient
RANS	Reynolds Averaged Navier-Stokes simulations
RE	Renewable Energy
RPM	Revolutions per Minute
SB-VAWT	Straight-Bladed VAWT
SST	Shear Stress Transport
TPES	Total Primary Energy Sources
TSR	Tip Speed Ratio
UAV	Unmanned Aerial Vehicle
URANS	Unsteady RANS
VAWT	Vertical-Axis Wind Turbine

C_D	Drag Coefficient
C_L	Lift Coefficient
C_N	Normal Force Coefficient
C_P	Power Coefficient
C_T	Tangential Force Coefficient
H	Rotor Height
N_b	Number of Blades
P_R	Rated Power
R	Rotor Radius
Re	Reynolds Number
Re_b	Reynolds number based on the blade chord
V, V’	Velocities
Ve	Equivalent Velocity
W	Effective Wind Velocity
c	Blade Chord
f	Transcendental Function
u, u”	DMST Interference Factor
α	Angle of Attack
λ	Tip Speed Ratio
k	Turbulence Kinetic Energy
θ	Azimuth Angle
μ	Dynamic Viscosity
ρ	Density
ω	Turbulence Dissipation Rate
Ω	Rotor Angle Velocity

SUMMARY

The interest in sustainable forms of energy is being driven by the anticipated scarcity of traditional fossil fuels over the coming decades. There is also a growing concern about the effects of fossil fuel emissions on human health and the environment. Many sources of renewable energy are being researched and implemented for power production. In particular, wind power generation by horizontal- and vertical-axis wind turbines is very popular.

Vertical-axis wind turbines (VAWTs) have a relative construction simplicity compared to horizontal-axis wind turbines (HAWTs). However, VAWTs present specific challenges that may hinder their performance. For instance, they are strongly affected by dynamic stall. A significant part of the kinetic energy contained in the oncoming wind is lost in swirl and vortices. As a result, VAWTs have lower power production compared to HAWTs.

First, the present work is aimed at the study of the aerodynamics of straight-bladed VAWTs (SB-VAWTs). Empirical calculations are conducted in a preliminary work. Then a two-dimensional double multiple streamtube (DMST) approach supported by a two-dimensional numerical study is implemented. The dynamic stall and aerodynamic performance of the rotor are investigated. A VAWT-fitted dynamic stall model is implemented. Computational fluid dynamics (CFD) simulations are conducted to serve as reference for the DMST calculations. This three-pronged approach allows us to efficiently explore multiple configurations. The dynamic stall phenomenon is identified as a primary cause of performance loss.

The results in this section validate the DMST model as a good replacement for CFD analysis in early phase design provided that a good dynamic stall model is used.

After having identify the primary cause of performance loss, the goal is to investigate the use to dual-element blades for alleviating the effect of dynamic stall, thereby

improving the performance of the rotor. The desirable airfoil characteristics are defined and a parametric analysis conducted. In the present study the parameters consists of the size of the blade elements, the space between them, and their relative orientation. The performance of the rotor is calculated and compared to the baseline.

The results highlight the preeminence of the two-element configuration over the single-element provided that the adequate parametric study is conducted beforehand.

A performance enhancement is obtained over a large range of tip speed ratios. The starting characteristics and the operation stability are also improved.

Finally, an economic analysis is conducted to determine the cost of energy and thus the financial viability of such a project. The Great Coast of Senegal is selected as site of operation. The energy need and sources of this region are presented along with its wind energy potential. The cost evaluation shows the economic viability by comparing the cost of energy to the current energy market prices.

CHAPTER 1

INTRODUCTION

1.1 Background

Renewable forms of energy have been left out with little or no consideration in the processes of power generation. This neglect was mostly due to the availability of inexpensive fossil fuels. Now with the progressive depletion of these classical fossil fuels, there is a resurgence of interest in sustainable sources of energy. In addition to this, the dependency of developed countries on foreign supply is also of concern because these resources are often located in politically unstable regions, if not countries literally engulfed in civil wars. As for developing countries, they often have great potential for renewable energies and this represents for them a great hope for achieving their endeavors in terms of development. Furthermore, the growing scientific and public awareness of the impact of the fossil fuel emissions on the health and the environment in general is undeniably to be added in the motivating factors. This is further backed by global advocacy to act against climate change. The technological advancements are also making it economically more realistic to invest on the research and development of clean energy solutions. Combinations of these factors and others are stimulating the interest to pursue advanced research in the field of sustainable energy. And the development of the corresponding solutions has substantially progressed in the last decades and the trend is toward pursuing these efforts. Furthermore, economic incentives are put into place to encourage this pursuit and work toward energy independence [44].

Of the renewable energy sources, hydro-electric power production has been around for generations and is still in use. Other forms of sustainable energy productions include geothermal energy, biomass and biofuels, solar energy, hydro-kinetics, and wind power.

An elaborated review and analysis is provided by Freris and Infield in their Renewable Energy in Power Systems [58].

1.2 Wind Turbine Technologies

The wind power generation is one of the renewable energy solutions with a sustained growth. It can be categorized in two technological forms: the Horizontal-Axis Wind Turbines (HAWTs) and the Vertical-Axis Wind Turbines (VAWTs). HAWT technologies are more developed because they have received more attention over the past decades. Efforts in this field include the works under the leadership of Sankar (e.g., [18, 19], [187, 188], and [209-211]), and by Hansen and Butterfield [67]. HAWTs are already being utilized on an industrial scale and the efforts to bring the technology to perfection are also ongoing (e.g., [206], [213], and [214]).

On the other hand, Vertical-Axis Wind Turbines (VAWTs) have been put aside for a long time. Yet the concepts themselves aren't new. Some of them date back to 1891.

HAWTs and VAWTs have each their own unique advantages and disadvantages. In terms of the amount of wind power that can be extracted, highly sophisticated HAWTs can yield up to 50% while VAWTs, on the other hand, are often limited to around 35%. Even though this is but one element of comparison, it obscures the general perception about VAWTs. However, a more meticulous analysis will show that often VAWTs may present advantages over HAWTs. For instance, HAWTs are able to achieve 50% wind power extraction only after incorporation of very sophisticated technologies, such as active blade pitch control and yaw control mechanisms. Advanced blade design with a variation of the section profile, twist, and tapering along the blade span is also necessary for reaching a good performance. Furthermore the yaw control mechanism is not adapted to rapid and/or frequent changes in wind direction while VAWTs operate independently from the direction of the wind. In sum, the HAWT technology is much more complex while VAWTs benefit from their

simplicity. VAWTs also profit from their relatively small sizes and low levels of noise. This makes them suitable for urban and suburban settings, thus cutting the costs related to the transportation. This is the opposite of HAWTs, which tend to be of very large sizes in order to achieve cost advantages, as measured in cents per kilowatt-hour (₵/kWh). For example, a five megawatt turbine has a diameter of about 120 meters [44]. The current trend is toward even larger turbines. These types of machines only fit in remote locations, away from major metropolitan areas.

On the other hand, as was mentioned earlier, VAWTs operation is independent of the wind direction. They come in different sizes and designs that fit in both rural and urban localities. Furthermore, they can be used to exploit the Venturi effect created by city architecture and thus operate even though the average wind speeds are less than that for normal operations. They satisfy the needs of small and relatively large energy consumption markets. They operate at lower tip speed ratios (TSRs) compared to HAWTs and are quieter. For instance, besides the fact that small VAWTs do not have gear boxes, Iida et al. [77] have shown that the aerodynamic noise emitted by VAWTs is at least 10 dB less than that which is generated by conventional HAWTs. The low RPM operation also reduces significantly the risk of avian fatality.

VAWTs also have a simpler design (fixed span, pitch, twist), and, in contrast to HAWTs, their power generation machinery is placed at ground level. The vertical-axis concept may also be oriented upside down, with the power production generator on the top, to make it suitable for operation in rivers and tidal currents. In these configurations, the power generator will be either on ground level or above water, which facilitates the maintenance. More detailed comparisons between the horizontal- and vertical-axis turbines are available in [53], [88], and [143].

The vertical-axis wind turbines can further be classified into two kinds – the Darrieus and Savonius concepts. These are driven by lift and drag forces, respectively.

The simplest Savonius turbines are made of semi-cylindrical barrels pushed by the wind. More advanced designs employ twisted S-like barrel sections. The works pertaining to this concept include [4], [33], and [123]. Savonius systems operate at low TSRs and are often used as measurement devices, although they are far from been restricted to this purpose. Their efficiency is limited to about 25% [91].

The Darrieus devices, on the other hand, are driven by the lift generated by airfoils. The simplest of the Darrieus turbines are made of straight blades (SB-VAWTs) of constant section profile. Also common are the egg-beater rotors with curved or straight blades. Comprehensive reviews of wind power technologies are compiled by Eriksson et al. [53], Balat [13], Ackerman and Soder [1], and Joselin-Herbert et al. [84].

Darrieus and Savonius concepts can be combined to improve the starting operation. This also increases the energy extraction at low TSRs. The blades in both concepts can be twisted for improved performance (eg., [85] and [166]). These hybrid concepts of wind turbines have been investigated by Kyozuka [97] and Wakui [198], among others.

1.3 Flow Physics of VAWTs

The understanding of the dynamics of the flow through the turbine is an important step toward understanding the challenges pertaining to VAWTs. To this effect, a model of straight-bladed vertical-axis wind turbine (SB-VAWT) is adopted.

The very concept of the VAWT yields inherent challenges that may undermine the effectiveness of the power extraction. For instance, as a blade covers a 360 degree cycle, it experiences large variations of its angle of attack particularly at low TSRs. A schematic of the rotor section with the velocity components and the angle of attack is given in Figure 1.1. The very rotation also curves the flow in such a way that the next blade sees a further variation of the effective angle of attack – this phenomenon is particularly important for high solidity rotors. Further, the rotor experiences a highly perturbed flow in its

downstream section as a result of the wake. Indeed, the swirling wake shed by one blade affects the other blades and in certain conditions the same blade at a later time. All this leads to severe dynamic stall, which hinders the performance and contributes to the vibrations and blade fatigue.

Furthermore, much of the incoming wind kinetic energy is lost to the swirling flow that is being generated by both the rotation and the dynamic stall.

All these factors inherent to the VAWT contribute to make them somewhat "less effective" in extracting wind power.

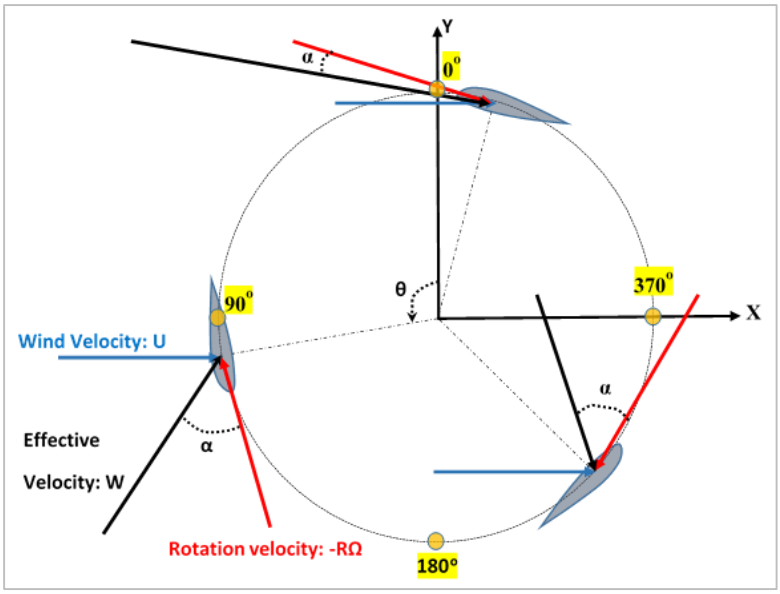

Figure 1. 1: Sketch of an SB-VAWT: Velocity Components

1.4 Literature Survey of Prior Work

In this work we mainly focus on Straight-Bladed Vertical-Axis Wind Turbines (SB-VAWTs). Despite their relative simplicity compared to the HAWTs, their aerodynamics present nonetheless specific challenges to cope with in order to assess and improve their performance. Diverse methodologies have been used to study the aerodynamics and performance of these turbines. The methods include empiricism, analytical and semi-

analytical calculations, numerical tools such as computation fluid dynamics, and experimental investigations in the form of wind tunnel experiments and open-field operation settings. The performance related investigations often deal with the design and geometry where the effects of blade geometry, rotor solidity, and/or blade pitch angle are studied. The effect of quantities such as the Reynolds number are also investigated in connection with the performance studies. During the investigations and design of VAWTs, it is not an understatement to say that the dynamic stall is the one of the most, if not the most, cumbersome challenge to cope with. In fact, this is especially the case because of its inherence to the very concept of the vertical-axis turbine.

While, as mentioned earlier, up until very recently, VAWTs have received little attention compared to HAWTs, there have still been efforts that undertook the challenges described above.

Before elaborating on some of those milestone contributions, it is worthwhile to draw attention to some of the overview and compilation works. In this regard, Ljungstom [110], Eriksson et al. [53], Carrigan [29], and McPhee and Beyene [113] provide comparative analyses of wind energy concepts and lay out the pros and cons of both horizontal- and vertical-axis wind turbines. A similar review was compiled by Khan et al. [88] for hydro-kinetic turbines. In passing, the hydrokinetic and wind turbine technologies follow the same concepts. Differences pertaining, in part, to the structure will only arise as imposed by the medium of operation (air in one case and water in the other). A historical review of wind energy followed by the concepts of vertical-axis turbines is given in the works by D'Ambrosio and Medaglia [39], Islam et al. [79, 81], and Manana [111].

We have emphasized the preponderance of the dynamic stall phenomenon. However, there are also other challenges to deals with. Dabiri et al. [38] describe the opportunities and challenges of wind energy in general and vertical-axis turbines in particular. More exhaustive reviews of the challenges pertaining to VAWTs are given by Islam et al. in [79] and [81]. They are connected to the low Reynolds number operation

that yields a great sensitivity to the flow perturbations and the energy losses associated with the formation of laminar separation bubbles. The large and oscillating angles of attack produce unsteadiness, vibrations, and gust responses that further contribute to the already mentioned dynamic stall. The flow curvature and swirling due to the rotation, the blade-blade-wake interactions, the parasite drag due to the struts and tower, and the turbulent atmospheric conditions add to the list of challenges.

1.4.1 Computational Methodologies

Various approaches have been adopted for either understanding and/or coping with these challenges or computing the loads and performance of the turbines. For instance, empirical or semi-empirical methods have been used for approximating the power output. It is in this framework that Eid et al. [48] and Omijeh et al. [127] used empirical correlations to express the variation of the power coefficients as a function of the tip speed ratio and the blade pitch angle. These authors also studied the dynamics of the electrical system itself. An empirical formulation is also utilized for modeling the dynamic stall, as will be seen in a later section of this chapter.

There also exist analytical and semi-analytical methods. We distinguish in this family mainly the actuator-disc based approaches, the vortex models, and the cascade models.

In the first group, the work by Newman [126] is noticeable as it redefines the Betz theoretical limit for the vertical-axis turbines. The maximum power coefficient that results from this multiple actuator-disc study is given by $C_{p,max} = \frac{8n(n+1)}{3(n+1)^2}$ where n is the number of actuator-discs. This gives a value of $\frac{16}{25}$ for the maximum limit in a two actuator-disc configuration for the vertical-axis turbines as opposed to the classical $\frac{16}{27}$ Betz limit for horizontal-axis turbines. The derivation of the Betz limit is shown in Appendix 2.

In the same family of actuator-disc models, we note the single, multiple, and double multiple streamtube models. The earliest streamtube model is due to Templin [185] who

decomposed the flow into a number of streamtubes in the streamwise direction. The drag and lift of the blade are calculated using static airfoil data. The relative velocity is used to determine the local Reynolds number and the effective angle of attack (AoA) of the blade. The single streamtube model [141] estimates with a relative accuracy the performance for high aerodynamic efficiency rotors (high TSRs) and predicts to some extent the effects of the rotor aspect ratio and solidity. However, it overestimates the performance for low TSRs.

The multiple and double multiple streamtube models are analogous to the Blade Element Momentum (BEM) theory often used in horizontal-axis turbines. In the streamtube models, the induced velocity is determined by equating the time averaged load of the blade with the momentum flux in the direction of the wind [205].

The multiple streamtube model first developed by Wilson and Lissaman [204] and Strickland [181] divides the rotor in streamtubes of equal width. It discretizes the crosswind direction of the rotor into multiple contiguous streamtubes. Lissaman [107] assumes an independence between these streamtubes and considers a single induction factor per streamtube. This single value is used for both the upstream and downstream actuator-discs. This model gives very approximate results and fits mostly small load rotors. The prediction of the azimuthal variations of the loads is also inaccurate to a certain extent. The limitations of the multiple streamtube model stem in part from the use of the same induction factor for the upstream and downstream parts of the rotor. This poses a problem because the downstream half is immersed in the wake of the upstream half of the rotor. This is remedied in the double multiple streamtube where each streamtube is divided in upstream and downstream halves – each of them having its own induction factor. A great deal of works [20, 21, 31, 35, 74, 147, 175, and 179] have been conducted using this approach following the pioneering contributions from Paraschivoiu [133-138]. Paraschivoiu later modified the model to incorporate the streamtube expansion effects [140] and was followed by Soraghan

et al [179]. Simao-Ferreira et al. [176] gave a comparative analysis of these actuator-disc based models along with other numerical codes.

The free-wake vortex models developed by Holme [73], Fanucci and Walters [54], and Strickland et al. [182] also demonstrate a semi-analytical approach. This approach assumes an infinite number of blades. Unlike classical actuator-disc models which do not include much information about the blades, this approach allows for the specification of rotor solidity (ratio of blade total chord to rotor circumference). There is an azimuthally varying bound circulation associated with the blade sections. This circulation is calculated from the local effective angle of attack as in classical fixed wing and rotor theories. The change in circulation along the span generates vortex sheets that are convected downstream by the wind. The vortex sheet is approximated by trailing vortices of equal strength. The lift and drag forces on a blade section are calculated using the Kutta-Joukowski principle. The resulting torque is integrated over the blade sections for all the blades in order to obtain the rotor performance. We note that since the lift and circulation are changing along the span and with the azimuth, vortices are continuously shed from each blade to account for the spanwise and azimuthal variations of the bound circulation. In this way, the total circulation (bound + shed) is conserved. These shed vortices are lumped into discrete vortices and are tracked as they are convected downstream. Strickland et al. [182] implemented a vortex simulations for Darrieus turbines in inviscid flow. The lifting line theory was used with airfoil data sheets to calculate the circulation. Li and Calisal [104] used the discrete vortex method with a free-wake vortex to investigate the aerodynamics, acoustics, and performance of vertical-axis tidal turbines. A two-dimensional discrete vortex method was utilized by Osterberg [128] to compute the aerodynamic loads of a VAWT and analyze the wake structure. Later, Zanon et al. [216] used vortex panels to simulate the wake of a VAWT in dynamic stall conditions, while Goude [64] combined the double multiple streamtube for computing the loads and the vortex method to capture the time variation of the flow characteristics.

The cascade model is borrowed from turbomachinery and was first implemented by Hirsch and Mandal [71]. It consists in equidistantly placing the blades one behind another on a plane, the width of which is the circumference of the rotor. A combination of Bernoulli's equation and empirical expressions is used to calculate the wake velocity then the induced velocity. The aerodynamic characteristics of each blade are calculated independently using the local Reynolds number. The model was later improved by Mandal and Burton [112] to account for the dynamic stall.

A more exhaustive review of the analytical methods can be found in the works by Islam et al. [79], Brahimi et al. [24], and Deglaire [43].

The next approach consists in numerically solving the first principles equations through Computational Fluid Dynamics (CFD). This set of methods includes the Direct Numerical Simulations (DNS), Reynolds averaged Navier-Stokes Simulations (RANS), Large Eddy Simulations (LES), and Detached Eddy Simulations (DES).

The DNS solve the Navier-Stokes equations on a fine enough mesh so as to directly capture the physics of the flow and determine the performance. Although attractive because of the accuracy it provides, this approach is limited by the associated computational cost. For this reason, to the best knowledge of the author, it is never used. URANS (Unsteady RANS), however, have been used to a very large extent. In fact, it is adopted in most of the CFD studies of VAWTs. Examples include the works by McLaren et al. [119-120], Simao-Ferreira et al. [173], [175], and Lain and Osorio [98]. McLaren et al. first studied the dynamic thrust and the radial forces of the vertical-axis wind turbine. They later investigated the blade wake interactions in a high solidity small scale rotor. For this purpose, they utilized three different turbulence models (k-ε, k-ω, and k-ω SST) and confirmed the prevalence of the k-ω SST model. Simao-Ferreira, on his side, focused on the study of the dynamic stall. Therefore, we will elaborate on his contribution in connection with this topic.

The LES approach solves the Navier-Stokes equations on a coarser grid compared to DNS to capture the large eddies, and models empirically the sub-grid scales. However, as with DNS, the computational cost is still a major drawback. The LES contributions include the work by Li et al. [108], who used 2.5D LES to study a 'high angle of attack' VAWT. In the same category, Shamsoddin and Porte-Agel [160] studied the flow in the wake of the turbine.

To the best knowledge of the author, the examples of the use of DES in connection to the VAWTs are very limited. Simao-Ferreira [174, 175] has touched on this subject in CFD comparative studies of dynamic stall.

1.4.2 Experimental Approaches

The investigation methodologies for vertical-axis wind turbines are certainly not only computational. We resort also to wind or water tunnel experimentations and open-field operations. The wind or water tunnel experiments are generally the next step after numerical calculations and before the full scale open-field tests. This limits the cost by using reduced scale models. It also allows a more thorough investigation of the physics of the flow. Brochier et al. [26] used water channel experiments with hydrogen bubble visualization and laser-Doppler velocity measurement to investigate the flow dynamics of a straight-bladed VAWT (SB-VAWT). Shiono et al. [166, 167] conducted a comparative study of straight, curved, and helical blades for tidal current turbines. They also studied the effect of the number of blades per rotor. It was found that helically twisted blades gave better performance and three blade rotors were retained as a compromise between the self-starting capability and the need to limit the vibratory loads during the operation.

Fiedler and Tullis [56] conducted open-air wind tunnel experiments to study the effect of blade offset and pitch angle on a high solidity turbine.

Closed cycle wind tunnels have been used more often. Thus, Mertens et al. [122] and Simao-Ferreira et al. [171, 172] studied the skewed flow in SB-VAWT operating on

rooftops. They concluded that the output of the turbine will be reduced by the skewed flow and that the geometry of the roof will influence the choice of the optimum turbine diameter and height. Li et al. [108] simulated the effects of icing by adding attachments to the blade leading edge. Their wind tunnel test showed a degradation of both the stability and the performance. Howell et al. [76] investigated two- and three-bladed rotors. They analyzed the effects of the solidity and surface roughness. Although the roughness makes the boundary layer turbulent, and thus increases the drag, it also helps delay the separation. This circumvents the laminar separation bubble that is otherwise preponderant in low Reynolds number operations. Other wind tunnel experiments are aimed at fine-tuning the different apparatus [57] or showing how the tunnel itself affects the results [86], [87]. The survey of wind and water tunnel related efforts will be continued in connection with the performance evaluation analyses.

The open-field tests constitute the most reliable option, but they are always reserved as the final step not only because of the cost, but also because the feasibility investigations need to be completed beforehand. Although the Darrieus turbines date back to 1931 [40], there have been few notable open-field tests. The available data include the egg-beater turbine operations conducted by the Sandia National Research Laboratories. Worstell presented in his report the aerodynamics of the Sandia 17-meter diameter rotor in [208]. The results for a 34-meter diameter turbine of the same family is provided by Ashwill [8]. Shires [168] shows the results of the open-field operation of the NOVA-V prototype and compares them with the predictions.

In the sub-category of straight-bladed vertical-axis wind turbines, pioneering works have been conducted by the Vertical-Axis Group in the Angstrom Laboratory of Uppsala University, Sweden. A 12 kW SB-VAWT has been extensively investigated in [42, 93, 94, and 178]. For instance, Solum et al. [178] put an emphasis on the design of the mechanical and electrical component of a permanent magnet synchronous generator. Deglaire et al. [42] recorded the wind conditions of the site, analyzed the generator, and

determined the nominal operating configurations. Kjellin et al. [93] detailed the performance of the turbine in a range of tip speed ratios and analyzed the measurement uncertainty. Kjellin [94] also analyzed the electrical systems and provided the open-field experimental results for three SB-VAWTs: the aforementioned 12 kW and two others with nominal powers of 10 kW and 200 kW, respectively.

Other pioneering efforts in this sub-category have been made under the leadership of Dabiri. His group has investigated the use of counter-rotating SB-VAWTs in order to improve the performance of a vertical-axis wind farm. In this regard, Kinzel et al. [90] studied the energy exchange in an array of counter-rotating VAWTs. They found that the 95% velocity recovery distance is about 4 rotor diameters for a single turbine. This distance becomes six diameters for a pair of turbines, which is much less than the 14 diameters for horizontal-axis turbines. These researchers also champion the use of Biomimetics. Thus, Whittlesey et al. [202] used fish schooling to model the turbine/wake interaction in a vertical-axis wind farm.

1.4.3 Performance Studies

Alongside the methodology, the performance related features constitute another major component of the investigation of vertical-axis wind turbines. We will distinguish two main categories. Thus, we will analyze the design and geometrical parameters on the one hand and the flow dynamics and its features on the other hand.

The first group includes the blade profile - camber and thickness, the number of blades, and the solidity of the rotor as well as the blade pitch. For the second group, we will limit ourselves to the Reynolds number, the dynamic stall, and its alleviation techniques.

a. Geometrical Design

The performance studies, in connection with the geometry, have occupied number of researchers. Healy studied the effect of the blade camber [68] and the blade thickness [69] on the power output of vertical-axis turbines. He concluded for his rotor design that a very large camber is detrimental overall to the power output, while thicker airfoils give better results. The camber contributes to improving the self-starting capability, as found by Beri and Yao [22]. The self-starting capability is also investigated in connection with the blade curvature by Li et al. [105]. Qu et al. [144] tried to optimize the location of the airfoil maximum thickness in order to minimize the laminar bubble separation that occurs at low Reynolds numbers. They concluded that the position of the maximum thickness depends on the Reynolds number itself.

The number of blades and the solidity of the rotor also play an important role in the performance and dynamics of VAWTs. A higher solidity was found by Li and Li [106] to give better starting characteristics for a four-blade-rotor at the detriment of the maximum power. It also gives a flatter operating range as concluded previously by Healy [69], and more recently by Sabaeifard et al. [153]. A flatter output variation is also obtained by using a curved or helically twisted blade as in [166, 167] and [156]. The twisting of the blade contributes not only to the self-starting capability, but also alleviates the dynamic stall. For instance, twisted blades [166] have been used so that, at every time, at least part of the blade operates under attached flow conditions and produces power. This approach also flattens the torque production over a cycle reducing the frequency of the torque and blade loads. Thus, it limits the vibratory loads and minimizes the damage to the machinery.

Active control approaches and variable pitch utilizing sensors have also been investigated (e.g., [17], [56], [59], [71], [130], [179], and [180]), but these approaches violate the simplicity of the VAWT configuration and compromise rugged reliable operation and low cost of ownership. For instance, there will be a need to incorporate wind direction sensors to achieve the desired performance. Like in the case of horizontal-axis turbines, these

sensors are not adapted for rapidly and/or frequently changing wind directions, whereas these phenomena and gusts of wind are expected in normal atmospheric operations. We can work around this issue by designing a passive variable pitch. This is done by the use of a dual-arm strut with an offset center of rotation. The locations of the arm attachments to the blades and the distance between the attachments will determine the amplitude and frequency of the variations of the pitch angle. This method was investigated by Kiwata et al. [92] and Erickson et al. [52]. Paraschivoiu et al. [140] analyzed a sinusoidal variation of the pitch and an optimization thereof. They predicted a 30% gain of power as a result of the "optimized" pitch. Rathi [147] studied the variable pitch blade in order to improve the self-starting characteristics and minimize the "dead" zone – region where power is consumed to drag the blade in the medium. This work proposed an azimuthally varying blade pitch so that the blade always operates below its static stall angle of attack. This can be implemented using the offset center of rotation that was discussed earlier. The fixed pitch blade is a rudimentary option and the optimal value will depend on the overall design of the rotor. Islam et al. [81] and Chen and Kuo [34] have investigated this alternative. The rotor in the case of Chen and Kuo [34] has better starting characteristics with a negative pitch angle while a near-zero pitch angle is preferred when the blade reaches its steady rotation phase.

These geometrical parameters have been combined for the design of small scale turbines (e.g. [83, 84], [35], [47], and [153]). Wahl [197] worked on the design of an H-rotor for operation on a South Pole research station. Kumar et al. [95] studied the design of a small turbine for Mars. The analysis of the atmospheric conditions on Mars shows a wind energy potential 5 to 7 times greater than on Earth. They conducted an optimization for the aspect ratio and solidity and analyzed the rotor aerodynamics and performance.

For further power extraction, vanes have been used by Takao et al. [183], while Geurts et al. [60] opted for the use of a diffuser. In the first case, the number of vanes, their

size and the distance between them were investigated. The results showed that the power output depended little with the number of vanes. However, there was some dependence with respect to the distance between them. In the second case, an augmentation of the blade characteristics (angle of attack, normal, and tangential forces) was noticed as well as the shedding of vortices.

b. Flow Dynamics

It has already been stated that small and medium capacity vertical-axis turbines operate at relatively low Reynolds numbers. Under these conditions, complex flow phenomena occur. The occurrence of laminar separation bubbles and laminar-to-turbulent transitions are among the most noticeable. There is also a strong sensitivity to the changes in oncoming stream as well as the flow perturbations generated by the turbine operation itself. In addition to this, large angles of attack may be reached during a cycle. This leads at times to post-stall operation for the blades. This phenomenon combines with the dynamic stall that is even more exacerbated in low tip speed ratios.

There may be limited studies proper to the dynamic stall of vertical-axis turbines. However, because of the periodic variations of the blade angle of attack, we can first look at the dynamic stall of the oscillating single airfoils. Experimental (e.g., [6], [117], [131], [148], and [162]) and numerical (e.g., [3], [196], [199], and [124]) studies are available. These studies help us to understand the dynamics of the flow and constitute a basis for developing dynamic stall models. Other researchers have investigated the combination of pitching and plunging motions (e.g., [192], [194]) and the combination of pitching and translation ([55]). The proper adjustment of the amplitudes and frequencies of the pitching and plunging motions can somewhat approach the type of motion encountered by a blade during VAWT operating cycles.

Despite the valuable information gathered from the single airfoil pitching and/or plunging dynamics, this still may not suffice to analyze the dynamics of a VAWT. For instance,

most of these studies, with very few exceptions, are limited to thin airfoils in relatively small oscillation amplitudes and reduced frequencies. VAWTs, on the other hand, deal with thicker airfoils, much larger amplitudes, and often larger reduced frequencies. Rueger and Greporek [151] studied the aerodynamic characteristics of a NACA0021 airfoil undergoing large oscillations. A comparative analysis of dynamic stall models is provided by Holierhoek et al [72] and showed that the Leishman-Beddoes model approaches relatively well the experimental results of an oscillating airfoil. Dyachuk et al. [45] adapted the Sheng et al. [164, 165] modification of the Leishman-Beddoes dynamic stall formulation to the conditions of this airfoil. Even now the conditions of VAWT operation are still not met. In fact, there is still a need to account for the change in effective velocity during a cycle as well as the blade wake interactions and the associated gusts of wind, among other constraints.

The study of the dynamic stall in the context of the VAWT itself is of utmost importance. Klimas [89] described the interferences (blade/blade wake, etc.), dynamic stall, apparent mass (unsteadiness induced by the inertia of the fluid), and circulatory effects (virtual camber induced by the flow rotation). Oler et al. [126] tried a regulation on the Sandia Darrieus rotors. His two-dimensional unsteady calculations used double panel method with an integral scheme for the attached boundary layer and discrete vortices for the detached boundary layer. Empirical dynamic stall models were later incorporated to the analytical calculations such as the double multiple streamtube models. These empirical models were initially designed for helicopter aerodynamics and later adapted to horizontal-axis turbines. Their parameters were tuned to fit some designs of VAWTs. Thus, reformulated versions of the Gormont, Berg, and Boieng-Vertol models were used by Paraschivoiu [135, 137], Paraschivoiu and Delclaux [136], Masson et al. [115], Brahimi et al. [24], and Shires [168] among other scholars.

The study of the VAWT dynamic stall phenomenon itself was conducted by few scholars. Among them, Brochier et al. [26] conducted water tunnel experiments using laser-Doppler

velocity measurement and hydrogen bubble visualization. They visualized the dynamics of the counter-rotating leading and trailing edge vortices, the blade/wake interaction, and the heavily perturbed flow inside the rotor. The blade-vortex interaction was explored by Amet et al. [7] in 2D simulations using TURBFLOW. A comparison of low (2) and high (7) tip speed ratios underlined the deep stall and the preponderance of vortex shedding at low tip speed ratios. Simao-Ferreira et al. [174, 175] conducted Particle Image Velocimetry (PIV) experimentation as well as CFD of a heavily stalled single-blade rotor. Their CFD work included URANS with the Spalart-Allmaras turbulence model, LES, and DES. Here the DES (Detached Eddy Simulation) is a combination of URANS in the boundary layer and LES in the outer regions.

1.4.4 VAWT Study: a Sustained Effort

The more studies of VAWTs are conducted, the more their potential is highlighted. The renewed interest feeds into the development of the products as well as the continuation of the research for the betterment of the devices. Small VAWTs, in particular, have gathered a great deal of attention because of their practicality among other considerations. The interest is to the point that some research (e.g., Weekes and Tomlin [201]) is dedicated to predicting the wind energy resources for these devices. Slootweg et al. [177], on another hand, focused on the dynamics of the wind turbine systems as part of the overall power supply. They analyzed the dynamic response of the system to the wind speed variations. Deglaire et al. [41] provided a two-dimensional analytical study of the aerodynamic and aeroelasticity coupling on the turbine while Raciti-Castelli et al. [145] and Zhang et al. [217] limited themselves to the aerodynamic loads and proposed CFD based models.

1.4.5 Multi-Element Airfoil and their Current Applications

Another approach not considered thus far for VAWTs is the use of multi-element airfoils. The technique is already used in the racing car industry to improve the ground

adhesion at very high speeds. It is also used for aircraft applications to achieve a high lift coefficient and increase the stall angle of attack. For example, Cebeci et al. [32] studied the low and moderate Reynolds number characterization of single- and multi-element airfoils for aircraft application. They improved the aerodynamic characteristics by use of flaps and slats in multi-element airfoil configurations.

Helicopter industries have also looked at "slotted" or "slatted" airfoils to alleviate dynamically stalled conditions (e.g., [14], [155, and [193]). Passive leading edge droop has also been explored (Figures 1.2, 1.3). These passive devices do alleviate dynamic stall on the retreating side of the rotor, but they may have undesirable effects (increased drag, poor performance under gusty flow conditions) on the advancing side compared with conventional single-element configurations.

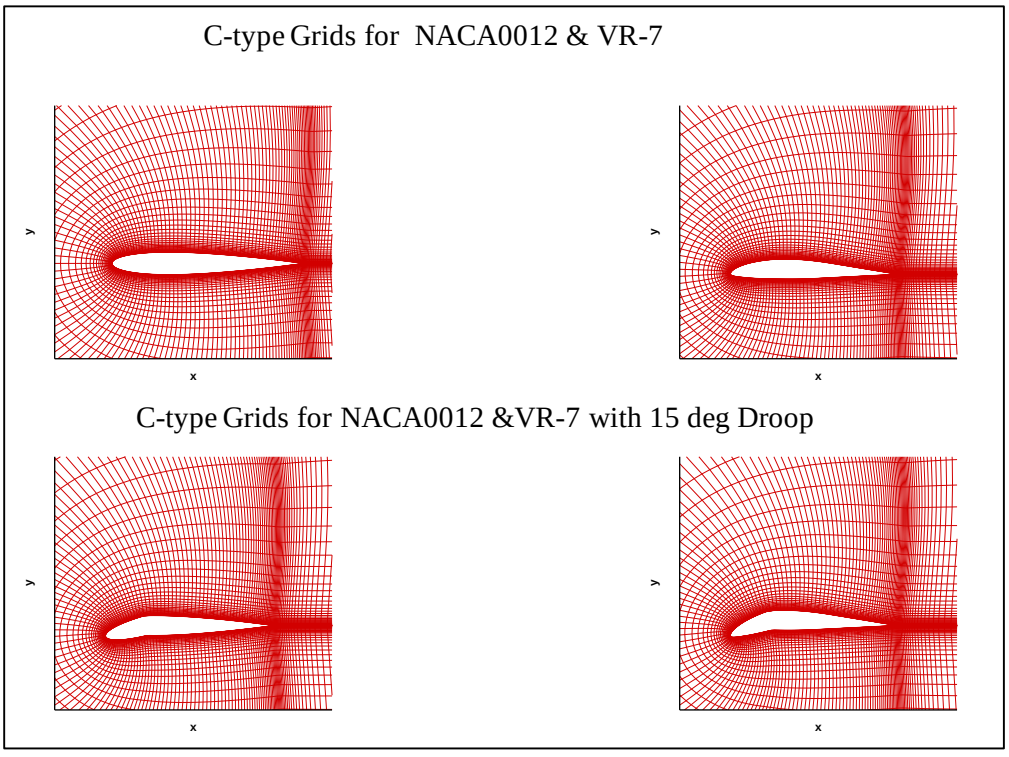

Figure 1. 2: NACA 0012 and VR-7 Airfoils with a Drooped Leading Edge

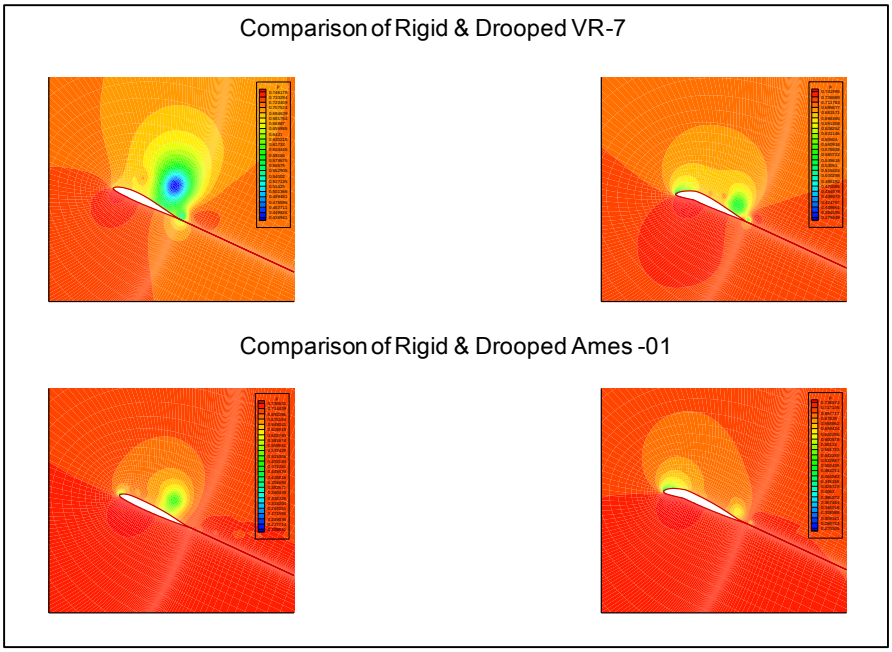

Figure 1. 3: Comparison of Pressure Field over a VR-7 and an Ames-01 Airfoil with and without Droop at 24.7 Degrees during Dynamic Stall

The application of multi-element airfoils extend also to sail wings. Shankaran [161] conducted an analysis and design of such device. Yet another application for these mechanisms is the use of tandem airfoils in axial compressors. In this regard, McGlumphy [116] investigated the subsonic axial flow through tandem airfoils for a core compressor rotor. UAVs (Unmanned Aircraft Vehicles) also utilize this technique. In this context, Ylilamni [212] studied the low Reynolds number flapped airfoils. Shirsath and Mukherjee [169] and Shirsath et al. [170] explored the dynamics of tandem airfoils in pitching motion for micro UAV application. They analyzed the effects of airfoil-wake interactions on the aerodynamic characteristics as well as the effects of the relative motion and phase between the airfoils.

An in-depth wind tunnel investigation of large deflection airfoils at low Reynolds number was conducted by Williamson [203] for optimizing the aerodynamic characteristics. He found that airfoil thickness affects the laminar-to-turbulent transition and the separation, but does not affect so much the lift. The lift depends on the flap-to-chord ratio and the

deflection angle in addition to the Reynolds number. Each airfoil type has its proper optimal deflection and flap-to-chord ratio. He noted a large dependence of the maximum lift-to-drag ratio on the thickness for low deflection angles.

Rival et al. [150] examined the lift augmentation of two pitching and plunging airfoils in tandem formation as a result of the angle of attack, the phase difference and the reduced frequency. They concluded that a proper phasing yields an increase of lift on the front airfoil. In general, there will be a proper combination of parameters that will substantially improve the aerodynamic characteristics.

Fundamental biomimetic studies of tandem airfoils have also being conducted. For instance, Broering et al. [25] mimicked the dragonfly's wings. Their tandem airfoils analysis emphasized the energy extraction and loads as functions of the phase between the airfoils. They compared the results with the single airfoil. They also analyzed the dynamics of the leading and trailing edge vortices.

In the field of wind engineering, the use of multiple-element airfoils remains to be explored. Ragheb and Selig [146] utilized such a technique on removable blade roots for HAWTs. They aimed at reducing the drag generated by the large root sections without compromising the structural integrity. The removable pieces also make it easier to transport the blades.

Passive two-element configurations will be more expensive to manufacture and assemble than single-element VAWTs, but this initial increased cost of acquisition may be offset by increased power production over the life of the device.

1.5 Research Scope and Objectives

The purpose of the present effort enters the broader frame of development of renewable energy solutions as it is becoming clear that fossil fuel sources need to be progressively replaced. The need for replacement arises not only from the progressive depletion of classical fuel sources, but also from the consequences of emissions on health and the environment in general.

The specific aims of the present work are to study the aerodynamics of straight-bladed vertical-axis wind turbines and to contribute to the state-of-the-art of performance improvement techniques. An innovative concept of multi-element blade profile is investigated to achieve the desired performance enhancement. A comparative cost analysis is conducted to see whether the concept is economically viable.

Prior to focusing on the proposed concept, an emphasis is given to the understanding of the dynamics of the classical straight-bladed vertical-axis wind turbines with a single-element blade profile. The flow dynamics is investigated using computational fluid dynamics. A first principles based VAWT dynamic stall model is put forward to meet some of the specific conditions encountered during VAWT operation. The aerodynamic loads are computed by means of CFD and the semi-analytical double multiple streamtube (DMST) model.

In investigating the novel multi-element blade, a parametric study is conducted to identify potential candidates based on aerodynamic criteria. The performance is computed using the DMST model in conjunction with an empirical dynamic stall model. CFD simulations are conducted to analyze the dynamics of the flow.

Following the aerodynamic modeling, an economic analysis of single- and multi-element VAWT configurations is conducted. A representative seasonal wind variation as a Weibull distribution is employed. The total annual energy production is then estimated. The

financial cost of ownership and servicing of the system is also determined. The cost of energy in cents per kilowatt-hour (₵/KWhr) is calculated.

We will thus summarize the objectives as follows:

1. To study the aerodynamics and performance of conventional straight-bladed VAWTs using CFD and DMST:
    a. To compare the interference factors, loads, and performance obtained by the two approaches,
    b. To establish the DMST as a viable substitute for the CFD in the preliminary design phase,
    c. To analyze the dynamics of the flow within the rotor.
2. To use the Leishman-Beddoes first principles approach to adapt the Sheng dynamic stall model to the conditions very specific to the vertical-axis wind turbines.
3. To work on the design of a dual-element blade for dynamic stall alleviation:
    a. To conduct a parametric study to identify a suitable candidate based on the VAWT aerodynamic criteria,
    b. To conduct the performance calculation using the DMST with an empirical dynamic stall model,
    c. To conduct CFD on the dual-element and analyze the flow dynamics
4. To conduct a comparative cost analysis of the single- and dual-element to ensure the economic viability.

1.6 Organization of the Dissertation

The dissertation is organized as follows. A general background on sustainable energies in the context of the overall energy sources has been given here. Following the introduction, this chapter also contains the description of wind energy technologies in general and the physics of vertical-axis wind turbines in particular. A detailed literature survey of prior work in the topics related to the themes of this work has also been given. The second chapter is dedicated to the dynamics of the conventional SB-VAWT. We detail therein the mathematical formulation for the computational fluid dynamics (CFD) and the double multiple streamtube (DMST) model. Chapter 2 also contains the formulation of the Gormont and the customized Sheng dynamic stall models. Validations for the computational tools and introductory elements are provided in chapter 3. Chapter 4 focuses on the aerodynamics and performance of the conventional SB-VAWT. We compare therein the DMST and CFD in order to establish the DMST as a viable approach to screen through numerous case studies. The customized Sheng dynamic stall model is used to approach the conditions encountered during VAWT operations. This model is used along with the empirical Gormont model and the static stall approach. The dual-element investigations are elaborated upon in chapter 5 with details on the parametric studies and the performance evaluation using DMST. In chapter 6, an economic feasibility study is presented. Finally, chapter 7 provides the concluding remarks and the recommendations for future work.

CHAPTER 2

MATHEMATICAL FORMULATION

In this chapter, an overview of the governing equations and numerical formulation used in this dissertation are given. There are two solvers (ANSYS Fluent and the double multiple streamtube – DMST) described in sections 2.1 and 2.2, respectively. The methodology of the computational fluid dynamics (CFD) – that is expounded in [186] – is provided. The equations are simplified and contextualized in light of the problem under investigation. The formulation of the double multiple streamtube (DMST) model is then detailed followed by the description of the Gormont [63] dynamic stall model. The chapter closes with a modified Sheng dynamic stall model, which is customized to vertical-axis wind turbine (VAWT) applications. This model follows the same principles as the Leishman-Beddoes model.

2.1 Mathematical Formulation of the Computational Fluid Dynamics

All the simulations described here were done using the commercial CFD software ANSYS Fluent®. The computational methodology is based on the Reynolds Averaged Navier-Stokes (RANS) equations.

2.1.1 The Navier-Stokes Equations

The problem under investigation assumes an incompressible and isothermal flow. Thus the energy conservation equation doesn't play a role. This leaves us with the mass and momentum conservation equations. The incompressibility is itself synonymous with constant density. With the gravity not taken into consideration and the absence of other body forces and source terms, the mass and momentum equations simplify to:

$$\nabla.\vec{V} = 0 \tag{1}$$

$$\rho\frac{\partial\vec{V}}{\partial t} + \rho\nabla(V^2) = -\nabla P + \nabla(\bar{\bar{\tau}}) \tag{2}$$

In these equations, the viscous stress tensor reads:

$$\bar{\bar{\tau}} = \mu\left[\nabla\vec{V} + \nabla\vec{V}^T\right] \tag{3}$$

These equations are written as follows in the Cartesian coordinate system with the Einstein repeated indices convention:

$$\frac{\partial u_i}{\partial x_i} = 0 \tag{4}$$

$$\rho\frac{\partial u_i}{\partial t} + \rho u_j\frac{\partial u_i}{\partial x_j} = -\frac{\partial P}{\partial x_j}\delta_{ij} + \mu\frac{\partial^2 u_i}{\partial x_j x_j} \tag{5}$$

2.1.2 Moving Mesh Formulation

The problem being solved comprises moving components. This motion is taken into account by making certain part(s) of the computational domain move. For doing so, the conservation equations are adapted to take into account the relative motion between the rotating and stationary parts. Thus for a given scalar Φ, the integral form of the conservation equation on an arbitrary control volume with moving boundary becomes:

$$\frac{d}{dt}\left(\iiint \rho\Phi d\mathcal{V}\right) + \oiint \rho\Phi\left(\vec{V} - \overrightarrow{V_m}\right).d\vec{a} = \oiint \Gamma\nabla\Phi.d\vec{a} \tag{6}$$

V, V_m and Γ denote the velocity of the flow, that of the moving mesh and the diffusion coefficient, respectively. And a second-order backward difference is used to compute the time variation term, which becomes:

$$\frac{d}{dt}\left(\iiint \rho\Phi d\mathcal{V}\right) = \frac{3(\rho\Phi\mathcal{V})^n - 4(\rho\Phi\mathcal{V})^{n-1} + (\rho\Phi\mathcal{V})^{n-2}}{2\Delta t} \tag{7}$$

The superscripts (n), (n-1) and (n-2) denote that the corresponding quantities are taken at successive time levels, with (n) superscript corresponding to the current time level. The $(n)^{th}$ volume is computed as follows:

$$\mathcal{v}^n = \mathcal{v}^{n-1} + \frac{d\mathcal{v}}{dt}\Delta t \tag{8}$$

The time variation of the control volume is computed in a way to satisfy the mesh conservation law.

$$\frac{d\mathcal{v}}{dt} = \oiint \vec{V}_m d\vec{a} = \sum_j^{nf} \vec{V}_{m,j}.\overrightarrow{a_j} \tag{9}$$

The summation in the above equation is done over all the faces of the control volume on the dot product of the mesh velocity and the face area vector. For time levels (n-1) and (n-2), this dot product is expressed as:

$$\left[\vec{V}_{m,j}.\overrightarrow{a_j}\right]^{(n-1)|(n-2)} = \left[\frac{\delta \mathcal{v}_j}{\Delta t}\right]^{(n-1)|(n-2)} \tag{10}$$

$\mathcal{v}_j$ is the volume swept by the control volume face j over the time step Δt.

The (n) time level dot product is expressed using the previous time levels as follows:

$$\left[\vec{V}_{m,j}.\overrightarrow{a_j}\right]^{(n)} = \frac{3}{2}\left[\frac{\delta \mathcal{v}_j}{\Delta t}\right]^{(n-1)} - \frac{1}{2}\left[\frac{\delta \mathcal{v}_j}{\Delta t}\right]^{(n-2)} \tag{11}$$

In the context of sliding mesh, the volume of a cell doesn't change with time, so

$$\mathcal{v}^n = \mathcal{v}^{n-1} = \mathcal{v} \tag{12}$$

And the first term in the conservation equation (6) becomes

$$\frac{d}{dt}\left(\iiint \rho\Phi d\mathcal{v}\right) = \frac{\rho[3(\Phi)^n - 4(\Phi)^{n-1} + (\Phi)^{n-2}]\mathcal{v}}{2\Delta t} \tag{13}$$

And the dot product terms discussed above are nil.

2.1.3 Reynolds Averaged Navier-Stokes

In this formulation the Navier-Stokes equations are averaged using the Reynolds decomposition. This consists in the decomposing of the time varying quantity such as the velocity into a mean time-averaged component and a fluctuating component in the form:

$$u_i(\vec{x},t) = \bar{u}_i(\vec{x}) + u_i'(\vec{x},t) \tag{14}$$

The Reynolds averaged mass and momentum equations become respectively

$$\frac{\partial \bar{u}_i}{\partial x_i} = 0 \tag{15}$$

$$\rho \bar{u}_j \frac{\partial \bar{u}_i}{\partial x_j} = \frac{\partial}{\partial x_j}\left[-\bar{P}\delta_{ij} + \mu\left(\frac{\partial \bar{u}_i}{\partial x_j} + \frac{\partial \bar{u}_j}{\partial x_i}\right) - \rho\overline{u_i' u_j'}\right] \tag{16}$$

There appears in the averaged momentum equation a new term that makes the problem unclosed. This term ($\tau_{ij}' = -\rho\overline{u_i' u_j'}$) is referred to as the Reynolds shear stress tensor and requires modeling in order to close the problem. The Boussinesq approach is retained for the closure model.

$$\tau_{ij}' = -\rho\overline{u_i' u_j'} = \mu_t\left(\frac{\partial \bar{u}_i}{\partial x_j} + \frac{\partial \bar{u}_j}{\partial x_i}\right) - \frac{2}{3}\rho k \delta_{ij} \tag{17}$$

The turbulence viscosity μ_t and the turbulence kinetic energy k are obtained by using a turbulence model.

2.1.4 Turbulence Model

Among all the turbulence models, a two equation formulation is select for the accuracy it offers. In particular the k-ω shear stress transport (k-ω SST) model [120, 121] is chosen because of its ability to represent rotating flows, and flows with high adverse pressure gradients and separation. These phenomena are strongly encountered in the flow through vertical-axis wind turbines that are being investigated.

The transport equations for the k-ω SST model (i.e., turbulence kinetic energy and turbulence dissipation rate) read as follows:

$$\rho \frac{\partial}{\partial t}(k) + \rho \frac{\partial}{\partial x_i}(k u_i) = \frac{\partial}{\partial x_j}\left(\Gamma_k \frac{\partial k}{\partial x_j}\right) + \tilde{G}_k - Y_k \tag{18}$$

$$\rho \frac{\partial}{\partial t}(\omega) + \rho \frac{\partial}{\partial x_i}(\omega u_i) = \frac{\partial}{\partial x_j}\left(\Gamma_\omega \frac{\partial \omega}{\partial x_j}\right) + G_\omega - Y_\omega + D_\omega \tag{19}$$

$\tilde{G}_k$ denotes the turbulence kinetic energy generation due to the mean velocity gradient and G_ω the generation of ω. In these equations, the terms $\Gamma_{k|\omega}$ and $Y_{k|\omega}$ correspond to the effective diffusivities and the dissipations due to turbulence, respectively, and D_ω represents the cross-diffusion. No source terms are considered in this problem formulation. The various terms that appear in these equations are described below.

$$\Gamma_k = \mu + {}^{\mu_t}/_{\sigma_k} \; and \; \Gamma_\omega = \mu + {}^{\mu_t}/_{\sigma_\omega} \tag{20}$$

where the turbulence viscosity (μ_t) and the turbulence Prandtl numbers (σ_k, σ_ω) are respectively defined as:

$$\mu_t = \frac{\rho k}{\omega} \frac{1}{\max\left(\frac{1}{\alpha^*}, \frac{SF_2}{\alpha_1 \omega}\right)} \tag{21}$$

$$\sigma_k = \frac{1}{{}^{F_1}/_{\sigma_{k,1}} + \frac{1-F_1}{\sigma_{k,2}}} \text{ and } \sigma_\omega = \frac{1}{{}^{F_1}/_{\sigma_{\omega,1}} + \frac{1-F_1}{\sigma_{\omega,2}}} \tag{22}$$

Because the vertical-axis wind turbine operates in a relatively low Reynolds number range, corrections are made to some coefficients as shown here.

$$\alpha^* = \alpha^*_\infty \left(\frac{\alpha^*_0 + Re_t/R_k}{1 + Re_t/R_k}\right) \tag{23}$$

where $Re_t = \frac{\rho k}{\mu \omega}$, $\alpha^*_0 = \frac{\beta_i}{3}$, $R_k = 6$, and $\beta_i = 0.072$.

For high Reynolds numbers, the model considers $\alpha^* = \alpha^*_\infty = 1$.

Continuing with the coefficients in the turbulence Prandtl numbers and the turbulence viscosity, we have

$$F_1 = \tanh(\Phi_1^4) \text{ and } F_2 = \tanh(\Phi_2^4) \tag{24}$$

$$\Phi_1 = min\left[max\left(\frac{\sqrt{k}}{0.09\,\omega y}, \frac{500}{\rho\omega y^2}\right), \frac{4\rho k}{\sigma_{\omega,2} D_\omega^+ y^2}\right] \tag{25}$$

$$D_\omega^+ = max\left(\frac{2\rho}{\sigma_{\omega,2}}\frac{1}{\omega}\frac{\partial k}{\partial x_j}\frac{\partial \omega}{\partial x_j}, 10^{-10}\right) \tag{26}$$

$$\Phi_2 = max\left(\frac{2\sqrt{k}}{0.09\,\omega y}, \frac{500\mu}{\rho\omega y^2}\right) \tag{27}$$

In the equations above, y denotes the distance to the nearest wall.

$$\tilde{G}_k = \min(G_k, 10\rho\beta^* k\omega) \text{ and } G_\omega = {}^{\alpha}/_{\upsilon_t}\,\tilde{G}_k \tag{28}$$

The production term G_k is given below in consistence with the Boussinesq formulation.

$$G_k = -\rho\overline{u_i' u_j'}\frac{\partial u_i}{\partial x_j} = \mu S^2 = 2\mu S_{ij} S_{ij} \tag{29}$$

$$\alpha = \frac{\alpha_\infty}{\alpha^*}\left(\frac{\alpha_0 + Re_t/R_\omega}{1 + Re_t/R_\omega}\right) \text{ with } \alpha_\infty = F_1\alpha_{\infty,1} + (1 - F_1)\alpha_{\infty,2} \tag{30}$$

The alpha-coefficients are given by the expressions

$$\alpha_{\infty,1} = \frac{\beta_{i,1}}{\beta_\infty^*} - \frac{\kappa^2}{\sigma_{\omega,1}\sqrt{\beta_\infty^*}},\ \alpha_{\infty,2} = \frac{\beta_{i,2}}{\beta_\infty^*} - \frac{\kappa^2}{\sigma_{\omega,2}\sqrt{\beta_\infty^*}} \text{ and } \kappa = 0.41 \tag{31}$$

The dissipation of turbulence kinetic energy is expressed by

$$Y_k = \rho\beta_i^* k\omega \text{ where } \beta_i^* = \beta_\infty^*\left(\frac{\frac{4}{15} + \left(\frac{Re_t}{R_\beta}\right)^4}{1 + \left(\frac{Re_t}{R_\beta}\right)^4}\right) \tag{32}$$

while that of the dissipation rate reads

$$Y_\omega = \rho\beta_i\omega^2 \text{ where } \beta_i = F_1\beta_{i,1} + (1 - F_2)\beta_{i,2} \tag{33}$$

Finally the cross-dissipation modification, which is a result of the passage from the standard k-ω model to the SST model, is expressed as:

$$D_\omega = 2(1 - F_1)\rho\sigma_{\omega,1}\frac{1}{\omega}\frac{\partial k}{\partial x_j}\frac{\partial \omega}{\partial x_j} \quad (34)$$

The constant parameters that were not already defined in the formulation above are given in Table 1.1.

Table 1. 1: k-ω SST Model Constants

$\sigma_{k,1} = 1.176$	$a_1 = 0.31$	$\alpha_\infty^* = 1$
$\sigma_{k,2} = 1.0$	$\beta_{i,1} = 0.075$	$\alpha_\infty = 0.52$
$\sigma_{\omega,1} = 2.0$	$\beta_{i,2} = 0.0828$	$\alpha_0 = 0.52$
$\sigma_{\omega,2} = 1.168$	$\beta_\infty^* = 0.09$	$\zeta^* = 1.5$
$R_\beta = 8$	$R_k = 6$	$R_\omega = 2.95$

With regard to the wall boundary conditions, the value of ω at the wall is given by:

$$\omega_w = \frac{\rho(u^+)^2\omega^+}{\mu} \quad (35)$$

Analytical solutions can be given for the laminar sub-layer and the logarithmic region respectively in the form:

$$\omega_{lam}^+ = {}^6/_{\beta_i(y^+)^2} \text{ and } \omega_{log}^+ = \frac{1}{\sqrt{\beta_\infty^*}}\frac{du_{turb}^+}{dy^+} \quad (36)$$

The equations and formulae described above correspond to an adapted version of a more general formulation. The formulation was contextualized to the problem under investigation. The corrections were undertaken in order to remain faithful to the context of the problems under investigation. A more general formulation of these equations can be found in [120, 121] and the Fluent® theory guide [186].

2.1.5 Numerical Schemes and Discretization

The numerical formulation uses a pressure based segregated algorithm with a linear pressure-velocity coupling. The velocity coupling is based on the Semi-Implicit Method for Pressure-Linked Equations (SIMPLE) [132]. In this scheme, the velocity and pressure

gradients are computed based on the boundary conditions and initial or current values. Then the discretized momentum equations are solved for the velocity field before computing the mass fluxes at the faces of the cell. Then the equation for the pressure correction is solved in order to determine the pressure correction for a given cell. This new pressure correction term is used to update the pressure field by the mean of the under-relaxation factor, which is set by the user or left at a given default value. The pressure field at the boundaries is then updated with the correction terms before updating the mass fluxes. Finally, the velocity of the cell is updated accordingly. A full description of the SIMPLE scheme with the pressure-velocity coupling can be found in [146].

With regard to the discretization, let us consider the general conservation equation and its discretized form on a given cell as shown in equations (37) and (38), respectively.

$$\frac{d}{dt}\left(\iiint \rho\Phi d\mathcal{V}\right) + \oiint \rho\Phi\left(\vec{V}\right).d\vec{a} = \oiint \Gamma_\Phi \nabla\Phi.d\vec{a} \tag{37}$$

$$\rho\frac{\partial\Phi}{\partial t}\mathcal{V} + \rho\sum_{f}^{Nfaces} \Phi_f \vec{V}_f.\vec{a}_f = \sum_{f}^{Nfaces} \Gamma_\Phi \Phi_f \vec{a}_f \tag{38}$$

The temporal discretization follows a second order implicit formulation and is written as

$$\frac{\partial\Phi}{\partial t} = \frac{3\Phi^{n+1} - 4\Phi^n + \Phi^{n-1}}{2\Delta t} = Func(\Phi^{n+1})$$

where the superscript (n-1), (n) and (n+1) denote the previous, current, and next time levels, respectively. We note that the right hand side scalar function is taken at the next time level, thus the implicit appellation.

For the spatial discretization, the Green-Gauss cell-based method is used for evaluating the gradients. And a second order upwind scheme is utilized. The up-winding indicates that for a given cell, information is carried from an upstream cell and utilized for computing

the present cell. This is expressed in equation (39), where the subscript SOU denotes the second order upwinding.

$$\Phi_{f,SOU} = \Phi_{c0} + \nabla\Phi_{up}.\vec{r} \tag{39}$$

The right hand side terms correspond to the cell center value of the scalar Φ and the dot product of its gradient in the upstream cell with the displacement from the upstream cell center to the center of the face. The gradient at a cell center will be given by equation (40) where the face value is taken as an average of the neighboring cell centers.

$$[\nabla\Phi]_{c0} = \frac{1}{v}\sum_{f}^{Nfaces}\bar{\Phi}_f\vec{a}_f \quad \text{with} \quad \bar{\Phi}_f = \frac{\Phi_{c0}+\Phi_{c1}}{2} \tag{40}$$

The numerical formulation is summarized in the Table 2.1 below.

Table 2. 1: Numerical Formulation

Pressure-Velocity coupling		SIMPLE Scheme
Spatial Discretization	Gradient	Green-Gauss cell based
	Pressure	Standard
	Moment	Second order upwind
	TKE	
	Dissipation	
Time Discretization		Second order implicit
Turbulence model		k-ω SST with low Reynolds number correction

2.2 The Double Multiple Streamtube Model

In the double multiple streamtube (DMST) model, the Darrieus turbine is represented by a series of streamtubes following the direction of the main flowstream. Each streamtube is composed of a pair of actuator-discs in tandem – one in the upstream half of the rotor and the other in the downstream half. Different induced velocities are considered in each half. The streamtubes are assumed to be independent of one another. And the expansion of the streamtubes is neglected because it was found in [140] that it had a

negligible effect on the overall performance prediction. A schematic of the model is presented in Figure 2.1 with only one streamtube being highlighted.

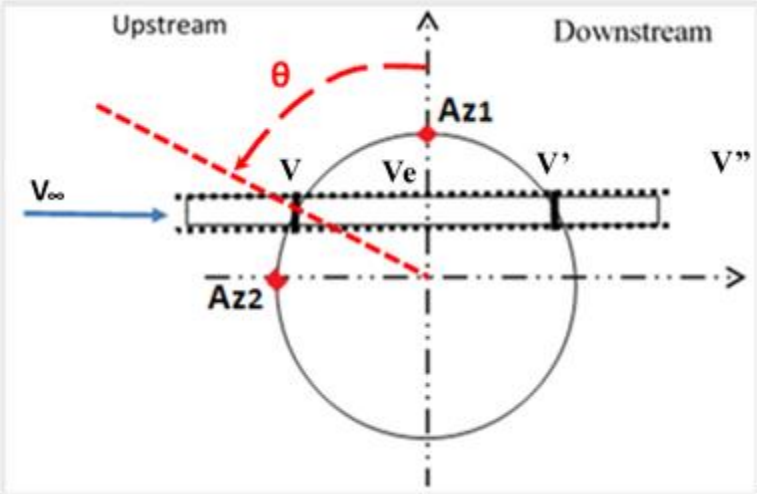

Figure 2. 1: Schematuc of the Double Multiple Streamtube Model

For the purpose of this work, the Earth boundary layer is not considered. Thus, the far-field wind speed is taken constant throughout the height of the turbine. In the streamwise direction, the presence of the turbine progressively slows the wind velocity and this decrease continues through the turbine. This effect is taken into account by introducing interference factors (a, and a'). The velocity relationships through each streamtube are expressed as follows in equations (41) through (44).

$$V = a.V_{\infty} \tag{41}$$

$$V_e = (2a - 1).V_{\infty} \tag{42}$$

$$V' = a'V_e = (2a - 1).a'.V_{\infty} \tag{43}$$

$$V'' = (2a - 1)(2a' - 1).V_{\infty} \tag{44}$$

The direction of rotation and the origin of the azimuth are not standardized in the literature. For instance, Paraschivoiu [137] takes the zero azimuth where the far-field wind velocity

is parallel to the rotor radius and pointing toward the center of rotation. This corresponds to the point '**Az_2**' in Figure 2.1. Other researchers such as Simao-Ferreira [173-175] chose the zero azimuth at the equivalent of point '**Az_1**' in this figure. The latter choice offers the advantage of coinciding the zero azimuth with the zero angle of attack. For this reason the present author preferred this alternative for presenting his work. The equations formulating the model are thus written in a way that reflect this 90 degree offset.

Since the velocity seen by a blade is a result of both the incoming wind and the rotation of the turbine, the effective local upstream speed and geometrical angle of attack are defined as in equations (45) and (46), respectively. $\lambda = \frac{R\Omega}{W}$ denotes the tip speed ratio and Ω the rotation speed of the turbine.

$$W = V.\sqrt{[(\lambda + \cos\theta)^2 + (\sin\theta)^2]} \tag{45}$$

$$\alpha = sin^{-1}\left[\frac{\sin\theta}{\sqrt{[(\lambda + \cos\theta)^2 + (\sin\theta)^2]}}\right] = tan^{-1}\left(\frac{\sin\theta}{\lambda + \cos\theta}\right) \tag{46}$$

Given the angle of attack and the local Reynolds number defined in equation (47), the lift coefficient (C_L), and the drag coefficient (C_D) are determined by interpolating data from look-up tables.

$$Re_b = \frac{W.c}{\upsilon_\infty} \tag{47}$$

The normal and tangential force coefficients are then computed following equations (48) and (49), respectively.

$$C_N = C_L.\cos\alpha + C_D.\sin\alpha \tag{48}$$

$$C_T = C_L.\sin\alpha - C_D.\cos\alpha \tag{49}$$

The calculations for the downstream half follow the same way, where V is replaced with V'. We thus determine the corresponding effective speed (W'), angle of attack (α'), and Reynolds number (Re_b) before calculating the lift and drag coefficients (C'_L and C'_D) with

the data interpolated from look-up tables. The downstream normal force coefficient (C_N') and tangential force coefficient (C_T') are calculated following the same principles shown in equations (48) and (49), respectively. The computation of the interference factors follows an approach close to that of the CARDAAV implementation [137] by introducing the transcendental equation (50). The sign of K_0 is positive for the upstream interference factor and negative for the downstream one.

$$sign(K_0).K.[1-a(\theta)].\cos\theta = a(\theta).f(\theta) \tag{50}$$

Considering the upstream half, a streamtube is centred at an azimuthal location θ and is Δθ wide. The velocity and interference factor are considered constant in this range. This is achieved by considering a sufficient number of streamtubes, so as to narrow the azimuthal width of the streamtube. Thus, solving equation (50) for a(θ), we obtain:

$$a(\theta) = {sign(K_0).K.K_0}\Big/{\left[sign(K_0).K.K_0 + \int_{\theta-\Delta\theta/2}^{\theta+\Delta\theta/2} f(\epsilon)d\epsilon\right]} \tag{51}$$

where $K = 8\pi R/(N_b.c)$, $K_0 = \sin\left(\theta + \frac{\Delta\theta}{2}\right) - \sin(\theta - \frac{\Delta\theta}{2})$ and

$$f(\theta) = \left(\frac{W}{V}\right)^2 [C_N.\sin\theta - C_T.\cos\theta] \tag{52}$$

We determine similarly the interference factor a' (θ) for the downstream half of the rotor.

$$a'(\theta) = {sign(K_0).K.K_0}\Big/{\left[sign(K_0).K.K_0 + \int_{\theta-\Delta\theta/2}^{\theta+\Delta\theta/2} f'(\epsilon)d\epsilon\right]} \tag{53}$$

$$f'(\theta) = \left(\frac{W'}{V'}\right)^2 [C_N'.\sin\theta C_T'.\cos\theta] \tag{54}$$

We note that sign (K_0) is +1 for the upstream half and -1 for the downstream half.

The large number of streamtubes also means that the force coefficients can be assumed to be constant across the width of a streamtube. Thus, the integration of equations (51) and (53) yields the interference factors in equations (55) and (56) where K_0 and J_0 are defined in equations (57) and (58), respectively.

$$a(\theta) = 1 \Big/ 1 + \left(\frac{W}{V}\right)^2 \left[C_N + \frac{J_0}{K_0} C_T\right] \tag{55}$$

$$a'(\theta) = 1 \Big/ 1 - \left(\frac{W'}{V'}\right)^2 \left[C'_N + \frac{J_0}{K_0} C'_T\right] \tag{56}$$

$$K_0 = 2 \sin\theta \,.\, \sin(\frac{\Delta\theta}{2}) \tag{57}$$

$$J_0 = -2 \cos\theta \,.\, \sin(\frac{\Delta\theta}{2}) \tag{58}$$

The average torque coefficients for the two rotor halves are given by equations (59) and (60), respectively.

$$\overline{C_\tau} = \frac{N_b . c . H}{2\pi S} \int_{-\pi/2}^{\pi/2} C_T \left(\frac{W}{V_\infty}\right)^2 d\theta = \frac{N_b . c . H}{2\pi S} \sum_{i=1}^{i=n} C_T(i) \left(\frac{W(i)}{V_\infty}\right)^2 \tag{59}$$

$$\overline{C'_\tau} = \frac{N_b . c . H}{2\pi S} \int_{\pi/2}^{3\pi/2} C'_\tau \left(\frac{W'}{V_\infty}\right)^2 d\theta = \frac{N_b . c . H}{2\pi S} \sum_{i=1}^{i=n} C'_\tau(i) \left(\frac{W'(i)}{V_\infty}\right)^2 \tag{60}$$

The iteration index "i" denotes the i[th] streamtube and "n" the total number of streamtubes. The total power coefficient for the rotor is given in equation (21) where $\lambda_\infty = \frac{R\Omega}{V_\infty}$ is the rotor tip speed ratio based on the far-field wind speed.

$$C_p = (\overline{C_\tau} + \overline{C'_\tau}) . \lambda_\infty \tag{61}$$

The above formulation has been independently coded by the present researcher. Prior to its application to the two-element VAWT rotors, it was validated for a conventional single-element rotor [12].

2.3 Dynamic Stall of Vertical-Axis Wind Turbines

2.3.1 Preamble to the Dynamic Stall

Dynamic stall on an airfoil is the phenomenon by which the airfoil loses lift due to strong perturbations of the flow around it. These perturbations are themselves associated with the aerodynamic separation of the flow. Divers mechanisms may trigger the stall and are associated with large effective angles of attack and/or strongly perturbed incoming flow. In the context of our study, the blade profile of a vertical-axis wind turbine sees a large range of angles of attack in the course of its 360 degree rotation. This phenomenon is even more important when the tip speed ratio (the ratio of the blade tip speed to the incoming flow speed) is small, as demonstrated with the expression of the angle of attack in equation (62) where λ and θ denote the tip speed ratio and the azimuthal location, respectively.

$$\alpha = sin^{-1}\left[\frac{\sin\theta}{\sqrt{[(\lambda+\cos\theta)^2+(\sin\theta)^2]}}\right] = tan^{-1}\left(\frac{\sin\theta}{\lambda+\cos\theta}\right) \qquad (62)$$

Besides the large angles of attack, a strongly perturbed stream will also trigger the dynamic stall. This may occur despite the angle of attack still being within its normal un-stalled range. This phenomenon is commonly encountered by airplane flying through a storm where the turbulence structures no longer allow a streamed flow around the airfoil. This analogy is particularly relevant for vertical-axis wind turbines where in the course of the 360 degree rotation around the rotor axis, a blade may encounter its own wake generated in the previous cycle as well as the wake generated by the other blades of the rotor. The combination of these wakes behaves like wind gusts with large turbulence structures that affect the flow around the blades.

Thus, it is very important to have a careful study of the dynamic stall taking into consideration the very specific conditions of vertical-axis wind turbine. The dynamic stall phenomenon itself has been investigated to a great extent. However, most of these studies

are limited to relatively thin airfoils oscillating in a relatively narrow range of angles of attack (e.g., [23], [49], [101, 102], [117], [131], and [196]). When thick airfoils are investigated, the range of oscillation is limited compared to the range of angle of attack encountered in VAWT operations [23]. The closest attempt for studying the effect of flow perturbations on dynamic stall consists in having an oscillating flow-stream as was done by Alvin-Pierce [5].

The study of a couple of blades in tandem configurations can also help approach to a certain extent the physics of the flow through a VAWT. Numerous studies of oscillating blades in tandem have been conducted (e.g., [25], [169], [170], and [195]). However, even though these segmented investigations may help gain some understanding of different phenomena that are encountered in a VAWT flowfield, it still is primordial to investigate the physics of the flow in its own context. Uncoupling of the components of a physical phenomenon mischaracterizes the solutions because of the very probable non-linear dependencies [96].

There exists a plethora of dynamic stall models or variations thereof ranging from empirical approaches to semi-analytical first principles formulation. Most of these studies were originally applied to helicopter blades (e.g., [63], [101,102], [129], [142], and [190]), and were subsequently adapted to horizontal-axis wind turbines [36], [101]. Efforts to adapt existing dynamic stall models to vertical-axis turbines have also been undertaken (e.g., [114], [115], [133], and [181]). Most of these adaptations are done empirically on a given type of rotor and can be generalized only with great difficulty. Other researchers [61, 62] used reduced aerodynamic modeling in a surrogate based reference framework. Considering for example the lift coefficient, this formulation iterates as follows:

$$C_L^{t+\Delta t} = C_L^t + \vartheta(C_L^{t+\Delta t})$$

The most promising results with regard to vertical-axis wind turbine applications are obtained when starting back from “first principles” models like the Leishman-Beddoes (e.g., Dyachuk et al. [45] and Sheng et al. [165]).

Before we elaborate on this formulation in section 2.3.3, the Gormont empirical model is discussed first in the next section.

2.3.2 The Gormont Empirical Dynamic Stall Model

For the present investigation, the Gormont empirical model was first used because it offers simplicity and a reasonable first order overview of the blade loads and rotor performance. This model works on approaching the hysteresis response by defining a modified angle of attack that is different from the geometric angle of attack defined in equation (62). This Gormont reference angle of attack is given in equation (63). The constant K_1 and variation of angle of attack $\Delta\alpha$ are given in equation (64).

$$\alpha_{Gor} = \alpha - K_1 \Delta\alpha \tag{63}$$

$$K_1 = \begin{cases} 1, & \dot{\alpha} \geq 0 \\ -0.5, & \dot{\alpha} < 0 \end{cases} \text{ and } \Delta\alpha = \begin{cases} \gamma_1 S, & S \leq S_c \\ \gamma_1 S_c + \gamma_2 (S - S_c), & S > S_c \end{cases} \tag{64}$$

$$S = \sqrt{\left|\frac{c\dot{\alpha}}{2W}\right|} \; and \; \gamma_1 = \begin{cases} \gamma_2, [lift\ characteristics] \\ 0, [drag\ characteristics] \end{cases} \tag{65}$$

$$S_1 = 0.06 + 1.5\left(0.06 - \frac{t}{c}\right) \; and \; \gamma_2 = \gamma_m max\left\{0, min\left(1, \frac{M - M_2}{M_1 - M_2}\right)\right\} \tag{66}$$

In the expressions above, c, W, M and $\dot{\alpha}$ denote the blade chord length, effective velocity, Mach number, and time derivative of the angle of attack, respectively. The other parameters are given in Table 2.2 where t/c represents the airfoil relative thickness.

Table 2. 2: Gormont Model: Lift and Drag Parameters

Lift Characteristics	Drag Characteristics
$M_1 = 0.4 + 5\left(0.06 - \frac{t}{c}\right)$	$M_1 = 0.02$
$M_2 = 0.9 + 2.5\left(0.06 - \frac{t}{c}\right)$	$M_2 = 0.7 + 2.5\left(0.06 - \frac{t}{c}\right)$
$\gamma_m = 1.4 - 6\left(0.06 - \frac{t}{c}\right)$	$\gamma_m = 1 - 2.5\left(0.06 - \frac{t}{c}\right)$

The value for the drag coefficient is then taken at the Gormont reference angle of attack instead of the geometric angle of attack.

$$C_D^{dyn} = C_D(\alpha_{Gor}) \tag{67}$$

The lift coefficient, on the other hand, follows a linear interpolation as given by equation (68) where α_0 is the zero-lift or any other convenient angle of attack and m is defined in equation (69). The static stall angle of attack is denoted by α_{ss}.

$$C_L^{dyn} = C_L(\alpha_0) - m(\alpha - \alpha_0) \tag{68}$$

$$m = min\left(\frac{C_L(\alpha_{Gor}) - C_L(\alpha_0)}{\alpha_{Gor} - \alpha_0}, \frac{C_L(\alpha_{ss}) - C_L(\alpha_0)}{\alpha_{ss} - \alpha_0}\right) \tag{69}$$

Strickland et al. [182] proposed a modification to the Gormont for thin symmetric airfoils. They set S_C in equation (64) to zero and only apply the dynamic stall model when the effective angle of attack exceeds the static stall value. Paraschivoiu et al. [137] applied the Strickland corrected model for operations in low turbulence regions taking into account the findings in [26] and [100]. Masse [114] and Berg [20] gave adaptations closer to the "spirit" of the Gormont model by using linear interpolation between the static lift and drag coefficients and those determined using the Gormont model.

The fully empirical dynamic stall model can offer a reasonable first order view of the blade loads and rotor performance. However, these models were designed to fit problems with relatively small variations of the angle of attack and flows of a different complexity. For this reason they present inherent limitations when applied to vertical-axis

wind turbines. Thus, it may be good to go back to the "first principles" models such as the Leishman-Beddoes model or adaptations thereof.

2.3.3 Sheng Dynamic Stall Model customized for Vertical-Axis Wind Turbines

The "first principles" approach consists in examining the flow characteristics and features that trigger and/or contribute to the establishment of the dynamic stall. Thus, we will distinguish the attached flow behavior, the onset of stall, the leading edge separation and vortex shedding, and the trailing edge separation. A similar approach was adopted by Sheng et al. [165] for low Mach number compressible flow and by Dyachuk et al. [45] in investigating oscillating airfoils. The Sheng et al. formulation of the Leishman-Beddoes model followed suit by Dyachuk et al. will serve as a reference for adapting the model for vertical-axis wind turbine operations.

In establishing a dynamic stall model, it is always of primary importance to model the unsteady attached flow behavior. The unsteady attached flow features two essential components generally referred to as circulatory and impulsive responses. The first is a response to the presence of a bound vortex the size of which increases with the angle of attack. It causes a phenomenon referred to as "vortex lift". The impulsive response is directly related to the changing of the angle of attack.

$$C_{N_n}^{Circ} = C_{N_\alpha}\alpha_{E_n} \tag{70}$$

The subscript "n" denotes the current time level and $C_{N\alpha}$ the slope of the normal force coefficient. The equivalent angle of attack is given by:

$$\alpha_{E_n} = \alpha_n - X_n - Y_n - Z_n \tag{71}$$

The expression for X_n, Y_n, and Z_n are given in the set of equations (72):

$$\begin{cases} X_n = X_{n-1}\exp\left(-\dfrac{\beta^2\Delta s}{T_1}\right) + A_1(\alpha_n - \alpha_{n-1})\exp\left(-\dfrac{\beta^2\Delta s}{2T_1}\right) \\ Y_n = Y_{n-1}\exp\left(-\dfrac{\beta^2\Delta s}{T_2}\right) + A_2(\alpha_n - \alpha_{n-1})\exp\left(-\dfrac{\beta^2\Delta s}{2T_2}\right) \\ Z_n = Z_{n-1}\exp\left(-\dfrac{\beta^2\Delta s}{T_3}\right) + A_3(\alpha_n - \alpha_{n-1})\exp\left(-\dfrac{\beta^2\Delta s}{2T_3}\right) \end{cases} \quad (72)$$

The subscript (n-1) denotes the previous time level. The reduced time step and Mach number effect are expressed as $\Delta S = \frac{2W\Delta t}{c}$ and $\beta = \sqrt{1-M^2}$, respectively. The deficiency coefficients $A_{1\text{-}3}$ and $T_{1\text{-}3}$ are given in Table 2.3 below where M is the local Mach number.

Table 2. 3: Sheng Model: Attached Flow Deficiency Coefficients

A_1=0.165	A_2=0.335	A_3=0.5
T_1=20	T_2=4.5	T_3=1.25 M

Besides the circulatory load coefficient given above, the attached flow response comprises also an impulsive part that is expressed in equation (73) where the impulsive time constant is given by $T_{Imp} = \frac{(1+3M)c}{4\sqrt{\gamma RT}}$

$$C_{N_n}^{Imp} = \frac{4}{M}H_n;\ H_n = H_{n-1}\exp\left(-\frac{\Delta t}{T_{Imp}}\right) + \frac{\pi}{4}(\alpha_n - \alpha_{n-1})\exp\left(-\frac{\Delta t}{2T_{Imp}}\right) \quad (73)$$

The total normal force coefficient for the unsteady attached flow thus reads:

$$C_{N_n}^{Att} = C_{N_n}^{Circ} + C_{N_n}^{Imp} \quad (74)$$

The unsteadiness of the flow induces a lag in pressure response for the angle of attack. In a first order approximation, this lag is accounted for by the introduction of a deficiency function as shown in equations (75) and (76).

$$\alpha'_{N_n} = \alpha_n - D_{\alpha_n} \quad (75)$$

$$D_{\alpha_n} = D_{\alpha_{n-1}}\exp\left(-\frac{\Delta S}{T_\alpha}\right) + (\alpha_n - \alpha_{n-1})\exp\left(-\frac{\Delta S}{2T_\alpha}\right) \quad (76)$$

The empirical constants T_α (which is specific to the airfoil profile) and T_P are 6.3 and 1.7, respectively. The value of T_α given here is that of a NACA0021 profile.

It is now essential to formulate the onset of separation. For this purpose, we choose to assimilate the rotation of a blade in a VAWT to a pitching blade around its quarter chord with a flow stream speed equivalent to the effective speed seen by the blade in the VAWT configuration. Thus, the Sheng et al. [165] formulation is adopted and the critical angle of attack is defined by expressions in the equations (77).

$$\alpha_{crit} = \begin{cases} \alpha_{DS0}; & |r_n| \geq r_0 \\ \alpha_{SS} + (\alpha_{DS0} - \alpha_{SS})\dfrac{|r_n|}{r_0}; & |r_n| < r_0 \end{cases} \; and \; r_n = \frac{c\dot{\alpha_n}}{2W} \tag{76}$$

The reduced pitch rate r_0, constant critical stall onset angle α_{DS0}, and static stall onset angle α_{SS} equal 0.01, 17.91, and 14.33, respectively. The last two parameters are airfoil specific and are given here for a NACA0021 profile. The criterion for stall onset is then defined as

$$|\alpha_n'| > \alpha_{crit} \; with \; \alpha_n' = \alpha_{n-1}' \exp\left(-\frac{\Delta S}{T_\alpha}\right) + (\alpha_n - \alpha_{n-1})\exp\left(-\frac{\Delta S}{2T_\alpha}\right) \tag{77}$$

Once the stall onset is established, we need to look at the flow characteristics in the context of separated flow. Under these conditions, the trailing edge separation and leading edge vortex shedding are the two striking and most essential features. Thus, we will write the normal force coefficient under these conditions as:

$$C_{N_n} = C_{N_n}^f + C_{N_n}^v \tag{78}$$

These two contributions are formulated following Leishman-Beddoes [101, 102] and Sheng et al. [164, 165]

$$C_{N_n}^f = C_{N_n}^{Circ}\left(\frac{1+\sqrt{f_n''}}{2}\right)^2 + C_{N_n}^{Imp};\; f_n'' = f_n' - D_{f_n} \tag{79}$$

We note that the circulatory response is corrected with the response of the unsteady boundary layer f_n'', which itself depends on the determination of the unsteady separation point f_n'.

$$f_n' = \begin{cases} 1 - 0.4\exp\left(\frac{|\alpha_n'| - \alpha_1}{S_1}\right); & |\alpha_n'| < \alpha_1 \\ 0.02 + 0.58\exp\left(\frac{\alpha_1 - |\alpha_n'|}{S_2}\right); & |\alpha_n'| \geq \alpha_1 \end{cases} \quad (80)$$

$$D_{f_n} = D_{f_{n-1}}\exp\left(-\frac{\Delta S}{T_f}\right) + (f_n' - f_{n-1}')\exp\left(-\frac{\Delta S}{2T_f}\right)$$

The constants S_1, S_2 and T_f are determined by solving the set of equations (80) under static conditions.

The effect of the leading edge vortex shedding to the normal force coefficient is written in equation (82) where the constant B_1 is 0.5 and the modulation factor V_x appears in (83).

$$C_{N_n}^v = B_1(f_n'' - f_n')V_x \quad (81)$$

$$V_x = \begin{cases} \sin\left(\frac{\pi\tau}{2T_v}\right)^{3/2}; 0 < \tau < T_v \\ \cos\left(\frac{\pi(\tau - T_v)}{T_{vl}}\right)^2; \ \tau > T_v \end{cases} \quad (82)$$

Finally, the normal force coefficient thus obtained is used to calculate the tangential force component following the Kirchhoff formula where the constants η and E are 0.98 and 0.2 respectively.

$$C_{T_n} = \eta C_{N_\alpha}\alpha_E^2(\sqrt{f'} - E) \quad (83)$$

2.3.4 Summary

The double multiple streamtube formulation with and without dynamic stall modeling is summarized by the flowchart in Figure 2.2. In this chart, each iteration of the Sheng model uses information from the previous time level. This is represented here by the function f(n-1) and allows the model to take into account the history of the flow.

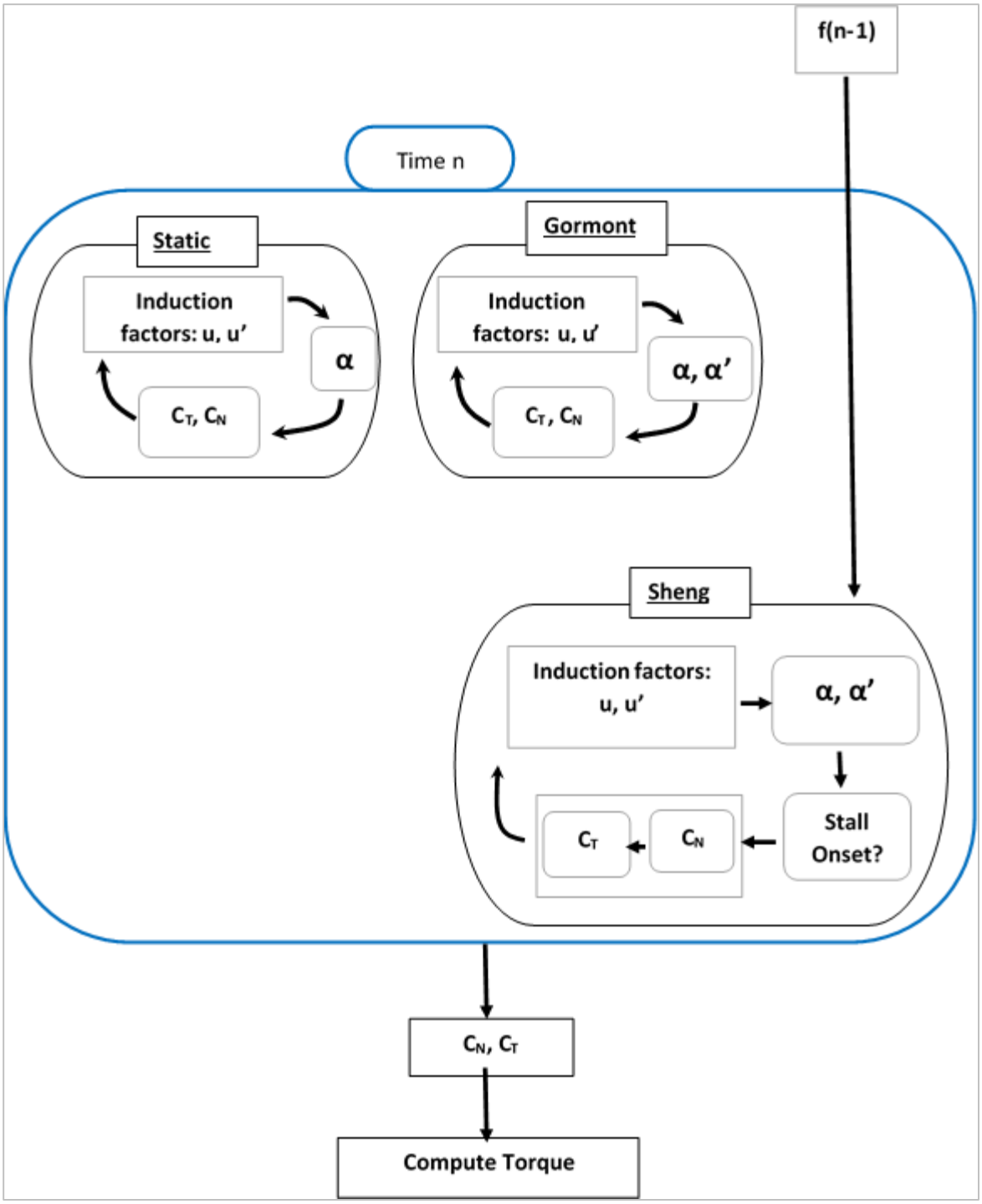

Figure 1.4: DMST Summary Flowchart

CHAPTER 3

PRELIMINARY STUDIES

This chapter is dedicated first to provide a validation of the computational tools before proceeding and then to answer some preliminary questions, and to explain some choices that were made. The chapter opens with the presentation of the open-field reference turbine. Then an empirical study of the effect of the blade pitch angle on the power coefficient is conducted and followed by the preliminary DMST studies. CFD results are then presented as validation of the computational tool followed by a brief comparison between the CFD and DMST. This chapter also includes an introductory analysis of the effect of the number of blades on the performance and dynamics of the rotor. This analysis is conducted at both constant solidity and fixed chord length. We finally analyze the physical pertinence of the use of a single-blade rotor for describing the fully loaded turbine.

3.1 Open-Field Experimental Reference

Open-field experimental data was chosen for reference to our investigations. A model of straight-bladed vertical-axis wind turbine developed by the Vertical-axis group at the Uppsala University (SWE) serves for this purpose. This model, which is rated at 12 kW, has been investigated in open-field settings. Detailed descriptions of the model and related analytical and experimental studies may be found in the works by Solum et al. [178], Deglaire et al. [42], Osterberg [129], Kjellin et al. [93], and Kjellin [94]. Some of the characteristics of the turbine are presented in Table 3.1. It can also be noted from Figure 3.1 that the blades are tapered linearly over the last one meter of their span in both directions. The chord length thus linearly changes from 25 cm to 15 cm. Each of the blades is connected to the central hub by two struts that are attached to the blade near the spanwise

locations where the tapering begins. This turbine is rated to generate 12 kW at 12 m/s wind speed at 127 RPM.

Table 3. 1: SB-VAWT Characteristics

Blade Profile	NACA 0021
Chord	0.25 meters
Blade Length	5 meters
Number of Blades	3
Rotor Radius	3 meters
Hub Height	6 meters

Figure 3. 1: Uppsala 12 kW SB-VAWT [42]

3.2 Effect of the Blade Pitch Angle

The blade pitch angle is sometime used as a means to increase the turbine performance (e.g., [56], [139]). Generally a few degree change in the blade pitch provides substantial improvement. And in some cases a large pitch angle will rather decrease the performance or oblige to change the rotor configuration or size.

For the present analysis an empirical approach is adopted. The methodology used here was originally used for horizontal-axis turbine in Wasynczuk et al. [200] and reproduced in Heier [70]. This formulation was subsequently adapted to vertical-axis turbines by Eid et al. [48] and Omijeh et al. [127]. The power coefficient is expressed as a function of the tip speed ratio and the pitch angle. This expression is given in equation (85).

$$Cp(\lambda,\vartheta) = C_1\left(\frac{C_2}{\lambda_{inv}} - C_3\vartheta - C_4\vartheta^{C_5} - C_6\right)e^{-C_7/\lambda_{inv}} + C_0\lambda_{inv}$$

where (84)

$$\frac{1}{\lambda_{inv}} = \frac{1}{\lambda_\infty + C_8} - \frac{C_9}{1+\vartheta^3}$$

In the above equation $\lambda_\infty = \frac{R\Omega}{V}$ and ϑ denote the tip speed ratio and the blade pitch angle, respectively. The empirical coefficients $C_{k,\,[k=0,\,9]}$ are determined to best match the data from a given turbine model. The data for the reference turbine was obtained from Kjellin et al. [93] and least square curve-fitting was used for computing these correlation coefficients. The results are presented in Figure 3.2 and the corresponding coefficients in Table 3.3.

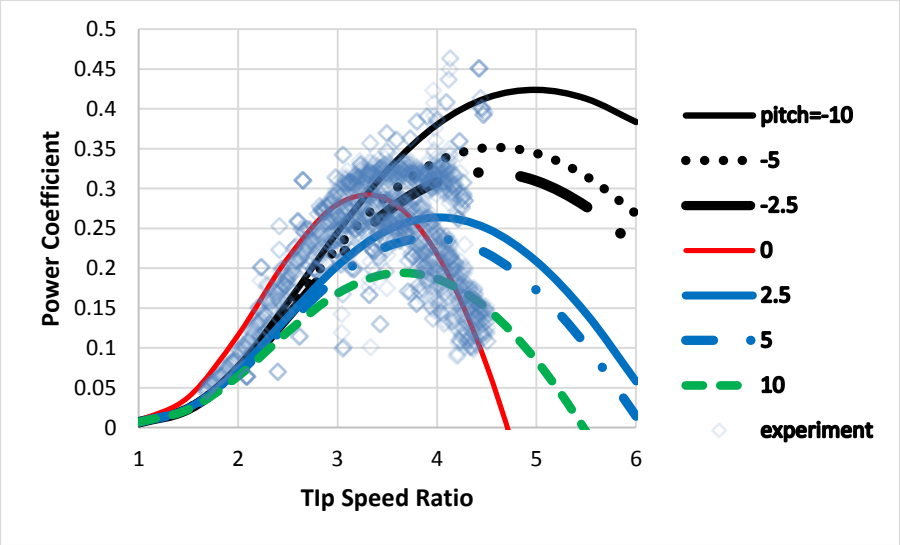

Figure 3. 2: Empirical Variation of the Power Coefficient with the Blade Pitch Angle

Table 3. 2: Empirical Coefficients for the Blade Pitch Dependency

C_0	C_1	C_2	C_3	C_4	C_5	C_6	C_7	C_8	C_9
0.0052	0.408	122.68	0.424	0.0226	1.026	18.025	11.893	0.126	0.064

It is worthwhile to emphasize the dependency of the correlation coefficients with the model of turbine. For each type of turbine, the correlation is to be found by fitting to the available

data. These coefficients cannot be used to extract generalized physical meaning. They are rather specific to a given device.

As mentioned previously, it appears from Figure 3.2 that the power output can be augmented by changing the pitch of the blades. However, this shifts the optimum operating region to higher tip speed ratios. This would be achieved by either making the turbine operate at higher RPMs or increasing the diameter of the rotor. There is not much leeway for considering the first option because the maximum RPM is determined by not only the turbine design (i.e., the size here), but also the wind conditions. On the other hand, the latter option that calls for the increase of the rotor diameter means de facto changing the design. Doing so yields the need for another reference. Therefore, as it appears from the results in Figure 3.2, the zero pitch SB-VAWT will be considered as reference for the rest of the investigations.

3.3 Preliminary Results using the DMST Model

Empirical methods, such as the ones shown above, are limited to a few design parameters (radius and height of the VAWT, tip speed ratio, and blade pitch). These methods are not adequate for the second stage of analysis where the aerodynamic data associated with a family of airfoils must be used to find an optimum single- and multi-element airfoil shapes. The variation of lift and drag coefficients with the angle of attack is also of utmost importance for the current studies. The principles of blade element theory are well suited for this stage of the study, and may be efficiently implemented using Matlab of Fortran scripts, or even on a spreadsheet. The double multiple streamtube model (DMST) was implemented in a Matlab code for the present effort.

In the present work, a number of dynamic stall models have been explored within the context of the DMST model, and the results are shown in Figure 3.3. The models described by Gormont [63] and Berg [20] overpredicted the performance at high tip speed ratios, while Massé [114] under-predicts it. The coefficients in the Gormont model was then tuned

to minimize the over-prediction. For instance, the first implementation of the Gormont model did not contain a dynamic stall correction when the derivative of the angle of attack is negative. This aspect was corrected by utilizing the original formulation of the model in which the dynamic stall was computed under all conditions. Other deviations between the predictions and the test data are attributable to the fact that the turbine has a moderate solidity (0.25) while the DMST generally gives its best results for low to moderate solidity values.

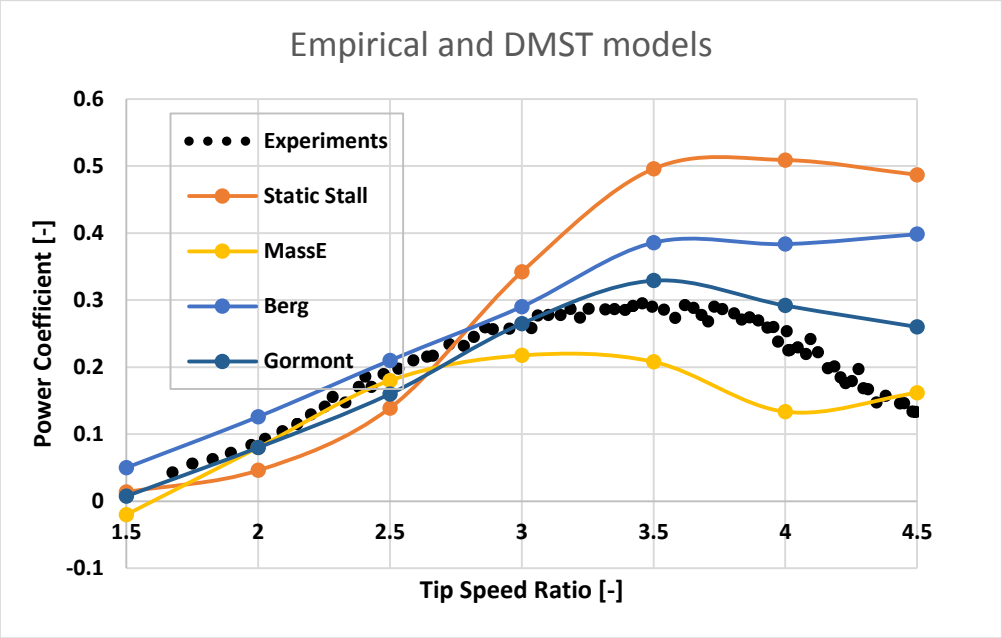

Figure 3. 3: Effects of the Dynamic Stall Models within the DMST Model on the Prediction of Power Coefficient

3.4 Computational Fluid Dynamics Analyses

We finally turn our attention to physics based models that have fewer empirical constants – only those that are needed to model the eddy viscosity. In this study, a two-dimensional CFD study is conducted using the commercial CFD tool Fluent®. The computational domain consists of two main sub-domains – the rotor which is a sliding

mesh and a stationary mesh. The center of rotation is placed at four rotor-diameter lengths downstream of the velocity inlet. The pressure outlet is placed eight diameters downstream of the center of the rotor. The sides are non-slip walls five diameters away on both sides of the center line.

In this section, the variation of the blade torque coefficient as a function of azimuth is examined for a reference blade. The other two blades will have a similar variation, with a phase lag of 120 and 240 degrees, respectively.

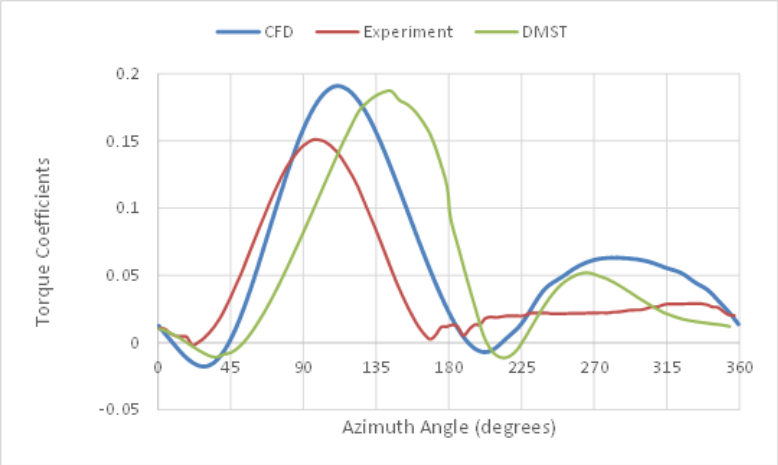

Figure 3. 4: Azimuthal Variation of the Torque Coefficient

The results are presented in Figure 3.4. The CFD simulations predict a higher torque coefficient over much of the azimuth. This deviation may be caused by a number of factors. First of all, this is a 2D simulation that is being compared to a full scale open-field data. In passing, it is worth mentioning that the large blade aspect ratio makes the tip losses negligible. The present 2D model does not take into account the blade taper near the tip. Neither does the simulation include the effect of the struts and the hub. Furthermore, the results in Figure 3.4 were not corrected to account for the blockage.

The DMST model behaves similar to the CFD analysis, but there is a significant phase lag between the test data and the DMST model, possibly indicating that stall is triggered at

higher angles of attack in the empirical model. The post stall behavior is acceptable, given the highly empirical nature of the dynamic stall model.

3.5 CFD Validations

Three sets of CFD simulations were conducted in order to validate the computational tools. The results for Uppsala 12 kW turbine described above are presented first. Thus, Figure 3.5 gives the numerical power coefficient along the curve-fitted experimental data and shows a good agreement over the range of tip speed ratios. This can be explained in two points. First, the height of the rotor is small enough so that the earth boundary effect on the velocity profile can be neglected. Thus, the velocity can be assumed to constant along the span of the rotor. Second, the large blade aspect ratio (20) makes the tip losses marginal as stated before.

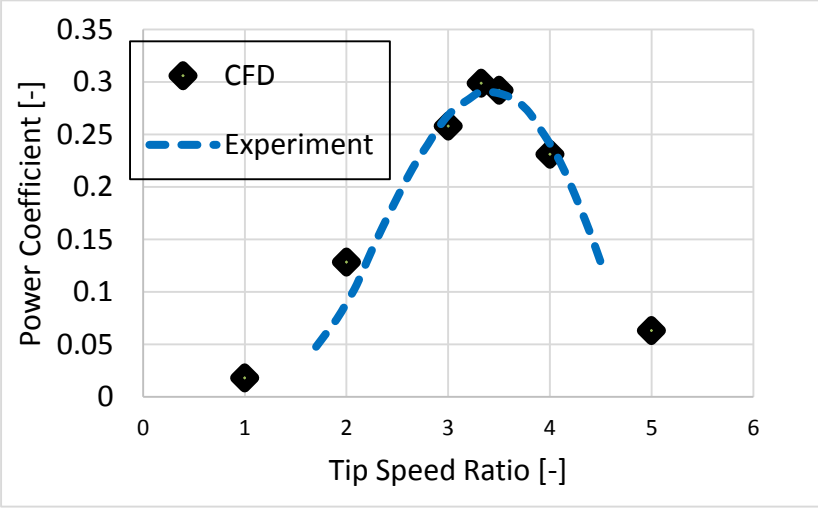

Figure 3. 5: CFD Validation on the Uppsala 12 kW Turbine

The second validation study to be presented refers to the rotor investigated by Li et al. [107] rotor. These authors considered a NACA0018 three-bladed SB-VAWT of chord length 7 cm, height 32.5 cm, and gyration radius 45 cm. The experiment used an open type wind tunnel of outlet section 40 cm x 40 cm. The turbine was placed 50 cm downstream from the wind tunnel outlet. The purpose for this work was to simulate the effect of icing

on the rotor performance by use of a solid attachment at the blade leading edge. The present validation was compared with their experiments without this leading edge device. The results proceed and the power coefficients are presented in Table 3.3 at two tip speed ratios. A reasonable match is observed, in spite of the 2-D strip theory assumption and our ignoring 3-D non-uniformity effects. These results were corrected to account for the blockage. Appendix 1 elaborates on the blockage effect.

Table 3. 3: Comparison of the Present Approach to the Experimental Results by Li et al. [107]

Tip Speed Ratio	1.5	1.8
Cp (Experiment)	0.17	0.03
Cp (CFD)	0.175	0.032

The third validation is based on the experiment by Shiono et al. [166], where a three-bladed turbine of height 30 cm and gyration radius 15 cm is considered. The airfoil is a modified NACA 633-018 profile where the camber line is made to coincide with the gyration path. The subject of the work pertained to turbines with helically twisted blades. We make reference here to their baseline straight-bladed turbine. The average torque reported for this turbine is 1.867 (N.m) per meter of span.

The numerical simulation in 2-D configuration gives an average torque of about 2 (N.m) per meter of span. This corresponds to a difference of about 7% compared to the experiment, primarily because the present simulations do not take into account the tip loss and other three-dimensional effects.

After the validation, some introductory elements are given to lay the groundwork for the main investigations. We begin with the effect of the number of blades at fixed chord length then at fixed solidity.

3.6 Effect of the Number of Blades

3.6.1 Effect of the Number of Blades of Fixed Chord

This section concerns the choice of the rotor configuration with regard to not only its effects on the performance, but also the vibrations it may induce. Castelli et al. [30] studied H-rotors with three, four, and five blades. They kept the same chord length for all three rotors thus did not maintain the solidity constant. The results show that the maximum power output diminishes and that the optimal operating point moves toward lower tip speed ratios as the number of blades increases. This can be explained by a few factors. First, the airflow through the turbine diminishes as the solidity (by extension the number of blades) increases. Additionally, since each blade is generating its own wake, more of the wind kinetic energy is converted into swirling structures instead of being converted to power. This also increases the blade-wake interactions, which are in most cases detrimental to the energy conversion. The increase of the solidity also yields a more curved flow associated with the rotation as will be seen later. As a result of the above factors among others, practical H-rotors generally limit the number of blades from two to four.

Besides impacting the absolute performance, the number of blades will also have effects on both the self-starting capability and the vibrations.

A rotor with three blades has a better self-starting capability compared to the one with two or four blades. It is so because when one blade is facing the wind with a zero angle of attack, the other two blades located at ± 120 degrees have non-zero angles of attack to generate a propulsive lift force. This is not the case for the two- and four-blade rotors that have symmetric configurations.

Furthermore, a symmetric rotor will experience heavy vibrations. This is related to the fact that the radial forces of diametrically opposed blades are in phase when their chords are perpendicular to the freestream as illustrated in Figure 3.6 for a two-blade H-rotor. This phasing occurs twice per cycle for a two-blade rotor and four times in the case of the four-

blade rotor. Since actual turbine rarely utilize more than four blades, we will limit the analysis to this point.

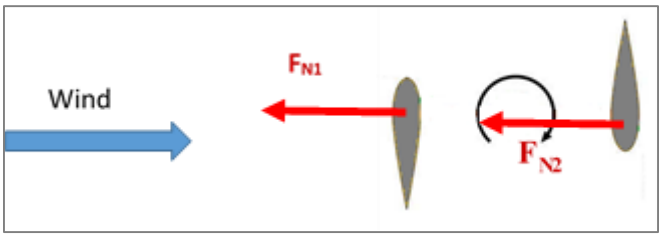

Figure 3. 6: Illustration of Vibration Resonance in Symmetric Rotor

For the reasons provided here, it is deemed that a three blade H-rotor will be the better choice with regard to the self-starting potential, the performance output, and the reduced vibrations.

3.6.2 Effect of the Number of Blades at Constant Solidity

Investigating the effect of the number of blades at a constant solidity comes down to changing the chord length of the blades. It is worthwhile to mention that the size of the rotor (i.e., its diameter) is not changed. The ultimate motivation in this subsection is to pave the way toward the analysis of dual-element blades. The question may arise as to whether a rotor with six small blades could offer the effect sought in a rotor with three dual-element blades. This is partly answered in the previous subsection in the sense that it was then explained that the multiplication of blades increases the loss of energy to the swirling structures. In this subsection, three- and six-blade rotors are being compared. The blade chord length of the former is twice that of the latter to maintain the solidity constant for a given rotor size. Using the double multiple streamtube model without dynamic stall model, Figures 3.7 and 3.8 give the power coefficients delivered by each rotor as function of the

tip speed ratio. Results obtained for both constant RPM and constant wind speed are provided.

The results show that the three-blade configuration is a better choice. The differences that appear in Figures 3.7 and 3.8 are not a result of the wake effect because this is not fully incorporated in the DMST model – the effect of the wake would also have favored the three-blade configuration over the six. Rather these differences are related to the effect of the Reynolds number. To understand this, we first recall that the Reynolds number is defined based on the blade chord length. Thus, at given azimuth locations (and the corresponding blade angles of attack), the Reynolds number changes by a factor two from on configuration to the other.

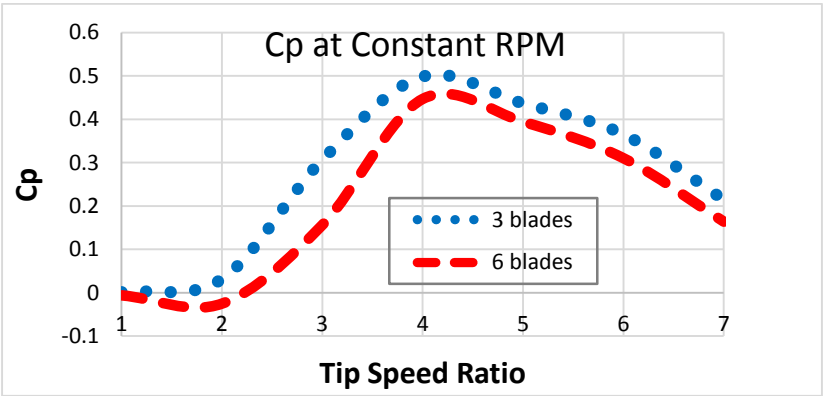

Figure 3. 7: Power Coefficient vs. Tip Speed Ratio at Constant RPM

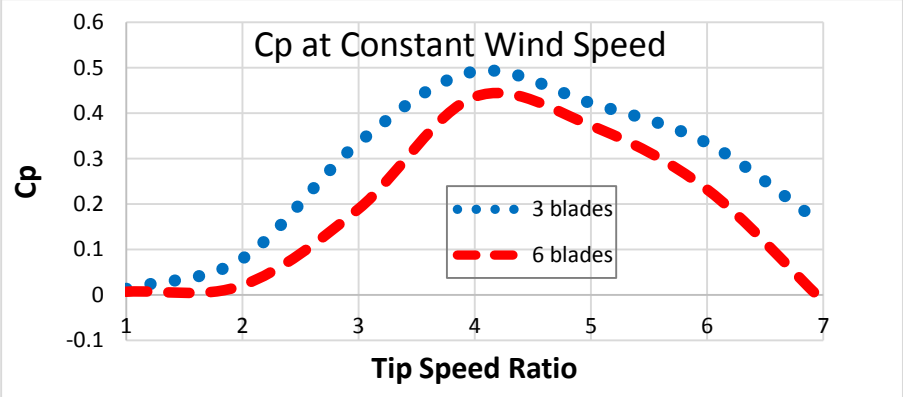

Figure 3. 8: Power Coefficient vs. Tip Speed Ratio at Constant Wind Speed

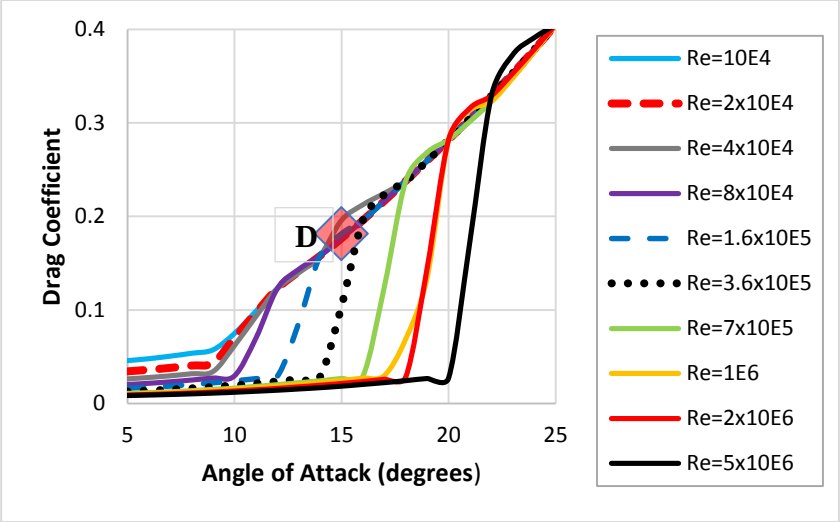

Figure 3. 9: Drag Polar Variations for Given Reynolds Numbers

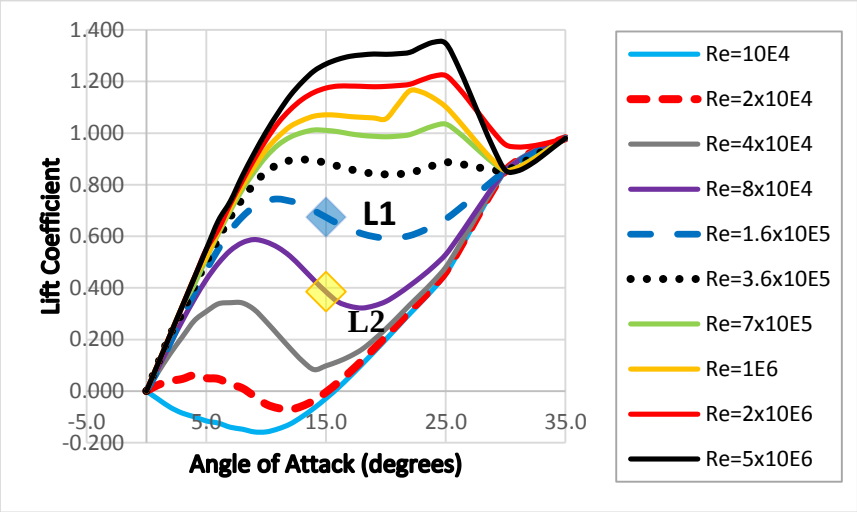

Figure 3. 10: Lift Polar Variation for Given Reynolds Numbers

The illustration of the Drag and Lift polar diagrams in Figures 3.9 and 3.10, respectively, provides a beginning of an explanation for the observed change of performance. For instance, at a certain angle of attack when the Reynolds number changes from $1.6x10^5$ to $8x10^4$, the drag coefficient is almost unchanged as shown by the **D**-mark in Figure 3.9 while the lift coefficient undergoes a more noticeable variation as illustrated by the **L1** and **L2** marks in Figure 3.10. This interpretation fits in the context of low Reynolds number operation of vertical-axis wind turbines and will present limitations when dealing with high Reynolds numbers.

The relation with a dual-element is that a dual-element will be seen as one unit where the Reynolds number is calculated based on the entire chord length. In addition, the overall structure of the wake as generated by a dual-element blade is closer to that generated by a single-element blade of the same size. Therefore it doesn't add significantly into the loss of the oncoming stream energy to the swirling structures. The part that needs investigation is the blade-wake interaction between elements of the same blade.

After analyzing the effects of the number of blades, we now verify whether a single-blade rotor could be utilized to investigate the dynamics and/or performance of a full three-blade rotor as was done in other studies [173-175].

3.7 Physical Pertinence of a One Blade rotor Compared with a Three Blade Rotors

It happens that some researchers utilize a single-blade rotor for investigating concepts and performances of vertical-axis wind turbines. For instance the studies utilizing the actuator disk methodology such as the single streamtube [141], multiple streamtube [125, 181], and double multiple streamtube models [133-140] consider one blade and account for the others by introducing the total number of blades in the calculation of the induced velocities.

On another hand, Simao-Ferreira [175] used a single-blade rotor in his CFD simulations and PIV experimentations of a heavily stalled VAWT. He subsequently provided a full three-blade CFD while investigating the wake generated by the VAWT. CFD simulations with respectively one and three blades were conducted. The torque coefficient of the single-blade rotor is compared with that of a blade in the full rotor configuration during an entire cycle. The results shown in Figure 3.11 indicate that a single-blade approach is not fully representative of the physics of the full turbine as far as the performance is concerned. This

will be further explained in a later chapter dedicated to the flow dynamics of a conventional straight-bladed turbine. The flowfield analysis will be utilized for the interpretations.

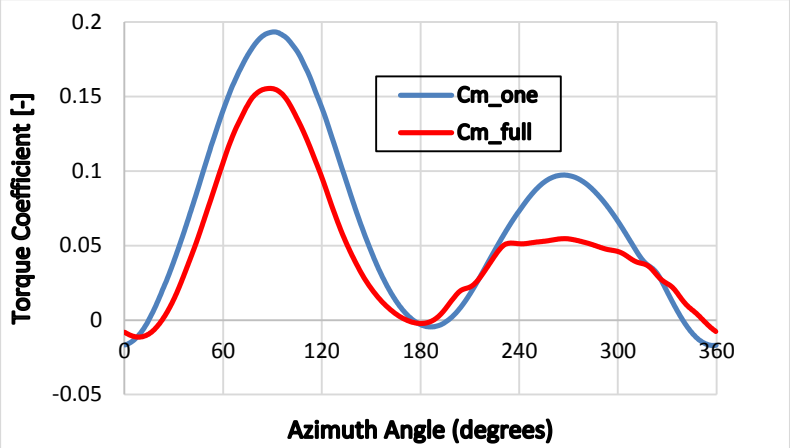

Figure 3.8: Blade Moment Coefficient in Single- and Three-Blade Configurations

3.8 Summary

In this work, a three-pronged approach with increasing complexity and increasing accuracy is used to get an overview of VAWT performance analysis and the associated dynamic stall for a representative system. Empirical curve fits are first used to map the efficiency of the turbine as a function of the tip speed ratio and blade pitch angle. An existing double multiple streamtube methodology (DMST) is next used, with a variety of empirical methods for modeling dynamic stall. Finally, computational fluid dynamics (CFD) results are presented and compared with test data and the DMST approach. This gives the primary elements to conclude that DMST approaches may be considered for screening and designing vertical-axis wind turbine configurations. More refined studies are presented in the later chapters.

Finally, the validation and the introductory elements are discussed in this chapter to lay the groundwork for the study of the straight bladed vertical-axis wind turbine. Thus the investigation of the aerodynamics of a conventional SB-VAWT can be undertaken.

CHAPTER 4

INVESTIGATION OF A SINGLE-ELEMENT BLADE ROTOR USING CFD AND THE DOUBLE MULTIPLE STREAMTUBE MODEL

In this chapter a comparative study is conducted on computational fluid dynamics (CFD) and the double multiple streamtube (DMST) semi-analytical model. The DMST is used with and without dynamic stall models. The empirical Gormont model and a modified Sheng model are utilized to investigate the dynamic stall. The aims after this chapter are to explain the aerodynamics of the VAWT, to provide a dynamic stall model that is more suitable to conditions specific to the VAWTs, and to establish the DMST method as a viable substitute to the CFD to limit the computational cost during preliminary design studies. The spirit of these goals is reflected in the flowchart displayed in Figure 4.1.

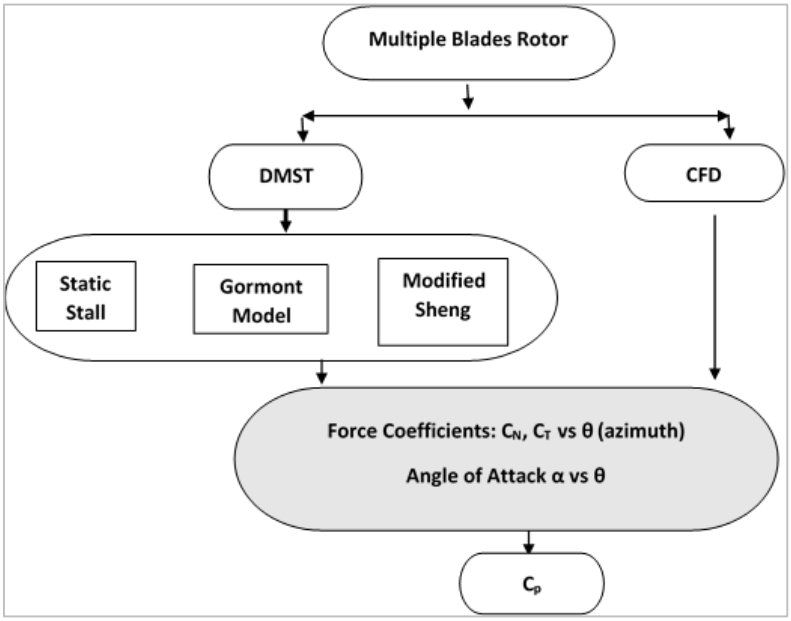

Figure 4. 1: CFD vs. DMST Flowchart

The angle of attack, force coefficients expressed as functions of the azimuth angle on one hand, and the hysteresis loops giving the force coefficients as functions of the angle of attack are deemed representative enough of both the aerodynamics and the performance of the rotor. Thus, the last step that yields the power coefficient will be omitted. In fact, this information is already contained in the tangential (i.e., propulsive) force coefficient (C_T). This choice was motivated by the intent to limit the number of tip speed ratios presented. And since the power coefficient is generally presented as a function of the tip speed ratio, it would then necessitate the examination of a number of cases to have a representative curve.

In the present chapter, first, the dynamic stall is investigated using the characteristic hysteresis loops. A comparative analysis of the force coefficients obtained using CFD and DMST is conducted. The DMST calculations are carried in conjunction with static stall, the Gormont empirical model, and the modified Sheng model.

The aerodynamics and performance of the VAWT are then discussed. This part emphasizes the variations of the angle of attack and the loads as the blade completes its rotation.

Before proceeding with the two main topics, we briefly recall the description of the reference turbine and computational settings. A preamble to the rotor aerodynamics and elementary computational outputs are also given.

4.1 Descriptions

4.1.1. Description and Computational Settings

The straight-bladed rotor was described in Chapter 3. Some of its key features are summarized again in Table 4.1. The SB-VAWT is rated at 12 kW, 12 m/s wind speed, and 127 RPM.

Table 4. 1: SB-VAWT Characteristics

Blade profile	NACA0021
Chord	0.25 m
Rotor Radius	3 m
Number of Blades	3

Two-dimensional CFD simulations are carried out, and the computational domain consists of two main sub-domains: a sliding mesh rotor and a stationary mesh. A sketch of the computational domain is presented in Figure 4.2.

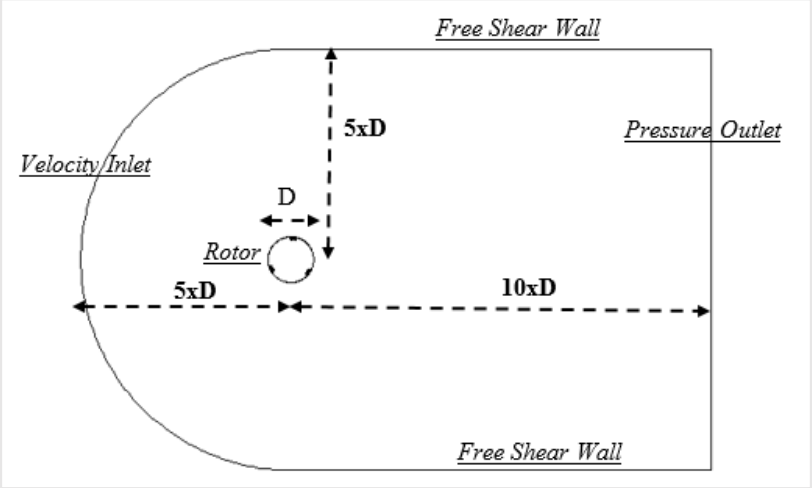

Figure 4. 2: Sketch of the Computational Domain

The center of rotation is placed at five rotor-diameter lengths downstream of the semi-circular velocity inlet. The pressure outlet is placed ten diameters downstream of the center of the rotor. The sides taken to be free-shear walls are five diameters on both sides of the center line. Corrections were made to account for the blockage, which is detailed in Appendix 1.

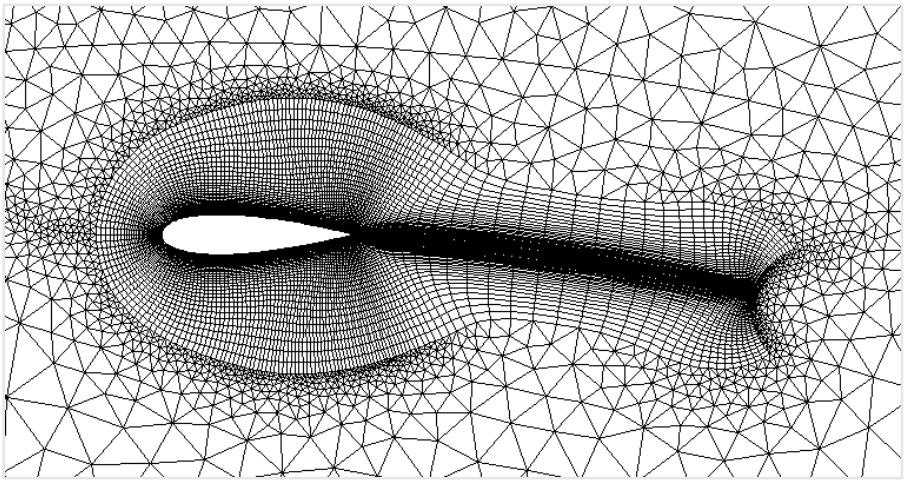

Figure 4. 3: Hybrid Mesh near a Blade

The mesh is fully unstructured in the stationary domain, while the rotor region is hybrid. In fact, a structured mesh is used in the near blade regions to resolve properly the flow in the boundary layer region. The remainder of the rotor region is completed with an unstructured mesh. The two types of mesh structures are connected by non-sliding interfaces, whereas the interface between the rotor and stator is of a sliding type. Pictures of the mesh in the near blade region are provided in Figures 4.3 and 4.4.

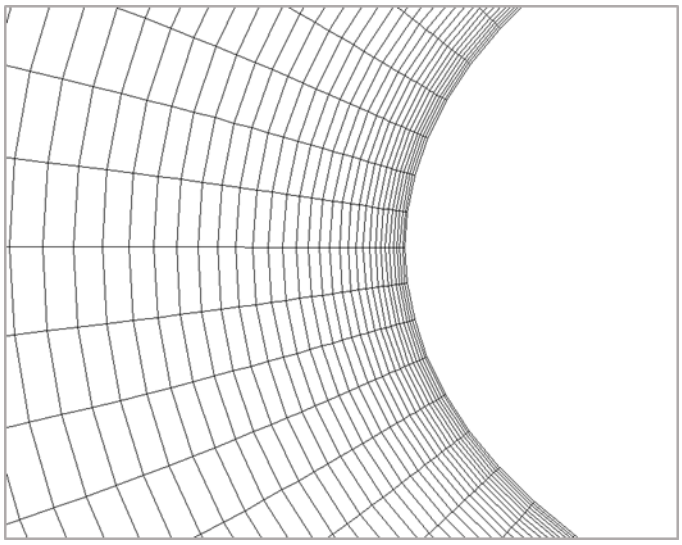

Figure 4. 4: Structured Mesh Refined in the Boundary Layer Region

The numerical setup and boundary conditions were also given in Chapter 2 and are repeated here in Table 4.2 for completeness. A second-order discretization in space and time have been used for better accuracy.

Table 4. 2: Numerical Setup

Pressure-Velocity coupling		SIMPLE Scheme
Spatial Discretization	**Gradient**	Green-Gauss cell based
	Pressure	Standard
	Moment	Second order upwind
	TKE	
	Dissipation	
Time Discretization		Second order implicit
Turbulence model		k-ω SST with low Reynolds number correction

4.1.2. Preamble to the Aerodynamics and Flow Computations

A. Aerodynamics

In the course of a 360-degree rotation around the axis of a turbine, a blade undergoes substantial changes in the angle of attack. The effective flow speed it sees also changes during this course. Consequently, the forces experienced by the blade are also varying. Figure 4.5 depicts these forces at a given position.

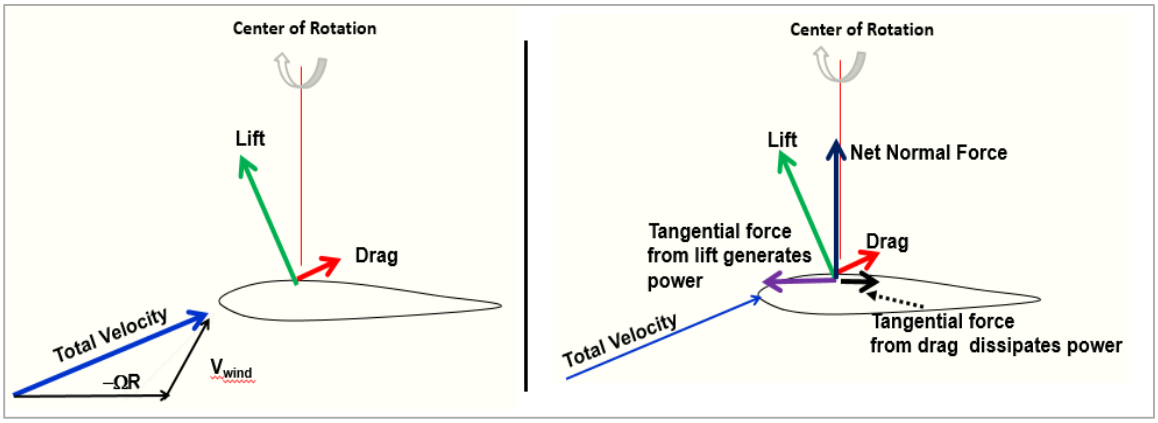

Figure 4. 5: Description of the Forces on a Rotating Blade

We note that at times some of these forces contribute to the propulsive trust, while at other times they act as a hindrance and instead contribute to the drag forces. In Figure 4.5, the angle of attack is the angle between the total velocity vector and the blade chord. This angle of attack may attain large values depending on the tip speed ratio, as shown in Chapter 2 and repeated here for convenience.

$$\alpha = sin^{-1}\left[\frac{\sin\theta}{\sqrt{[(\lambda-\cos\theta)^2+(\sin\theta)^2]}}\right] = tan^{-1}\left(\frac{\sin\theta}{\lambda-\cos\theta}\right) \qquad (85)$$

B. Flow Computations

The CFD simulations are obtained as described above. "Numerical" probes are introduced to compute the velocity near the blade and determine its angle of attack.

Although it was concluded in the preliminary chapter that a single-blade rotor could not fully relay the physics of a blade in a multiple-blade rotor, calculations of such a single-blade rotor were kept for comparison purposes. In such a case, the "numerical" probe was placed at a radius of 3.25 meters in the continuation of the blade chord line. For the three-blade rotor, three probes are used and still placed at a radius of 3.25 meters but at an equal distance from any two blades. The three sets of data are averaged, taking into account the phase lag between them. The choice of the 3.25 meter radius is not exclusive and other carefully selected locations could very well provide the information needed. This location was selected for numerical convenience. For instance, this corresponds to the interface between the rotor and stator domains and there exists a clearly defined connector. This made it numerically easier to place a probing "point."

The three-blade rotor CFD velocities thus obtained are used to compute the interference factors as defined in the DMST formulation and compared with the DMST values. Figure 4.6 shows the comparison for a tip speed ratio of 3. Since this interference factor is at the root of the DMST formulation, the difference that is observed here at a given tip speed ratio will be reflected in the determination of the blades' aerodynamic loads and the rotor

performance. Thus, the differences between the two approaches will be examined in connection with force coefficients in the following sections.

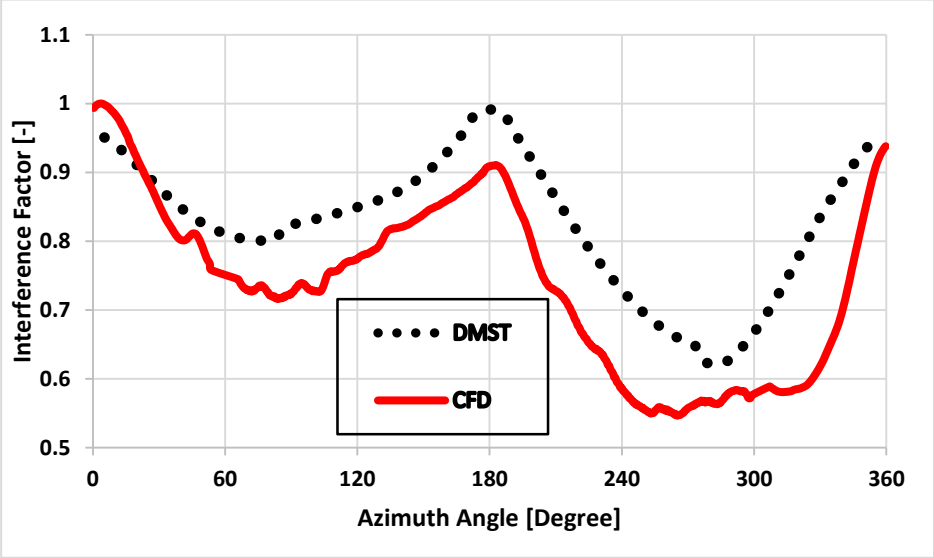

Figure 4. 6: CFD and DMST Interference Factors (TSR = 3)

4.2 Dynamic stall on an SB-VAWT

Efficient and reasonably accurate methods are needed for computing the performance as an important first step toward designing next-generation VAWT systems. The DMST has been used to this effect and has proved to give valuable first-order approximations of the rotor performance. However, it may need improvement for better accuracy. In this section, the focus is on dynamic stall modeling. The conditions and challenges very specific to the VAWTs were described in Chapter 1. And the dynamic stall formulation was detailed in Chapter 2. The comparison between the static stall and dynamic stall DMST and the CFD is presented in this section. For the sake of brevity, the presentation is limited to the hysteresis loops of the normal and tangential force coefficients for a couple of tip speed ratios, namely, 3 and 4. Figures 4.8 and 4.9 corresponding to the TSR 3 give the normal and tangential components, respectively. Figures 4.11 and 4.12 correspondingly relate to TSR 4. These sets of force components are presented along with the azimuthal variations of the angle of attack in Figures 4.7 and 4.10 for TSRs of 3 and 4, respectively.

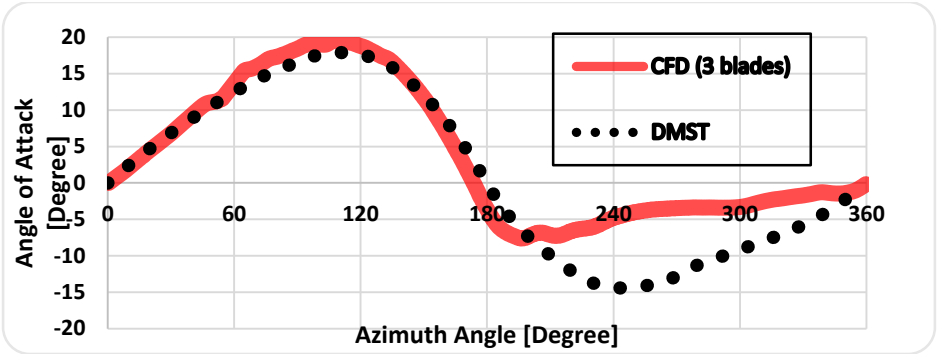

Figure 4. 7: Angle of Attack (TSR = 3)

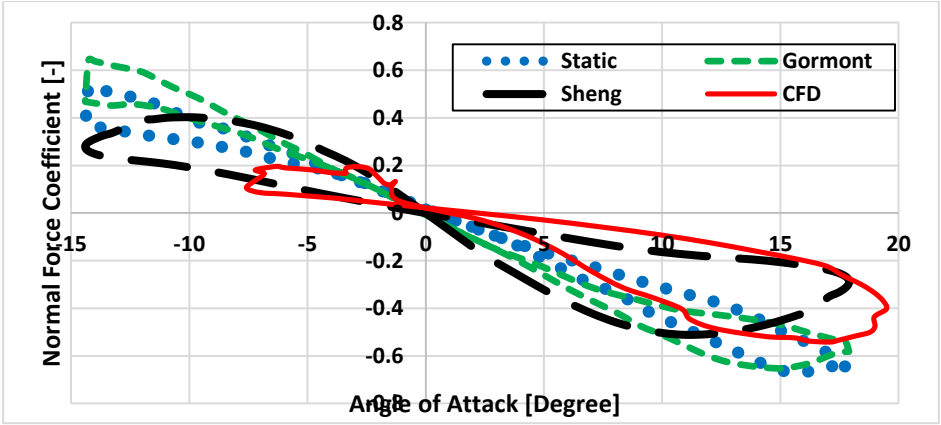

Figure 4. 8: Hysteresis Loop: Normal Force Coefficient (TSR = 3)

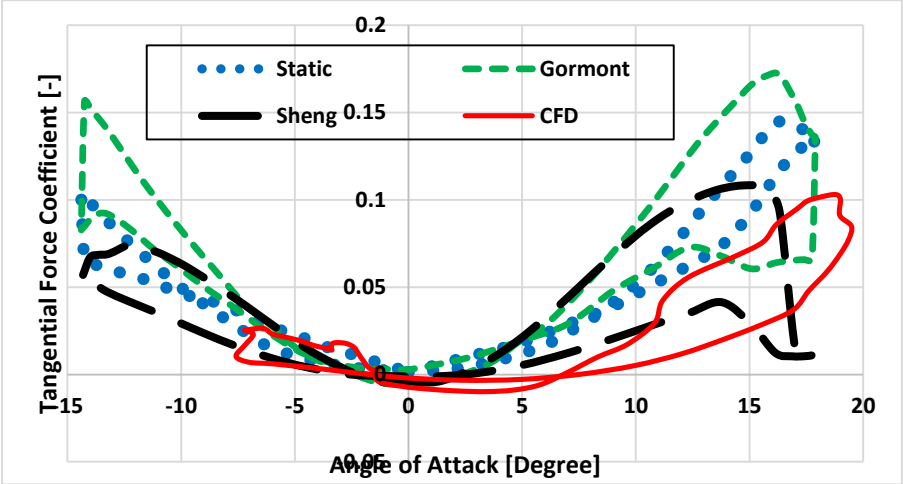

Figure 4. 9: Hysteresis Loop: Tangential Coefficient (TSR = 3)

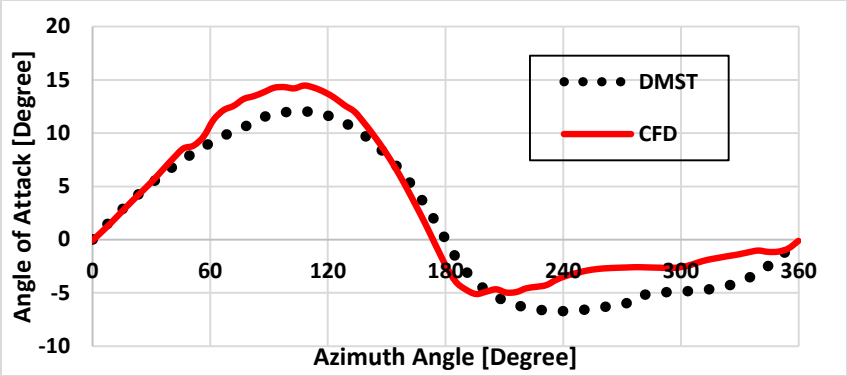

Figure 4. 10: Angle of Attack (TSR = 4)

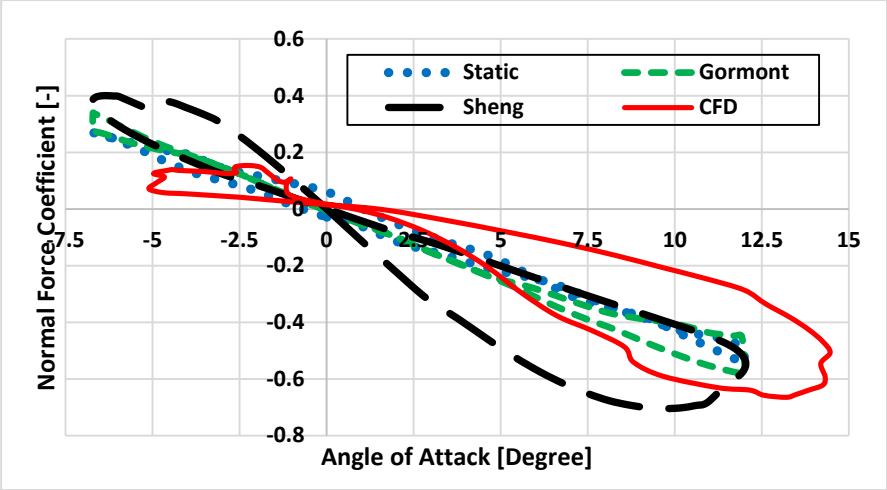

Figure 4. 11: Hysteresis Loop: Normal Force Coefficient (TSR = 4)

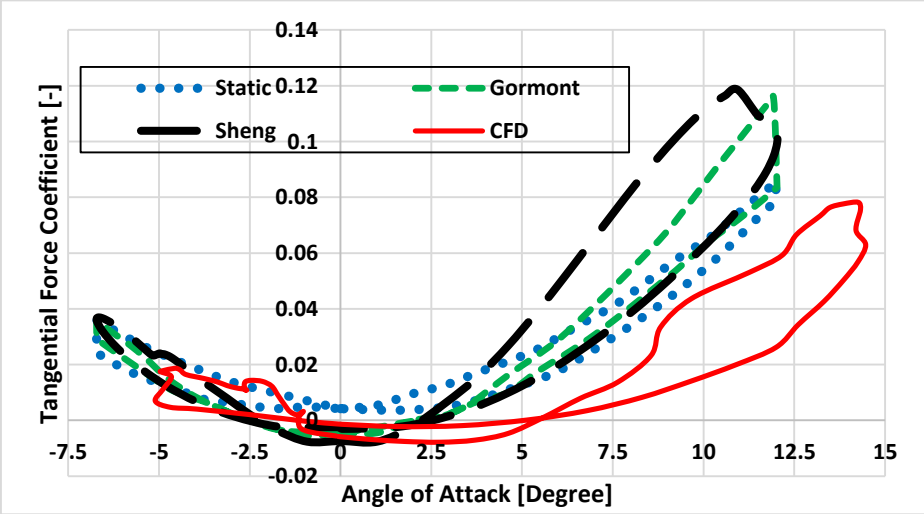

Figure 4. 12: Hysteresis Loop: Tangential Force Coefficient (TSR = 4)

For the purpose of illustration, the same azimuthal variation of the angle of attack is taken to represent the different DMST calculations.

In all cases, it is noted that the static stall fails to predict not only the load values but also the amplitude of the hysteresis cycle. The tangential forces are generally over-predicted by the static stall, while the normal forces are generally under-predicted for positive angles of attack and over-predicted for negative angles of attack. Although the mispredictions constitute an issue in themselves, the profile of the hysteresis cycles is of greater importance. For instance, an offset of the angle of attack from one approach to the other may cause the translation of the pattern. The deviation noted with the static stall may be attributed to the non-incorporation of the dynamic stall. In such an approach, the upstroke-like and downstroke-like motions of the blade resemble one another to a great extent. This results in the narrowing of the body of the hysteresis cycle as observed.

The shape of the loops is improved when we went from the static stall calculations to the Gormont dynamic stall model. This corresponds to a clearer differentiation between the upstroke-like and downstroke-like motions of the blade. This greater recovery is noted for the lower tip speed ratio. This is due to the fact that the dynamic stall is more preponderant under this condition. However, this recovery is still very limited compared to the result obtained using CFD. The small recovery observed can be attributed to the empiricism behind the model. For instance, the model was designed to fit different operating conditions in terms of range of angles of attack and reduced frequencies. The adaptations to the model were also made to fit specific configurations. For example, Strikland et al. [182] decided to drop certain terms when dealing with airfoils of percentage thickness greater than 12%. This was restricted to low turbulence regions by Paraschivoiu et al. [137]. The Berg [20] modification to the Massé [114] formulation, on the other hand, was fitted to the Sandia 17-meter turbine.

For these reasons, it was deemed added-value to look at a first principles based model and to customize it to the conditions of the VAWT operation. The Sheng modified

Leishman-Beddoes model served as a basis for this work. The results are presented in the previous figures along with the aforementioned formulation. These results show a good recovery of the hysteresis loops. The bifurcations observed at high angles of attack correspond to convergence defects.

The mispredictions are also greatly attenuated for the lower tip speed ratio. On the other hand, the higher tip speed ratio only sees such an attenuation for a narrower range of small angles of attack.

To explain this difference, it is worth a reminder that the model was built by considering the key features of attached and separated flow conditions. The preeminence of separated flow and dynamic stall at low tip speed ratio was emphasized. Under these conditions, the model will thus give better accuracy, while it could slightly deviate under different flow conditions.

Overall, it can be seen that the new approach yields a better rendering of the CFD results. A more exhaustive study of the loads is conducted using this model as well as the computational fluid dynamics to investigate the aerodynamics and performance of the rotor.

4.3 Aerodynamics and Performance of the SB-VAWT using CFD and DMST

In this section, the aerodynamic loads and performance are investigated using CFD and DMST. In order to do so, the azimuthal variations of the angle of attack and the normal and tangential force coefficients are considered. As a reminder, details of the CFD formulation and the double multiple streamtube model are available in Chapter 2. The computational settings were elaborated upon in section 4.1 above.

Before proceeding, the reader is reminded with the sign convention adopted for the force coefficients. The tangential component is positive when it is in the direction of the rotation, thus contributing the power production. From this, it take its other appellation,

propulsive force. The normal component is taken positive when it points toward the center of rotation. It contributes mainly to the rotor structural dynamics.

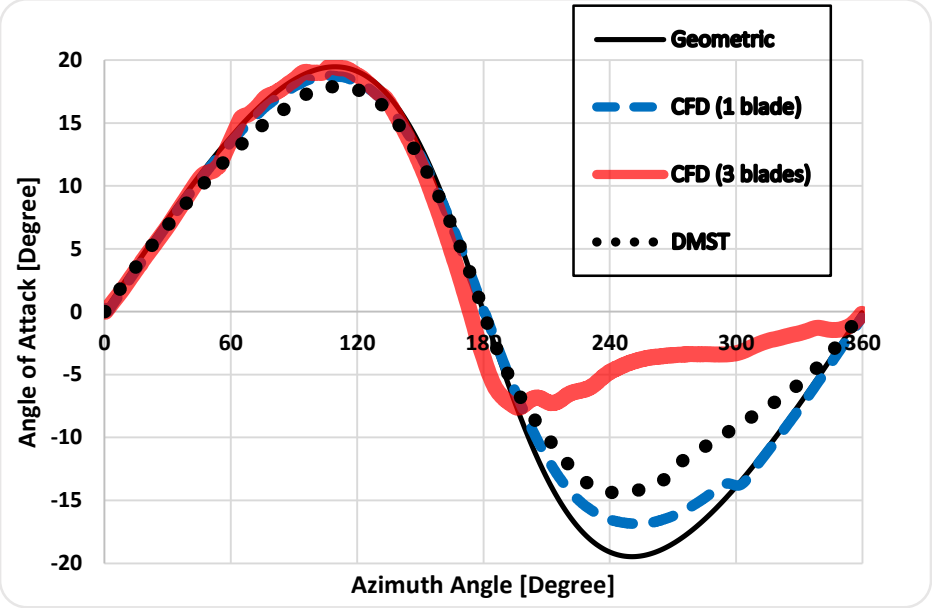

Figure 4. 13: Azimuthal Variation of the Angle of Attack (TSR = 3)

Four configurations corresponding to as many tip speed ratios are presented here. For each case, the angle of attack and the components of the force coefficients are utilized. Specific to the TSR of 3, the CFD of a single-blade rotor is included for comparison purposes. This case is also supported by flow-field images for interpretation.

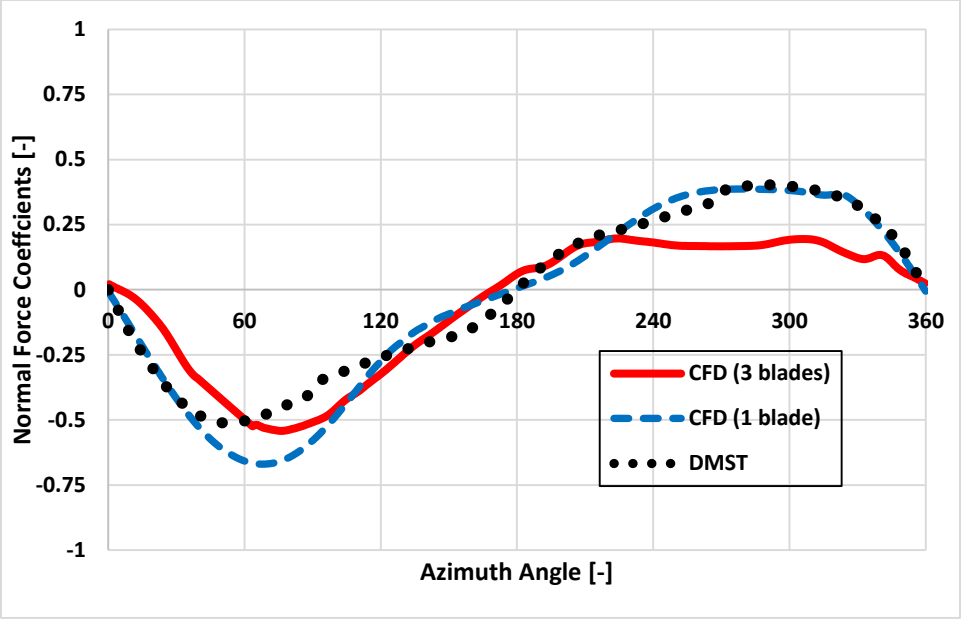

Figure 4. 14: Azimuthal Variation of the Normal Force Coefficient (TSR=3)

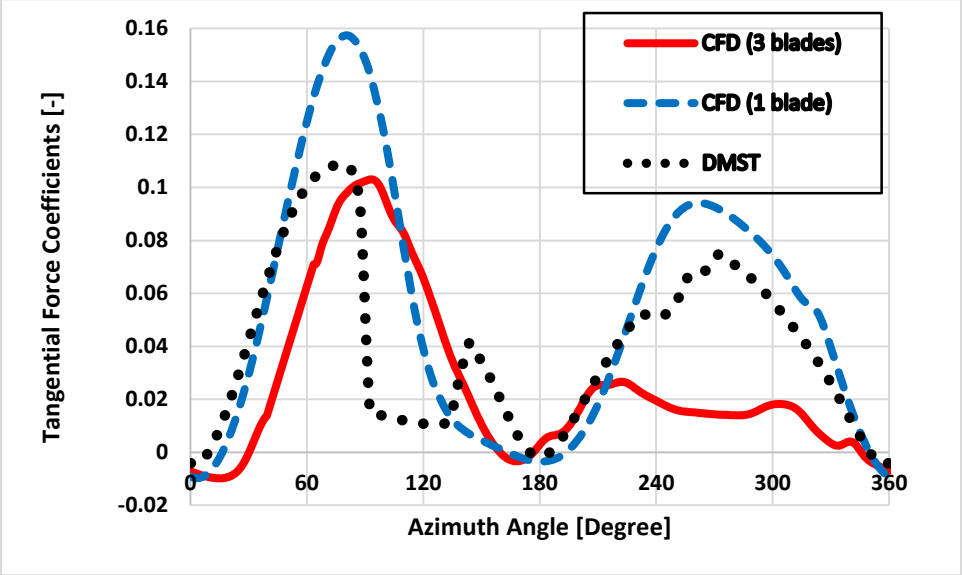

Figure 4. 15: Azimuthal Variation of the Tangential Force Coefficient (TSR = 3)

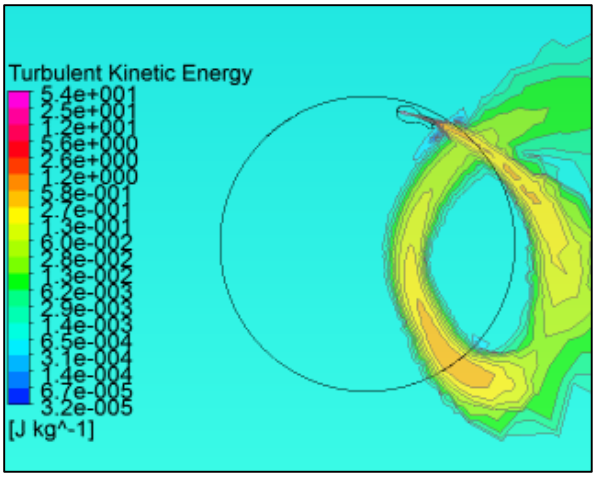

Figure 4. 16: Flowfield of a Single-Blade Rotor (a)

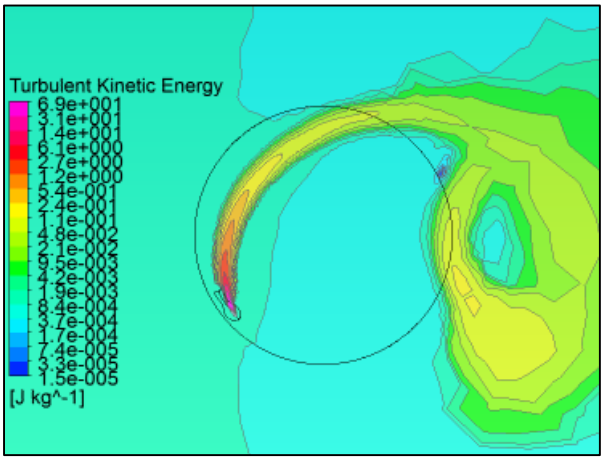

Figure 4. 17: Flowfield of a Single-Blade Rotor (b)

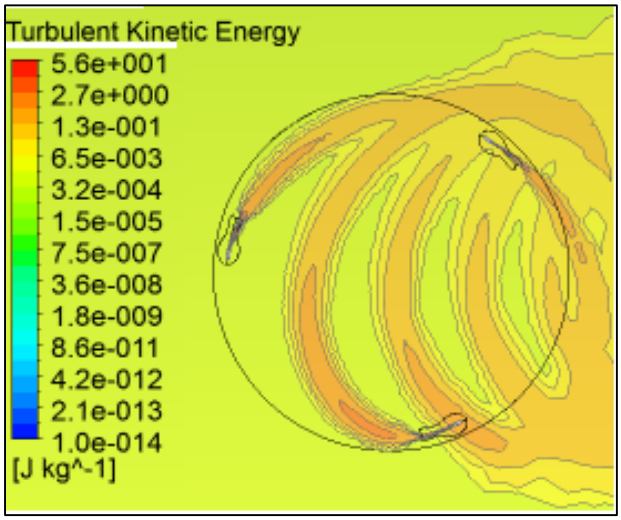

Figure 4. 18: Flowfield of a Three-Blade Rotor

First, it can be noticed through the interference factors in Figure 4.6 in the preamble section that the axial velocity undergoes a great deficit in the case of the three-blade rotor. This deficit is greater in the downstream region and is attributed to the wakes generated by the different blades in this region. For the given tip speed ratio, the single-blade rotor only experiences the effect of its own wake in a limited region, as shown in Figures 4.16 and 4.17. Besides, this interaction occurs after the intensity of the wake has substantially weakened as will be seen by the analysis of Figures 4.16 and 4.17. The plausibility of the wake effect interpretation is confirmed by the fact that the velocity deficit is almost non-existent in the zero angle of attack regions (i.e., 0, 180, and 360 degree azimuths). The variations of the transverse velocity component are related to the curving of the flow induced by the rotation and the presence of the swirling vortices.

Figure 4.13 portrays the variation of the angles of attack with the azimuth angle. It gives the geometric angle of attack, which is calculated using the tip speed ratio of the rotor and the local azimuth as defined in equation (46). The CFD calculated angle of attack instead uses the velocities obtained using the numerical probes described earlier. The DMST-computed angle of attack uses the velocities corrected by the interference factors as formulated in Chapter 2. These interference factors were presented in Figure 4.6 alongside the approached values using the CFD-computed velocities.

The geometric angle of attack is included not only as an overall reference but also to emphasize the reason why a single-blade rotor may not be very suitable for capturing the flow features in the downstream region of the rotor. This will further help formulate recommendations for improving the double multiple streamtube model.

Figures 4.14 and 4.15 give the normal and tangential force coefficients, respectively. Data are obtained from both CFD and DMST.

The flowfield snapshots in Figures 4.16 through 4.17 illustrate the swirling wake in the two types of rotors by presenting the turbulence kinetic energy. The first two

correspond to the single-blade rotor at two different times and the last corresponds to the three-blade rotor. The difference between the sets of images is noticeable and is at the origin of the velocity deficits that were presented earlier. This will also be helpful to interpret the results.

For instance, a single-blade rotor is only affected by its own wake (beside the wake of the tower and strut), while in the three-blade rotor the wakes generated by the other blades also play an important role. We further see by examining Figures 4.16 and 4.17 that at certain tip speed ratios, a blade can even not be significantly affected by its own wake because this one is quickly washed downstream by the mainstream flow.

As a result of the different wakes, a heavily disturbed flow is created in the downstream part of the three-blade rotor. The flow therein resembles a nearly dead flow region with wind gusts. A blade traversing this region experiences conditions somewhat similar to those of an aircraft flying into heavily turbulent storms. In this case, the dynamic stall and loss of performance is not necessarily attributed to high angles of attack but rather to the large turbulence structures of the flow.

The difference between the upstream and downstream parts of the rotor is reflected in the blade angles of attack shown in Figure 4.13. Indeed, in the upstream part, the CFD-computed angle of attack matches neatly the geometric values for both the single- and three-blade rotors. The reason for this concordance goes back again to the fact that a blade in the upstream section does not encounter the wake, for this one is washed downstream by the incoming stream before the next blade reaches the given region. This is particularly true for low solidity rotors. In the case of high solidity rotors, the apparent camber induced by the very rotation become non negligible. This induced camber plays a role in the determination of the angle of attack and blade loads. The behavior in the downstream section is completely different as a result of the preeminence of the wake and its vertical structures. The DMST-computed angle of attack is also relatively close to the CFD (single- and three-blade rotors) and geometric values in the upstream section. The small difference

observed therein may be associated with the pertinence of the choice for the CFD locations of the velocity probing points. In the downstream part, however, the DMST data is only approached by the single-blade CFD. The DMST model takes into account the total number of blades in calculating the interference factors. But the effect of the phase lag between the blades and that of the wake are not fully accounted for.

The consequences of this approximation are reflected in the force coefficients (Figures 4.14 and 4.15). The effect is more noticeable in the tangential component, which serves to compute the rotor performance. We notice again that the DMST values reflect more of the corrected single-blade approach as it is closer to the single-blade CFD values. We note in passing the sudden changes in the tangential force coefficient computed using the DMST model at low tip speed ratio. Similar observations were shown by Allet et al. in [6]. This may be associated with an interpolation error from the provided drag and lift polars. The order of the iteration in the DMST could also be a contributor to the convergence defect. Indeed, the present formulation uses fixed point iteration. A higher order iteration such as the Newton method could improve the convergence. It will thus be recommended that future works utilize at least second order accurate iteration methods. We also note a slight azimuthal shift for normal and tangential force coefficients from the DMST and single-blade CFD on the one hand to the three-blade CFD on the other. This is a result of the curving of the flow by the additional blades and the entrainment by them. The location of the "numerical probes" for determining the angle of attack can also be a contributor to the slight deviation.

A very important point to keep in mind while comparing the DMST and CFD is that the first is based on table look-ups and interpolations for the aerodynamic coefficients, while the latter operates with first principles calculations (i.e., Navier-Stokes equations in this case). The tables that are utilized are generally based on static aerodynamic data and by definition the interpolations are but approximations. The tables themselves were obtained by yet other interpolations. In fact, static experimental data were obtained for four

airfoils at a few Reynolds numbers. This data were then extrapolated to other airfoil profiles and interpolated in a range of Reynolds numbers using the PROFILE code [51].

In addition to the explanations presented above, the relatively large difference between DMST- and CFD-computed interference factors (section 4.1.2.) may, in part, come from the fact the CFD-computed velocities are taken at locations that minimize the direct effect of the blades themselves, as described above. Calculations using the blade loads (i.e., drag and lift coefficients) might well give better approximations at the cost of time.

The above discussion was carried out for a tip speed ratio of 3.0. Other tip speed ratios are presented below to cover a range of operating conditions. Thus, TSRs of 3.3, 3.5, and 4.0 are presented here. For these cases, the single-blade rotor is not included, but the geometric angle of attack is kept as a comparative reference.

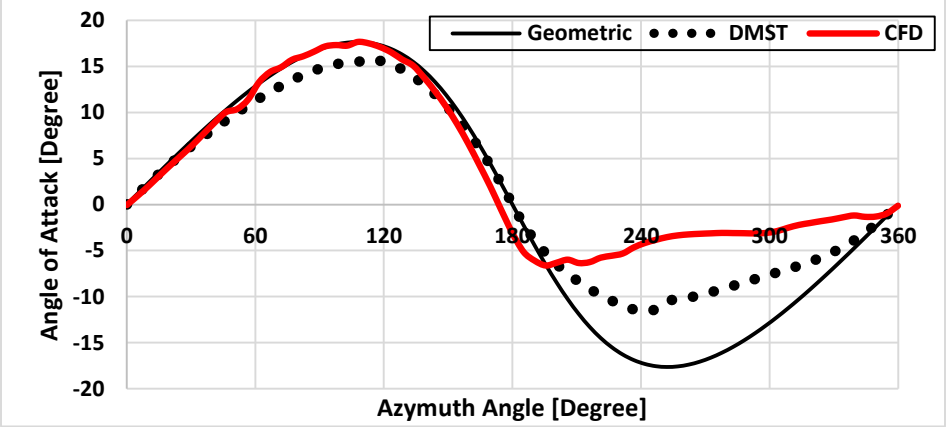

Figure 4. 19: Azimuthal Variation of the Angle of Attack (TSR = 3.3)

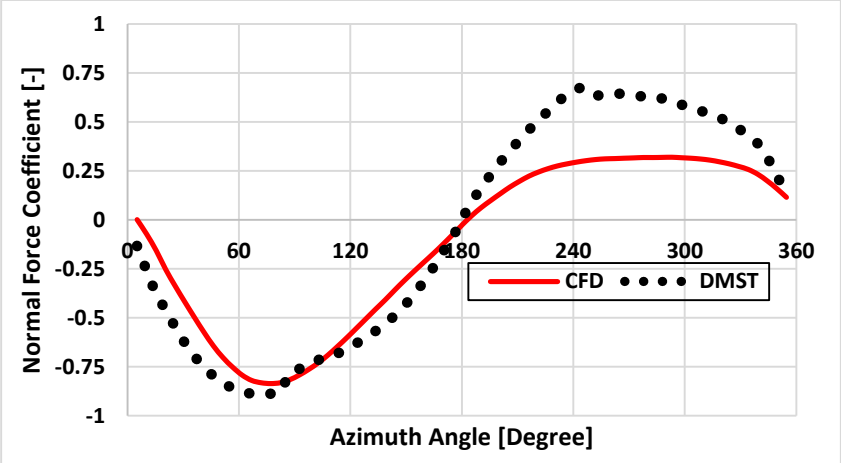

Figure 4. 20: Azimuthal Variation of the Normal Force Coefficient (TSR = 3.3)

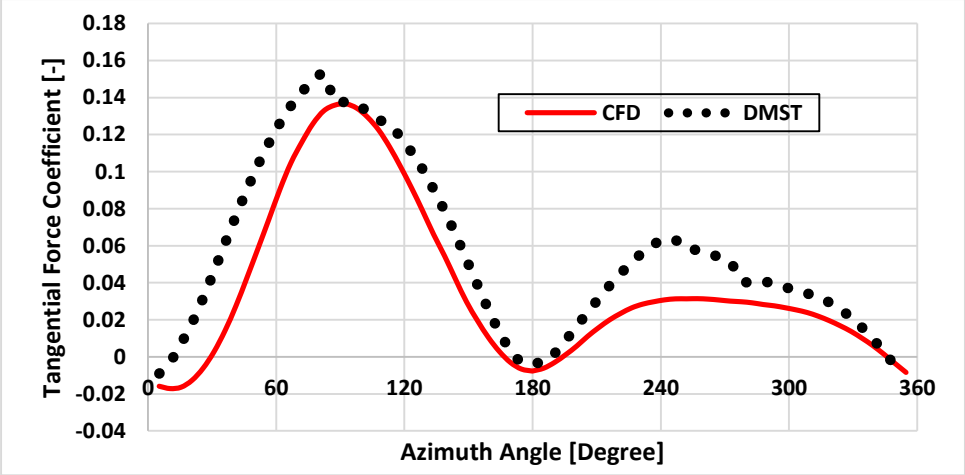

Figure 4. 21: Azimuthal Variation of the Tangential Force Coefficient (TSR = 3.3)

The tip speed ratio of 3.3 corresponds to the nominal operating point of the turbine. Figures 4.19, 4.20, and 4.21 give, respectively, the angle of attack and the normal and tangential force coefficients. First, the previously observed convergence defect at a lower TSR is no longer observed. The upstream section of the rotor corresponding to the azimuthal range [0, 180 degree] sees a good estimation of the angle of attack and the normal force coefficient. However, the tangential force coefficient is not captured with the same quality. In this case as well as in the previous TSR, this can be explained by the preponderance of flow curvature induced by the rotation of the blade.

In the downstream section of the rotor, the differences are attributed to the presence of the wake and the associated flow agitations. These phenomena are accounted for in the CFD but not so well in the DMST. Comparing the deviations in the upstream and downstream sections, and in particular for the tangential force coefficient, it can be concluded that in the downstream region the effect of the wake is more preeminent than that of the flow curvature.

The results corresponding to a TSR of 3.5 are presented in Figures 4.22, 4.23, and 4.24. These are followed by the output for the TSR of 4.0 in Figures 4.25, 4.26, and 4.27. In these sets of results, the general trends are the same as previously discussed for the TSR of 3.0. General trends emerge from the overall results. First, the deviation of the DMST-computed angle of attack is more accentuated in the upstream section as the tip speed ratio increases, while this difference is attenuated in the downstream part. This is due to the increasing preeminence of the rotation velocity component in the upstream part. On the other hand, the downstream part sees this effect progressively leveled by the wake. In addition, in the CFD simulations, the location of the velocity probing points discussed earlier may also contribute to the deviation between the two approaches. In fact the location of these points half distance between any two blade contribute to making the CFD-computed angles of attack close to the geometric value in the upstream section of the rotor.

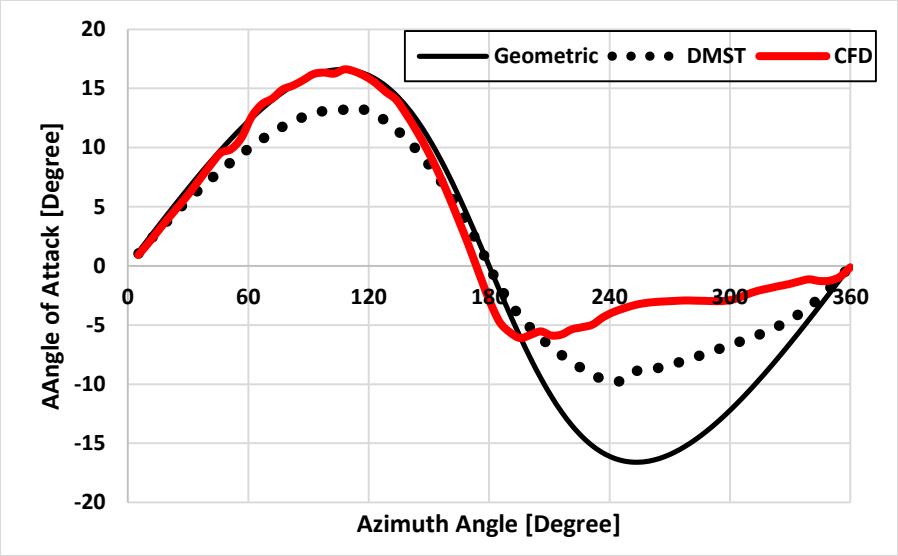

Figure 4. 22: Azimuthal Variation of the Angle of Attack (TSR = 3.5)

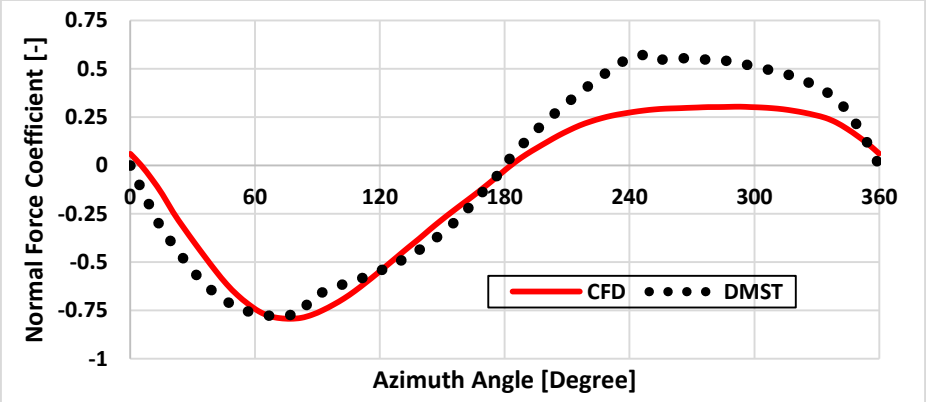

Figure 4. 23: Azimuthal Variation of the Normal Force Coefficient (TSR = 3.5)

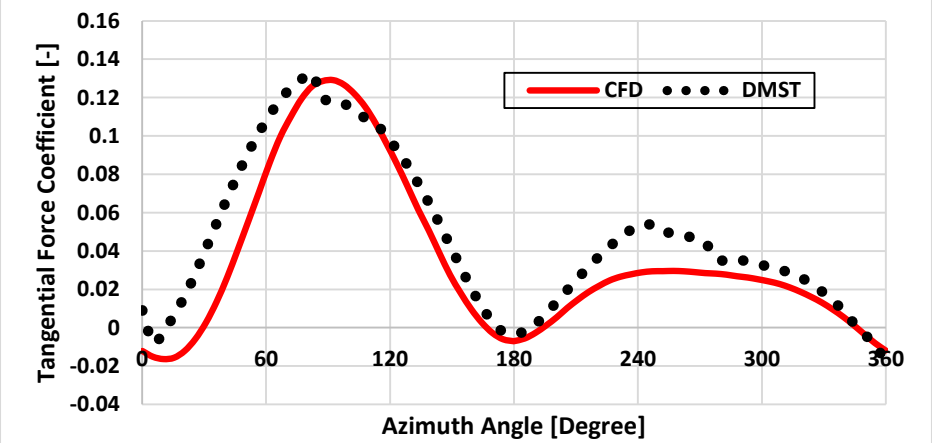

Figure 4. 24: Azimuthal Variation of the Tangential Force Coef. (TSR = 3.5)

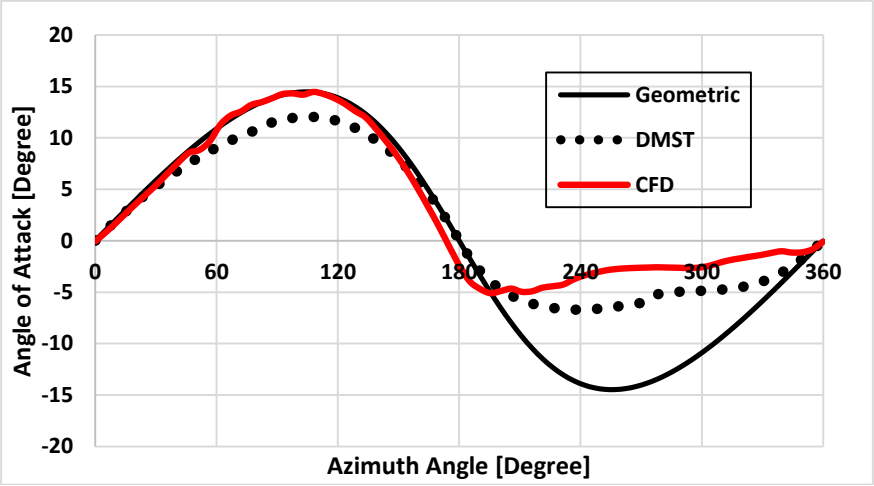

Figure 4. 25: Azimuthal Variation of the Angle of Attack (TSR = 4)

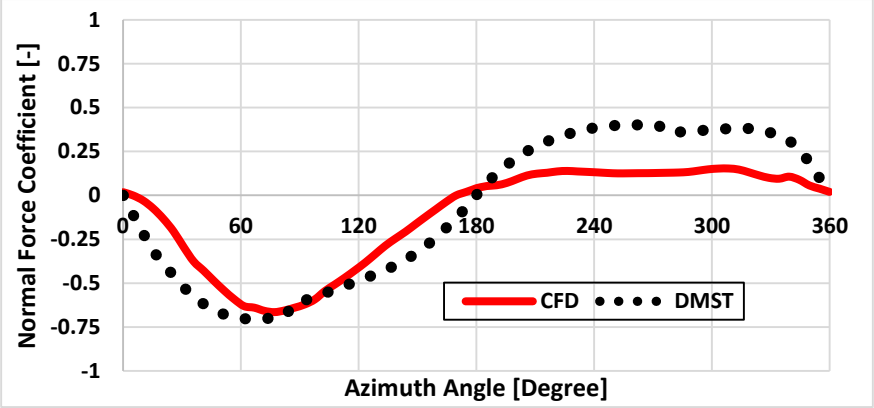

Figure 4. 26: Azimuthal Variation of the Normal Force Coefficient (TSR = 4)

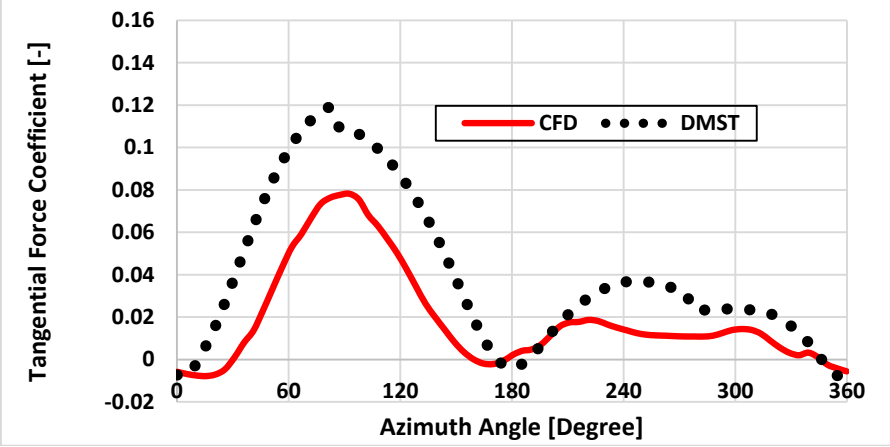

Figure 4. 27: Azimuthal Variation of the Tangential Force Coefficient (TSR = 4)

We also conclude from the aforementioned results that the normal component is not significantly affected by the flow curvature. For instance, this component is already of relatively large amplitude (compared to the tangential component), and the velocity change induced by the curvature is negligible with respect to the normal component. This component is thus mainly affected by the velocity deficit due to the induction in its upstream part and the combination of the induction and the wake factors in the downstream region.

The tangential component on the other hand is more affected by the curvature (in addition to the wake and other phenomena) because of its smaller amplitude. For instance the tangential force coefficient is more than an order of magnitude less than the normal force coefficient. This is manifested in the TSR 4.0 case, where the deficit is equally noticeable across the cycle with the exception of the near-zero-angle-of-attack regions. As it happens, there is no curvature effect in these regions because the velocity induced by the rotation is in the same direction as the main flow stream. It can also be noted that high tip speed ratios are synonymous with high reduced frequencies. So as this frequencies increase, the dynamic stall models may start to show limitations. The deviation of the customized Sheng model that was found to arise at high TSRs is thus an element that will contribute to this difference.

The present analysis discussing the aerodynamics and performance of the SB-VAWT shows the viability of the DMST to be used as a substitute to the CFD during the screening phase of the investigation. The findings are summarized below.

4.4 Summary

In this work, the double multiple streamtube (DMST) model is compared to the computational fluid dynamics (CFD). A description of the computational settings and processing is provided.

The investigation first discussed the effect of the dynamic stall model on the solution. For this purpose, the Gormont empirical dynamic stall model was compared to the results of static stall calculations. Subsequently, a modified Sheng model was introduced to better represent the dynamic stall phenomenon in the context of vertical-axis wind turbines. The different approaches were compared to the CFD solutions, and the modified Sheng approach was retained as best representing the solution for single-element blades in VAWT rotors. The model was found to be more precise in moderate and low tip speed ratios and tends to deviate for higher TSRs.

In the second part, aerodynamic loads obtained using CFD and DMST with the customized Sheng model were analyzed. Flowfield analyses were utilized to support the interpretations.

Some of the key points in the discussions are:

1. The preeminence of the customized Sheng model over the empirical Gormont model and static stall calculations,
2. The better accuracy of the predicted results for low and moderate tip speed ratios and some deviation for higher TSRs,,
3. The effect of the wake structure on both normal and tangential force components,
4. The effect of flow curvature on tangential force and thus on the power output,
5. The little dependence of the normal force component on the flow curvature.

And in terms of the approach, it is worth noting that:

1. Although the DMST takes into account the total number of blades in calculating the induced velocities, it doesn't fully account for the wake effect. For instance it doesn't render the phase lag between the blades;
2. The location of the velocity probing points may slightly affect the value of the angle of attack and thereafter offset the dynamic stall hysteresis cycle;
3. For comparing the DMST and the CFD, it may be worth computing the (CFD)-interference factor starting from the loads instead of the aforementioned probe velocity. This approach is more accurate and needs a more methodical implementation.

CHAPTER 5

INVESTIGATION OF TWO-ELEMENT BLADES

The general characteristics of vertical-axis turbines were described in the previous chapters. Previous chapters discussed the challenges pertaining to VAWTs and current techniques utilized to improve the performance. The modelization of the dynamic stall addressed and the aerodynamic loads of the blades described.

In this chapter, two-element blades are investigated as a means to alleviate the dynamic stall and improve the rotor performance. The chapter is structured around the following points: the characteristic features of airfoils suitable to vertical-axis wind turbines (VAWTs), the parametric study of the dual-element blade in order to meet these characteristics, the performance, and the associated flow aerodynamics.

5.1 Characteristics of VAWT Airfoils

Although improving the aerodynamics of the rotor struts can help enhance performance, this contribution may be marginal compared to the blades' aerodynamics. Thus the design of suitable blades is a field of investigation on its own. The characteristics of the blades must meet the specific requirements of the rotor design. In fact, the size of the turbine and the projected operating conditions will determine the choice of the blade. Examples of the efforts conducted in this regard include the work by Saeed et al. [152]. They developed an inverse airfoil design for a low-speed SB-VAWT application using a panel method coupled with a boundary-layer scheme. Their conclusions emphasized the performance improvement that was thus obtained. They also underscored the difficulty of predicting the aerodynamic loads for low speed and/or high angles of attack. This difficulty is associated with the high adverse pressure gradients and flow separation on one hand and the formation of laminar separation bubbles on the other hand. Tatinemi and Zhong [184]

conducted a numerical investigation of unsteady low-Reynolds number flows over airfoils. They studied the separation of the boundary layer, the dynamics of the shed vortices, and the effects of the laminar separation bubbles.

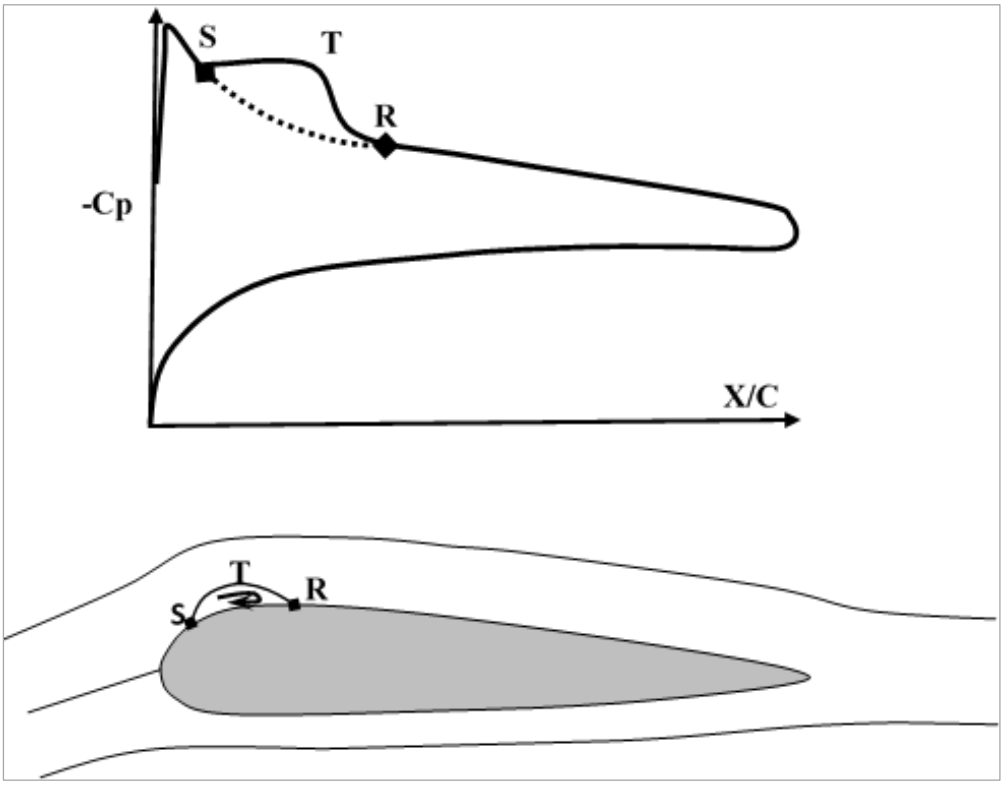

Figure 5.1: Illustration of the Laminar Bubble Separation and its Effect on the Pressure Coefficient (S=Separation of boundary layer, **T**=Transition from laminar to turbulent boundary layer, **R**=Reattachment of the boundary layer**)**

This phenomenon of laminar bubble separation corresponds to the detachment of the boundary layer from the airfoil while it is still laminar. The laminar-to-turbulent transition occurs in the detached "boundary" layer. This early separation is caused by the inability of a less energetic flow to withstand the relatively strong adverse pressure gradients. Then, reattachment occurs under certain conditions. In fact, depending on the location of the point of separation, the "boundary" layer may fail to reattach to the airfoil. In either case, whether

or not the flow reattaches, there is energy losses associated with this phenomenon. This causes performance degradation of the airfoil at low Reynolds numbers.

The characteristics of wind turbine airfoils were investigated by Wolfe and Ochs [207]. These authors also studied the laminar-to-turbulent transition and emphasized the importance of its location on the airfoil.

The laminar separation bubble and its effect on the pressure distribution are illustrated in Figure 5.1. Phenomena like these make the low-Reynolds number flows encountered by the VAWT blades very complex. We previously emphasized the geometrical design parameters for the airfoil in order to enhance performance. For instance, the literature survey discussed the effects of the airfoil type – its camber and/or thickness [e.g., 47, 68, 69, and 144] – among other factors. Each geometrical feature will influence the aerodynamic characteristics. In the context of VAWTs, the blade camber can be chosen so as to make the adverse pressure gradient mild. The moderate adverse pressure gradient on both the pressure and the suction sides can be overcome by the weak turbulent boundary layer, making the airfoil less sensitive to surface roughness and less prone to separation. This type of airfoil will have relatively high lift (and high stall angle) and large negative pitching moment. A thicker airfoil will have better starting torque and also present larger drag buckets. The thickness also improves the structural strength. Large leading edge radii also contribute to making the airfoil less sensitive to roughness in addition to making the stall milder. On the other hand, shaper trailing edges reduce the minimum drag, but they are more difficult and costly to manufacture. All the geometric features and associated active and/or passive controls made to the blades serve the main purpose of finding the most suitable aerodynamic characteristics that meet the design requirements.

Before presenting the aerodynamic criteria for good airfoil performance, it is worthwhile to note that the airfoil aerodynamic properties can be reasonably characterized by five variables, namely,

i. The thickness-to-chord ratio,

ii. The camber,

iii. The Reynolds number,

iv. The surface contamination such as the (leading edge) roughness and/or the deposits,

v. The stall behavior, which depends strongly on the previous four points.

Form these variables, the desirable aerodynamic criteria are crystalized in the following nine points:

1. Large stall angle at small or moderate Reynolds numbers,
2. Wide drag bucket,
3. Small zero-lift-drag coefficient,
4. Large lift-to-drag ratio,
5. Large maximum lift coefficient,
6. Large negative pitching moment,
7. Delayed deep stall property,
8. Small sensitivity to roughness, and
9. Small level of noise generation.

In the criteria above, the small zero-lift-drag coefficient is required for the starting capability of the turbine. The large stall angle at low Reynolds numbers and the wide drag bucket criteria are meant to ensure the minimization of the region in which the blade is stalled and thus contribute negatively to the driving torque. They also contribute to overcoming the rotor inertia as well as to avoiding the power coefficient "dead band."

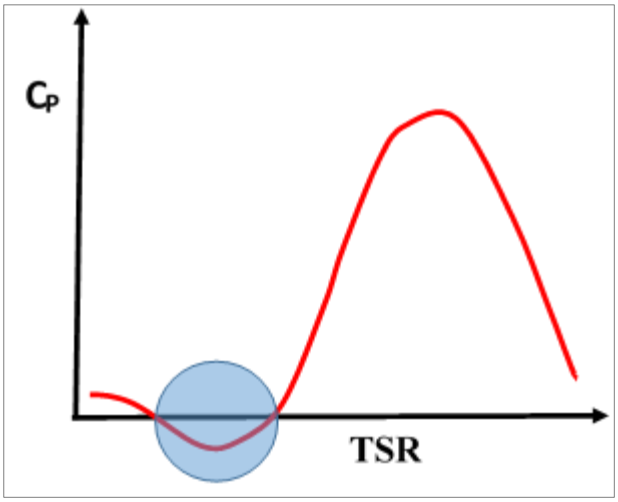

Figure 5.2: Sketch of Cp with a "Dead Band" in blue

The "dead band" is a range of low tip speed ratios in which the power coefficient is negative as shown in Figure 5.2. A turbine that presents this characteristic is inherently non-self-starting and must incorporate a starting device such as a Savonius rotor. The two criteria being discussed address this issue by removing the "dead band" altogether.

Continuing with the criteria list, the large lift-to-drag ratio, large maximum lift coefficient, and large negative pitching moment all pertain to the better performance of the turbine. But it will be seen later that each of these quantities need to be large but not necessarily the largest possible. So, a trade-off needs to be made with other considerations.

The deep stall delay can be considered to go along with the large stall angle criteria. The angle at which the deep stall occurs is a function of the Reynolds number as well as the leading edge radius. When the stall occurs, it is important for it to be gradual rather than abrupt so as to minimize the negative contribution to the driving torque. Indeed, an abrupt stall is associated with a more drastic reduction of the lift-to-drag ratio and yields more vibrations and structural fatigue.

The sensitivity to surface roughness is listed for completeness but is not included in this numerical study. The need to minimize this sensitivity arises from the fact that the turbine operates under conditions (dust, debris, etc.) that would cause the boundary layer

to become turbulent. The roughness then decreases the maximum lift while the zero-lift-drag increases. This phenomenon becomes more pronounced as the Reynolds number increases.

Finally, to minimize noise generation, sharp trailing edges are recommended for single-element blades. The same option is also retained for multi-element blades. Additional noise can be generated because of the flute effect in the gap between the components.

In the following section a parametric study is conducted, accounting for the aforementioned aerodynamic criteria except for the last two, namely, the roughness sensitivity and the noise level.

5.2 Parametric Study of the Dual-Element Blade

After describing the aerodynamic criteria that serve to determine the most suitable blade, a parametric study is conducted in this section. The parameters consist of the chord lengths of the two elements, the size of the gap between them, and their relative orientation. Figures 5.3 and 5.4 are sketches of dual-element blades and the different parameters that were considered. For the purpose of the parametric study, the total chord is taken to be the sum of the chords of the two elements at the exclusion of the gap between them, as illustrated in the figures. The size of the gap is represented in Figure 5.3 by the length "**d.**" However, to account for the relative position of the elements, this gap is decomposed into its "$\mathbf{d_x}$" and "$\mathbf{d_y}$" components, as shown in Figure 5.4. The configuration in this figure shows a case where "$\mathbf{d_x}$" and "$\mathbf{d_y}$" are, respectively, positive and negative.

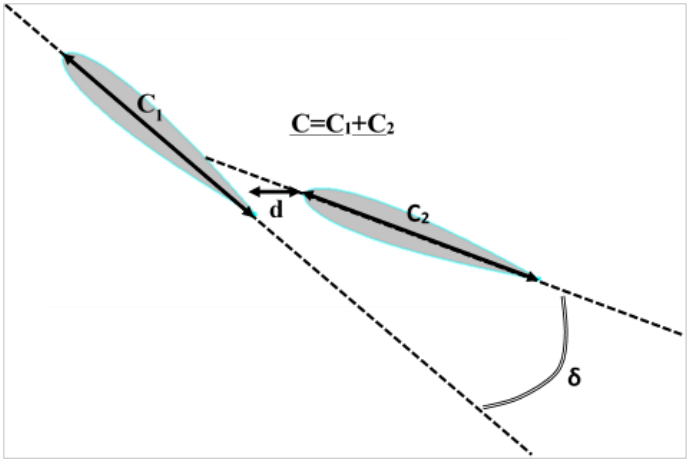

Figure 5.3: Parametric Study Configuration (a)

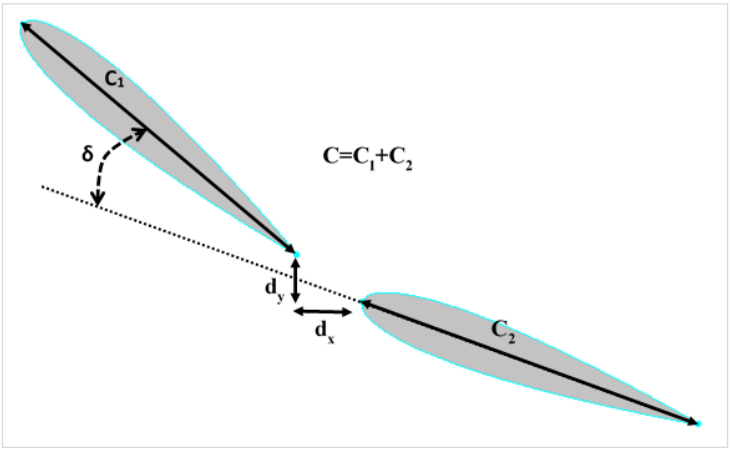

Figure 5.4: Parametric Study Configuration (b)

The parametric study was conducted by analyzing various configurations to cover a representative portion of the parametric map. In general all the parameters except one are kept constant. The other parameters are later refined based on the optimal value thus found. Some of the configurations that were studied are compiled in Table 5.1.

The parametric study is divided into two segments. Cases 1 through 6 in Table 5.1 emphasize the lift and drag coefficients (C_L, C_D) as well as the moment coefficient (C_m). The lift-to-drag ratio is also examined. These characteristics are analyzed as functions of the angle of attack. The corresponding results are presented in Figures 5.5 through 5.11.

In study cases 7a through 10d, the moment coefficient was dropped from the analysis. The variation of the lift-to-drag ratio as a function of the angle of attack was still examined alongside the C_L vs. C_D polar diagrams. A summary of the results is given in Figure 5.12.

Table 5.1: Parametric Settings

	C_1/C	**d/C**		**Λ**
		d_x/C	**d_y/C**	
Case 1	0.5	0.05		[0°, 10°, 20°, 30°]
Case 2	0.5	[-0.075, ... 0.125]		20°
Case 3	[0.2, 0.4, 0.6, 0.8]	0.025		20°
Case 4	0.5	0.04		[0°, 10°, 20°, 25°, 30°]
Case 5	0.5	[-0.075, ... 0.15]	[-0.025, -0.0125]	25°
Case 6	[0.3, 0.4, 0.6, 0.7]	[-0.075, ... 0.15]	[-0.025, -0.0125]	25°
Case 7a	0.5	0.05		[5°, 10°, 15°, 20°, 25°, 30°]
Case 8b	0.5	[0.025, 0.05, 0.075]		25°
Case 9c	0.5	0	[+/-0.025, +/-0.05]	20°
Case 10d	[0.3, 0.4, 0.5, 0.6, 0.7]	0	-0.05	25°

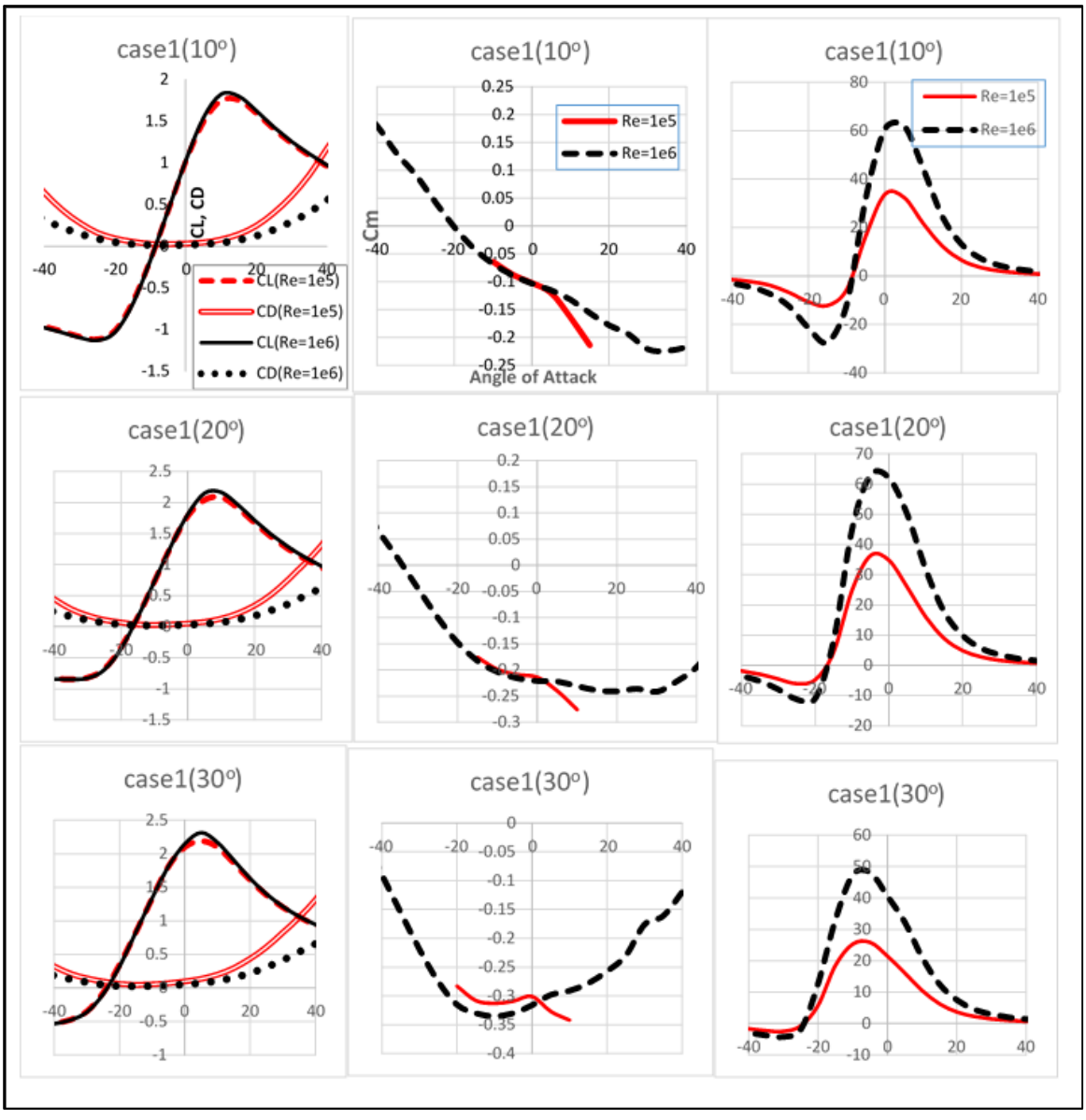

Figure 5.5: Case 1 – Variation of the Relative Orientation

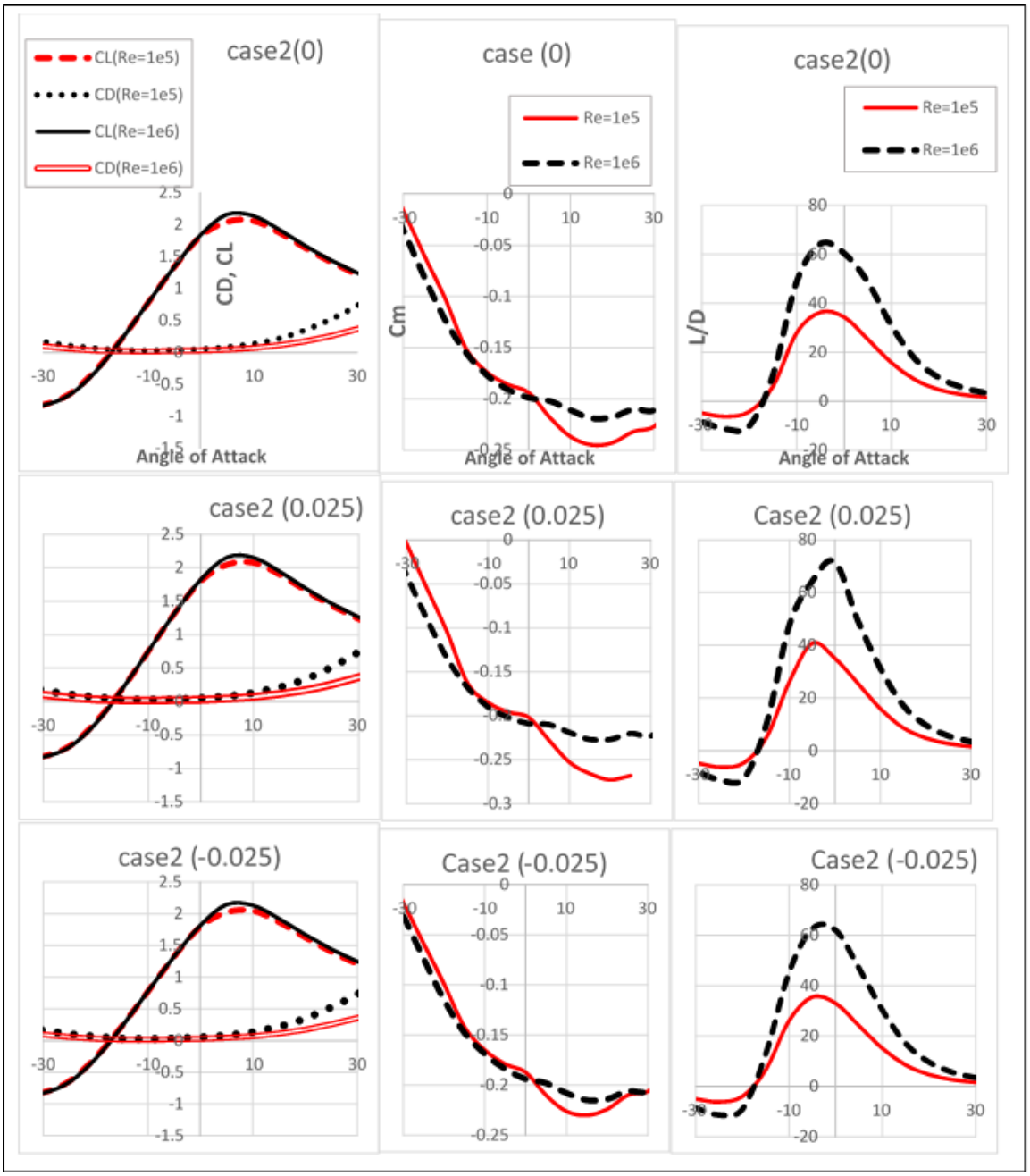

Figure 5.6: Case 2 - (1) Variation of the Gap Size

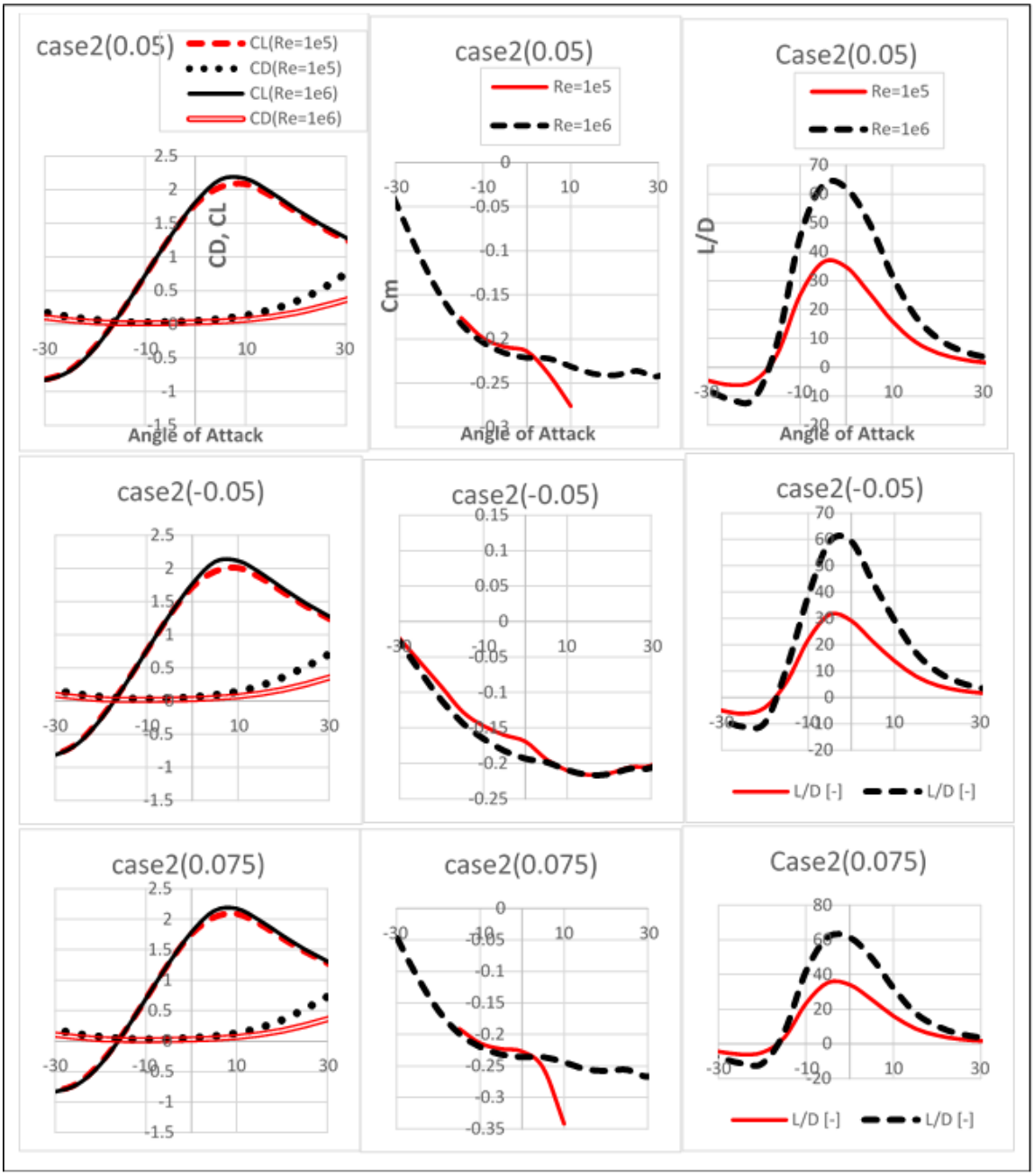

Figure 5.7: Case 2 - (2) Variation of the Gap Size

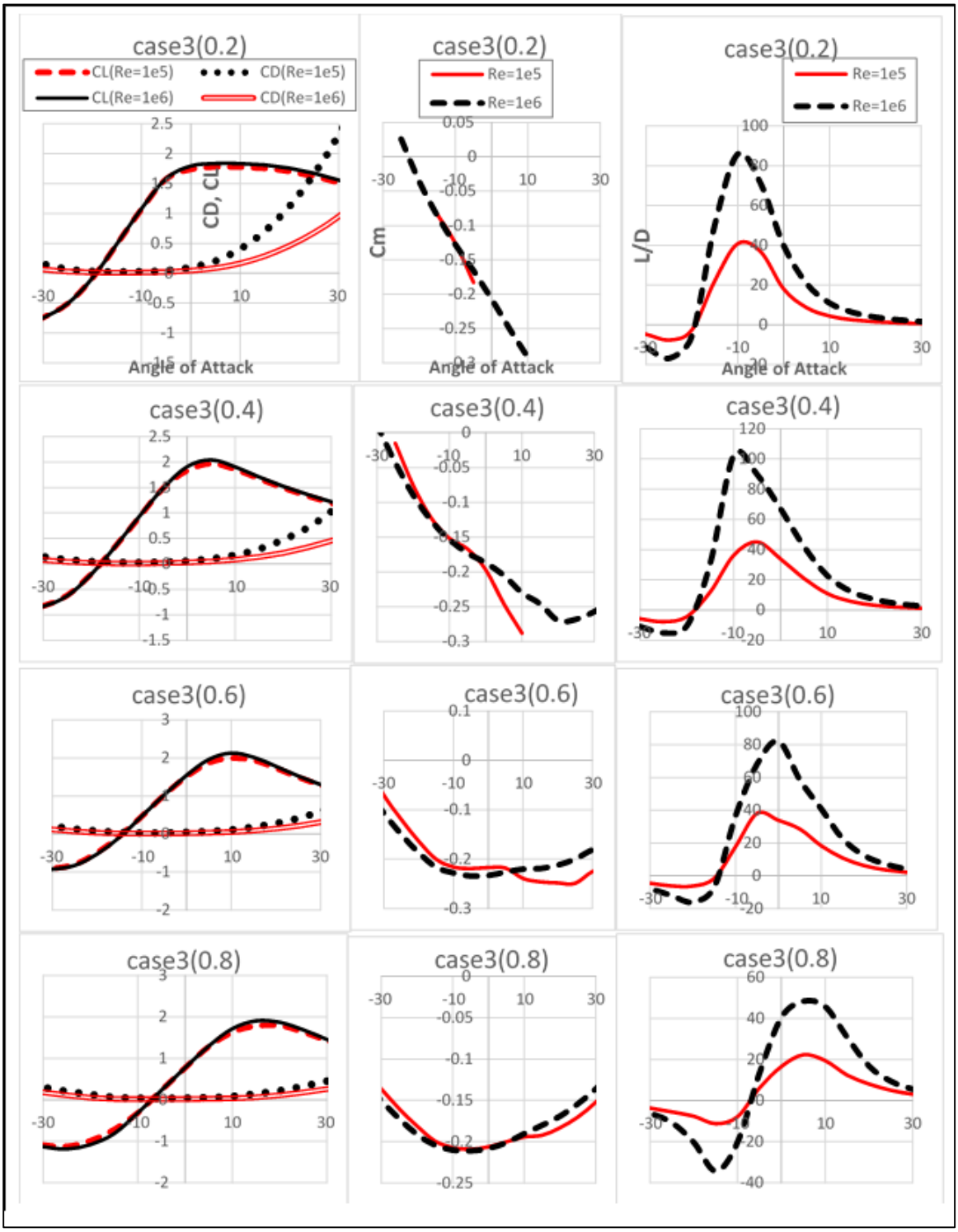

Figure 5.8: Case 3 – Variation of the Relative Size of the Elements

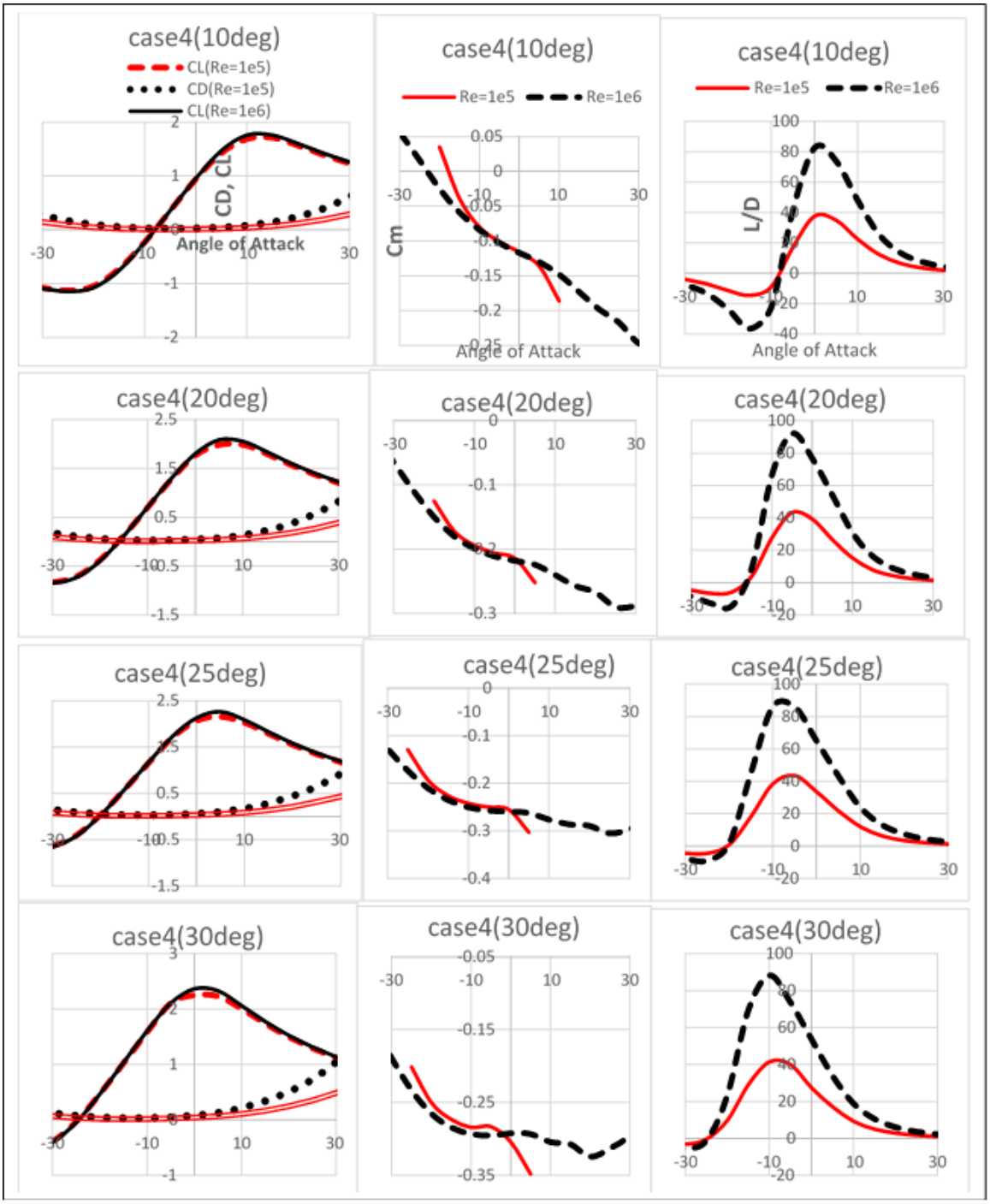

Figure 5.9: Case 4 – Variation of the Relative Orientation

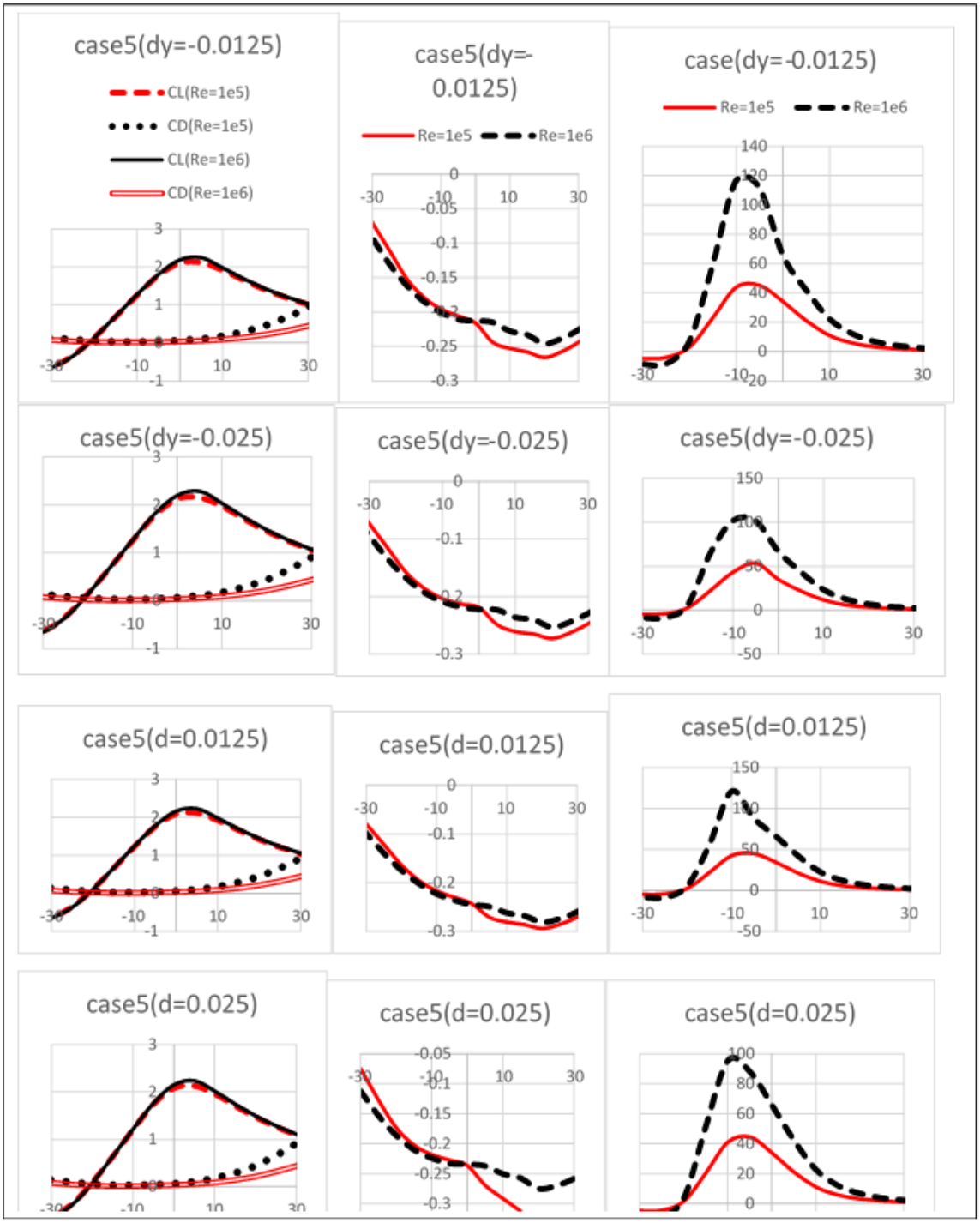

Figure 5.10: Case 5 – Variation of the Gap Size

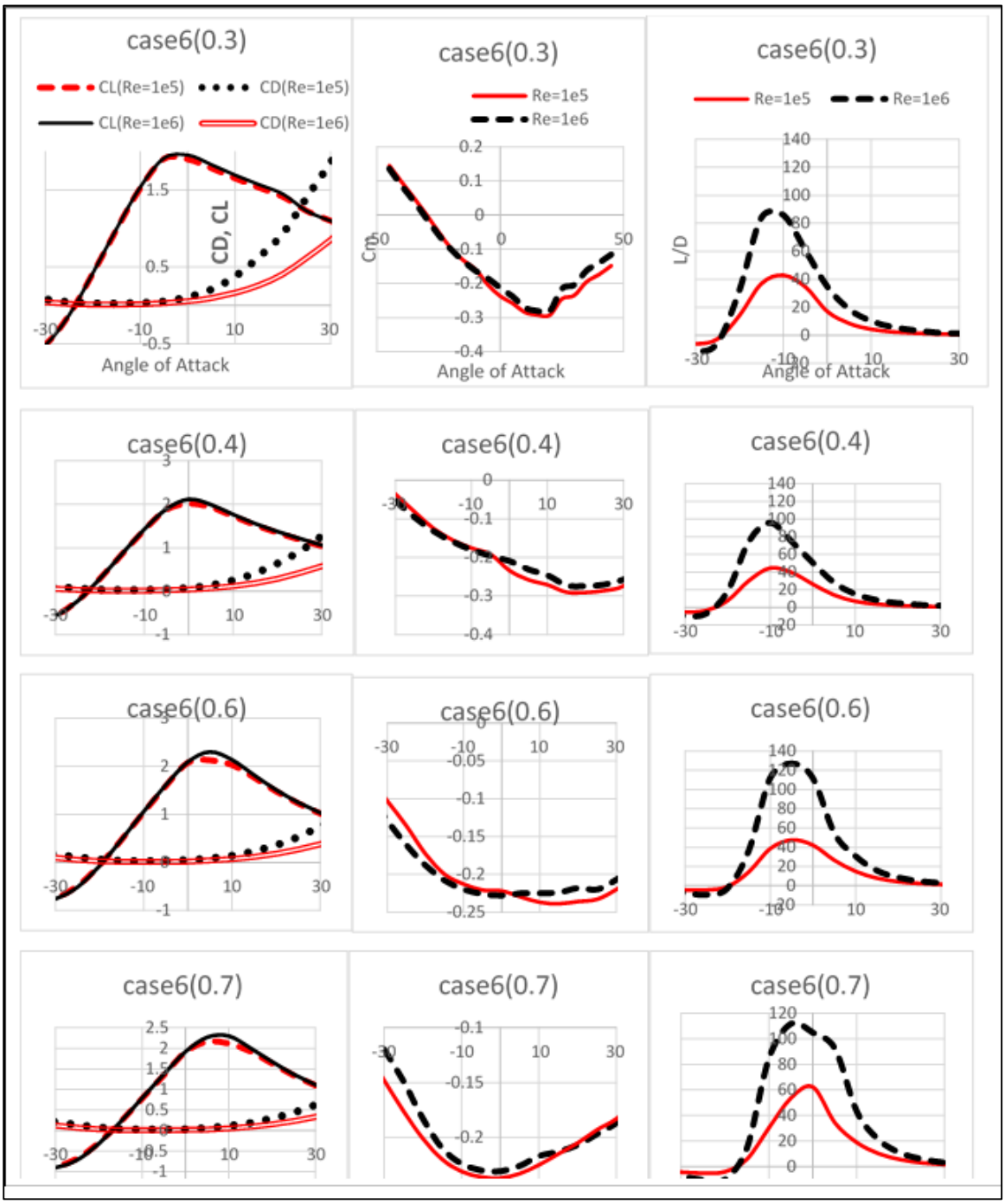

Figure 5.11: Case 6 – Variation of the Relative Size and the Gap size

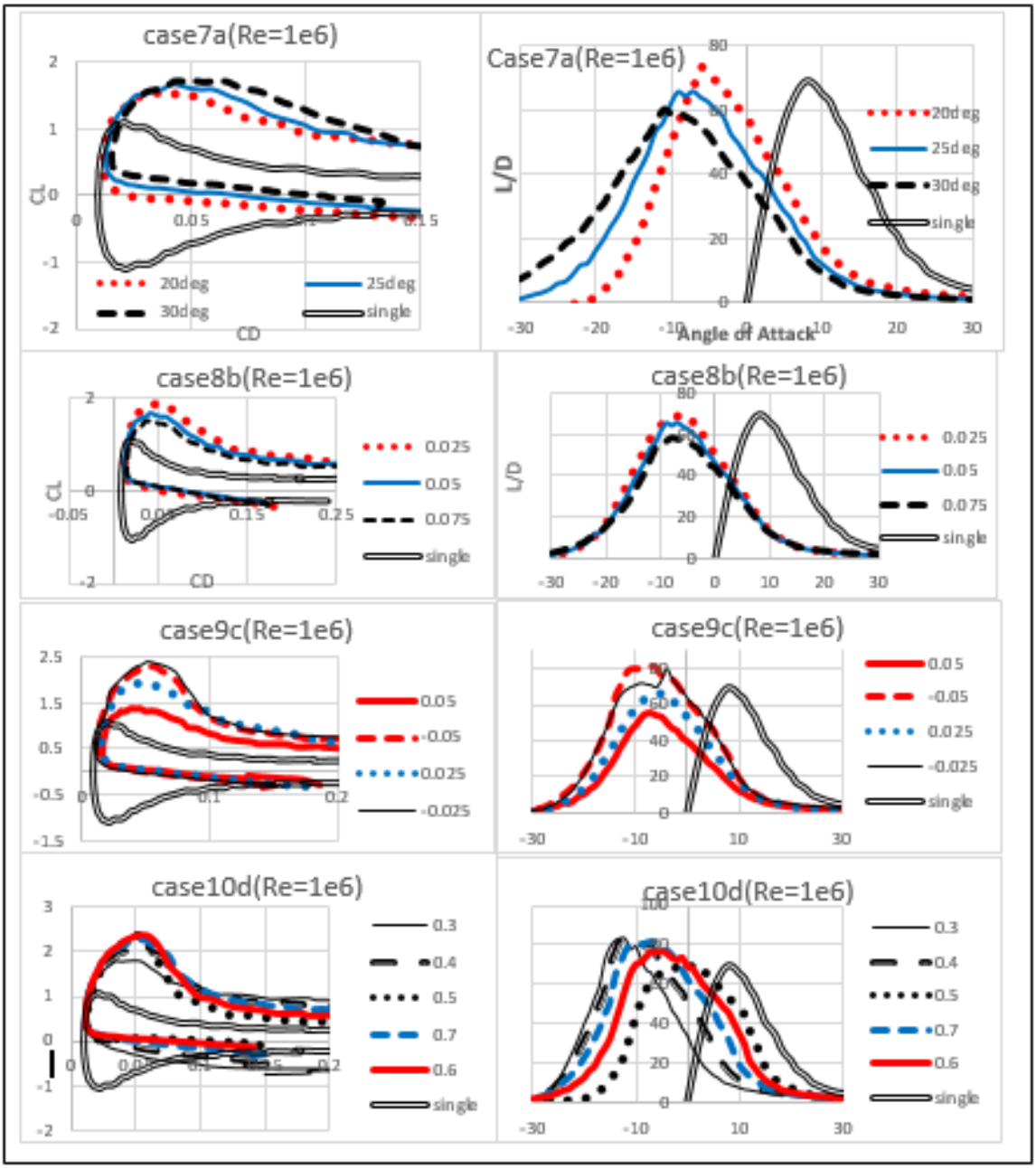

Figure 5.12: Cases 7a-10d – Refined Parametric Studies

The effects of the relative orientation were studied in cases 1 and 4 with a gap size of 4% and 5% of the total chord, respectively. The two elements had the same size. Each case was investigated at multiple Reynolds number. Two Reynolds numbers that are representative of the VAWT operation shown in these results. From the results of these two sets of cases, Figures 5.5 and 5.9 show that the moment coefficient (C_m) is improved. C_m is in fact negative over almost the entire range of angles of attack. This fulfills the performance stability criterion described in the previous section. The lift-to-drag ratio also attained values larger than the single-element blade. However, the largest values are concentrated in regions of angles of attack where the blade doesn't spend much time. This would result in sudden and large amplitude variations. Such a phenomenon is not desired.

The zero-lift drag coefficient is almost equal to the overall minimum drag coefficient. We observe that the zero-lift angle of attack moves toward higher negative angles of attack as the relative orientation between the elements is increased. It is also noticed that the range of angles of attack with positive lift-to-drag ratio increases with the relative orientation. However, the maximum value attained by the lift-to-drag ratio follows the inverse trend. This means that at almost any given angle of attack, there is descent self-starting potential. The drawback is that the full-potential torque may be reduced.

Because of this downside and the previously mentioned sudden and large amplitude variations, these configurations cannot be retained. Other configurations are investigated. Every new configuration builds upon the previous findings for improvement.

Cases 2 and 5 present the effects of the gap size for two identical elements with relative orientations of 20^o and 25^o, respectively. In the configuration sets of case 2, the gap is represented by one parameter: the algebraic distance between the elements. The results (Figure 5.6-7 and 5.10, respectively) indicate that small negative gaps give slightly better lift-to-drag recovery. The centering of the angles of attack interval is not affected. The gap was then represented by two Cartesian components. The corresponding parametric analysis is presented in case 5. Some configurations therein show a substantial recovery of

the lift-to-drag ratio compared to the cases already studied. However, the sifting of the optimum angles of attack still persists.

In case 3, the effect of the relative size of the elements at fixed gap and fixed orientation is examined. The results (Figure 5.8) show that a large size disparity is detrimental to the overall aerodynamic properties. The gain in lift observed in some configurations coincides with substantial increase in drag. The overall gain is almost non-existent. This can be explained by the fact that a small element can be completely immersed in the wake of a much larger element. Under these conditions, the contribution of this element to the lift-to-drag ratio is negative. This also affects performance stability. It can be observed for instance that the variation of the moment coefficient is very steep when the size disparity is important.

In case 6, a combination of three parameters is examined. The relative size of the elements is considered alongside the two gap components. The results are presented in Figure 5.11 for the most conclusive set of gap parameters and various element sizes. It results from this analysis that elements of similar size yield the most convincing results in terms of combined lift-to-drag and moment considerations.

Refined analyses are conducted as specified in cases 7a through 10d. The configurations are presented in Table 5.1 and the results in Figure 5.12 for a Reynolds number of 10^6. The findings from the previous preliminary parametric analysis are highlighted here. In the last case (10b), we note a re-centering of the lift-to-drag profile around the zero angle of attack for similar blade elements. The maximum lift-to-drag ratio is not significantly higher than that of the single-element blade. However, the range of angles of attack with high lift-to-drag ratios is almost doubled.

Considering the results of this parametric investigation, the configuration presented in case 10d with similar blade elements will be retained as a candidate for the remaining investigations.

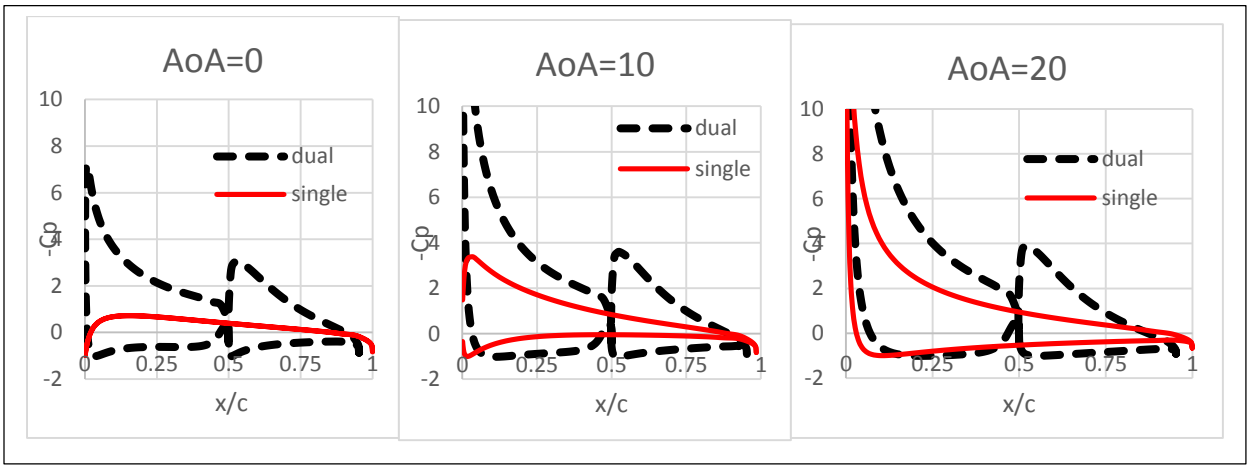

Figure 5.13: Single- vs. Dual-Element – Pressure Distributions

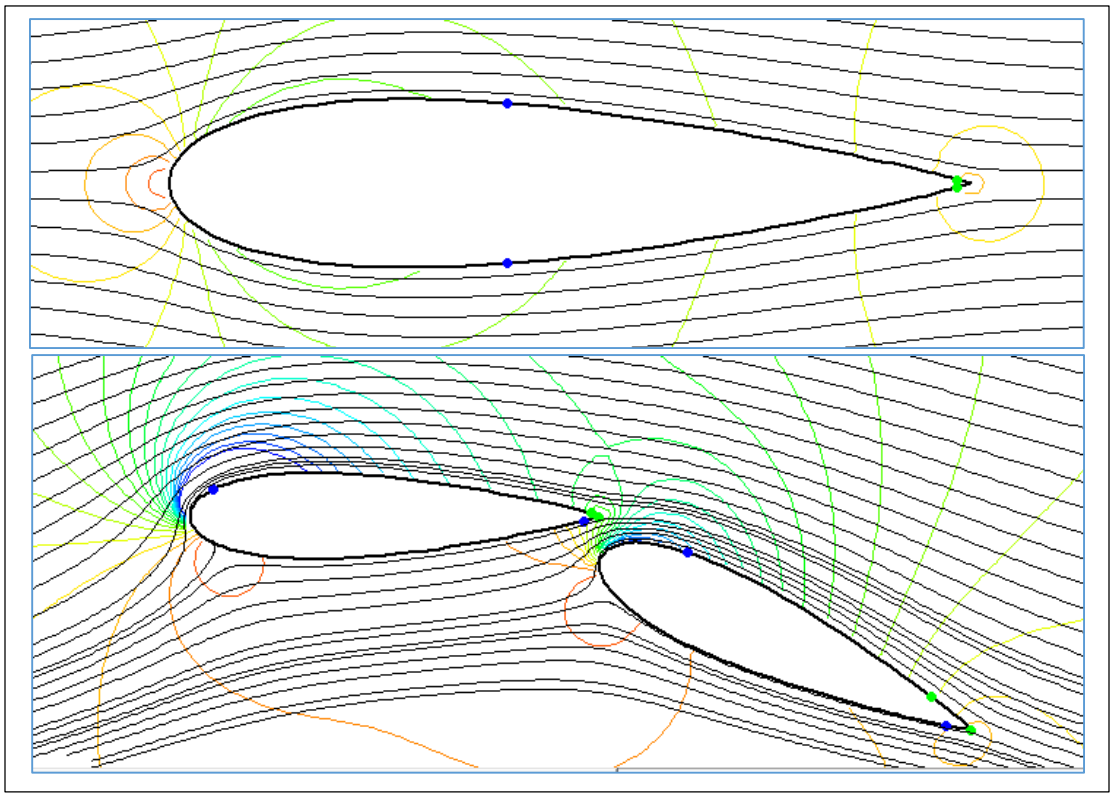

Figure 5.14: Single- vs. Dual-Element – Flow Stream

Before continuing with the performance evaluation, the pressure distribution of a dual-element blade is compared to that of a single-element for three angles of attack (Figure 5.13). The flow-field comparison (Figure 5.14) is presented at a given angle of attack in order to illustrate the analysis.

First, we notice the changes in the pressure distribution. This change will be reflected in the lift and other aerodynamic properties. Observing in particular the zero angle of attack pressure distribution, we notice that even the leading element has a profile of a pressure coefficient that is not representative of a zero angle of attack. This is so despite the element having a zero angle of attack based on the freestream velocity. This phenomenon is created by the flow perturbation due to the presence of the rear element. For instance, the presence of the rear element induces a slowing down of the flow and a bypass effect around this element. These processes start far in the upstream and becomes more marked as the flow approaches the given element. In this dual-element configuration, the front element is in what will be termed the region of influence of the rear element. Conversely and more obviously, the rear element will be affected by the presence of the front element.

The interactions between the elements is sought to be utilized for improving the overall characteristics of the blade and by extension the performance of the rotor.

5.3 Rotor Performance and Analysis

One of the goals of this work has been to make the case for the use of dual-element blades in vertical-axis wind turbines as a means to improve performance. The present researcher has presented in [10] and [11] preliminary findings on the subject.

In the current work, in a nutshell, this process has consisted so far of:

1. Studying the physics of SB-VAWTs with single-element blades,
2. Comparing the DMST model with CFD,

3. Validating the use of the DMST as a means to evaluate the performance, and
4. Conducting a parametric study on the dual-element configuration to find a suitable candidate.

The following step in this investigation is to determine the performance of the rotor. The rotor has the same specifications as the reference open-field rotor with one exception: each blade is now made of two elements, as described earlier.

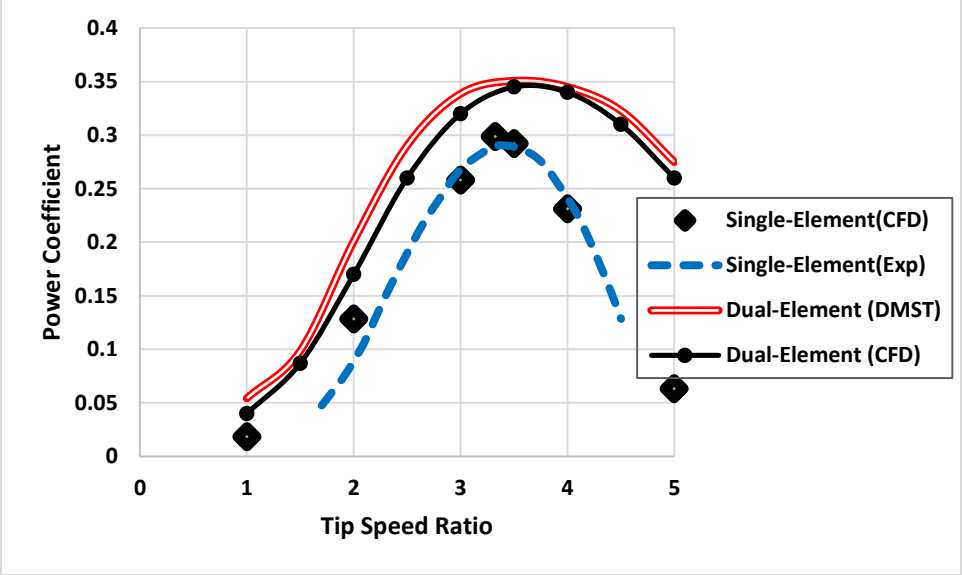

Figure 5.15: Wind Turbine Performances

The power coefficient, which is the ratio of the turbine power to the free-stream wind power, serves as representation of the performance. The calculations were made using the double multiple streamtube model and complemented with the CFD. The results are presented in Figure 5.15. The power coefficient for the reference turbine is also given for comparison. A number of positive conclusions can be drawn.

1. Performance enhancement is observed over the entire range of investigated tip speed ratios.

2. The range of tip speed ratios with a significant power coefficient is expanded. This means that the turbine can operate under more diverse conditions.
3. The variation of the power coefficient near its optimal value is less abrupt. In fact a quasi-plateau is observed. This means the operation at/or near the optimum TSR is more stable and less subjected to changing conditions. This also means that the turbine can operate at different TSRs and still produce a significant amount of power.

   The second type of operation is introduced because as opposed to HAWTs, which can be tuned to operate at the maximum C_P by use of the pitch control, the simplicity and rugged construction intended for these SB-VAWTs make them susceptible to operate away from the maximum C_P. A Weibull-averaged C_P ($C_{P,WA}$) is introduced to represent this operation. The details are presented in connection with the economic analysis in Chapter 6.
4. Relatively high Cp values are recorded for low tip speed ratios. This suggests that the "dead band" described in section 5.1 may be eliminated. As a result, the self-starting capability is improved.

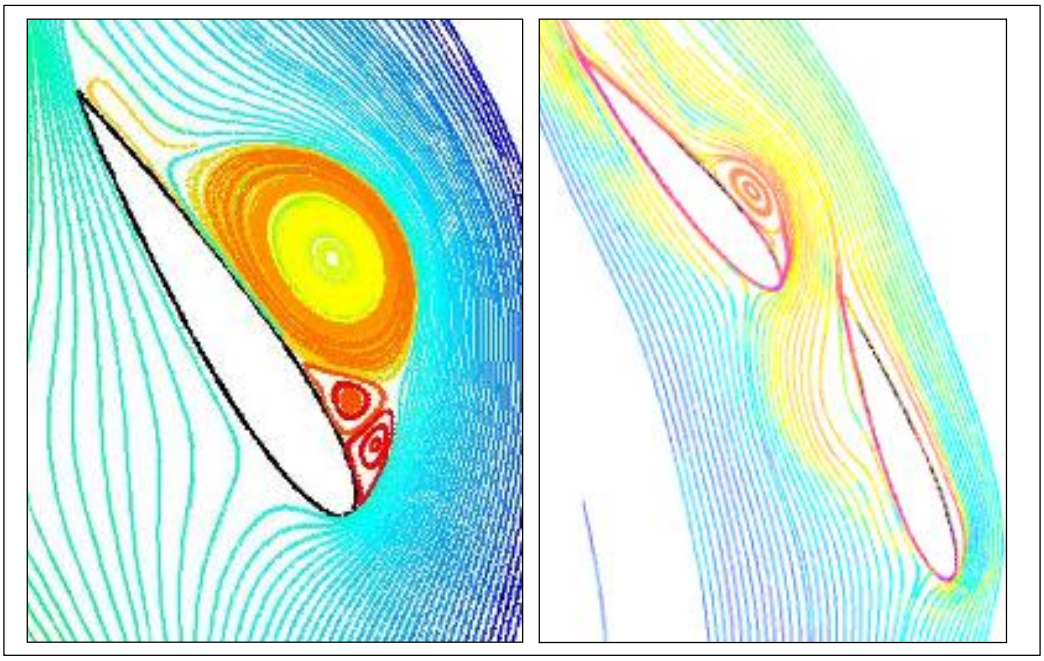

Figure 5.16: Streamlines around Single- and Dual-Element Blades at 230º Azimuth

It has been shown in the conclusion of the parametric study that the interaction between the two elements of the blade modifies the aerodynamics of the system. The changes that each element undergoes were investigated by this author in [10] and [11]. The contribution of each element was also quantified. The analysis of the flow structure around the blades was utilized for the interpretation of the results. Some of the results are reproduced here for illustration and completeness.

The key points that contribute to the changing of performance related to the geometry on the one hand and to the flow interactions on the other hand.

The purely geometric consideration consists of properly orienting the blade elements so that when one stalls the other is still operating under attached flow conditions. In this way, at least part of the blade is contributing to the propulsive force. Thus, it minimizes the performance loss due to pure drag. This is illustrated in Figure 5.16 where the single-element blade is completely stalled, while the flow is still overall attached in the dual-element configuration.

The interactions are of a more complex nature. They can be referred to as blade-blade-wake or blade-blade-flow interactions. The interactions therein are inter-coupled. However, they can be uncoupled for the purpose of the analysis.

In addition to the geometric position and orientation, the local angle of attack of a given element is affected by the changing of the flowfield as a result of the presence of the other element. This aspect was explained in the previous section and illustrated in Figures 5.13 and 5.14.

There is also the also the effect of the direct wake of one element on the other. For instance the rear element is directly affected by the trailing edge vortex of the front element. It may also be affected, to a lesser extent, by the leading edge vortex as well. For these reasons, it was discussed earlier that it is better to have two elements of comparable sizes. Otherwise, one runs the risk of being completely immersed in the wake of the other.

The gap region sees a vortex-vortex interaction that modifies the structure of the flow around the elements in this region and beyond. The primary finding in this regard was presented by this author in [10]. This interaction and its effects on the blade components are of a complex nature. Further and more thorough investigations need to be dedicated specifically to this subject.

In order to grasp the phenomenon, it is best to start with the dynamics of the shed vortices in a single-element blade. In a rotor composed of single-element blades, the leading-edge shed vortices rotate in the same direction as the rotor itself. The trailing-edge shed vortices rotate in the opposite direction. Going back to the dual-element, these two type of vortices "cohabit" in the gap between the elements. The dynamics of each vortex are modified not only by the presence of the solid body that is the other element but also by a counter-rotating vortex. The presence of the solid body prevents the full spreading of the vortex and changes its dynamics. The presence of the counter-rotating vortex may create a dead-flow region depending on the relative strength of each vortex.

Finally, the interaction between these vortices at times causes flow reattachment. This, also, is illustrated in Figure 5.16. We notice indeed the reattachment of the flow in the rear element as result of the dual-element configuration.

Further flowfield analysis is given in Figure 5.17. The streamlines are captured at different azimuth for a tip speed ratio of 3. Number of aspects are noticeable in the upstream and downstream sections of the rotor. In the upstream sections, these include the fact that:

- At least one element is operating under attached flow conditions,
- The vortex interactions between the components are favoring the reattachment of the flow, and
- The equivalent blade (i.e., the two elements and the region between them seen as one entity) has an overall attached flow.

Similar features appear in the downstream section but they are not as manifest as they are for the upstream part. There also exist a region within which the flow either doesn't reattach or the amount that reattaches is negligible. This will be the subject of one of the recommendations for future work.

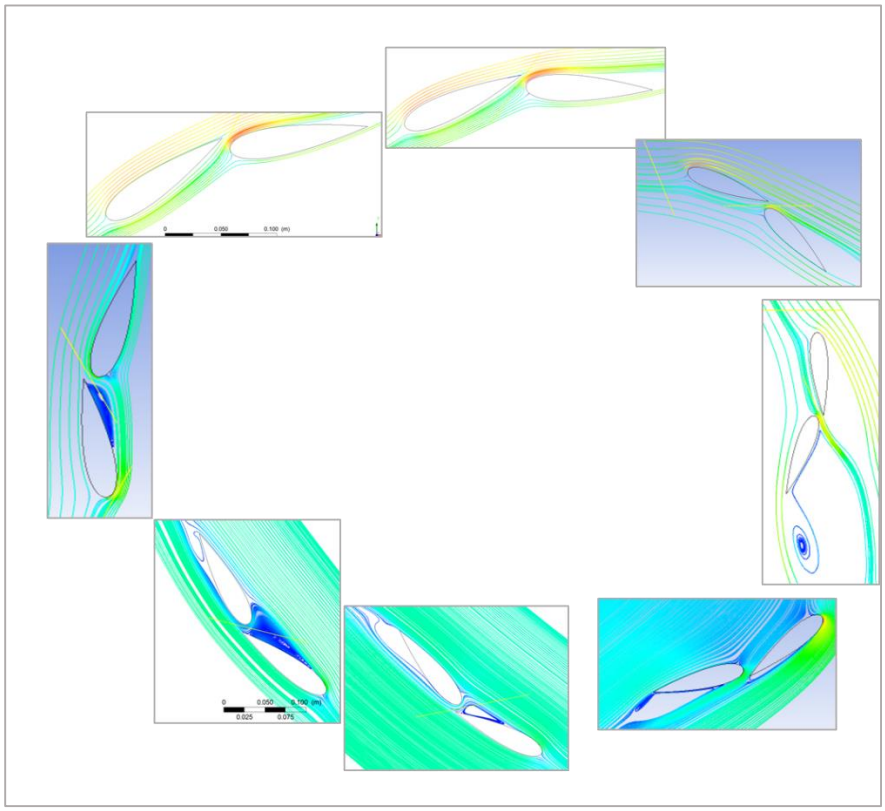

Figure 5. 17: Flowfield Analysis – Streamlines at Representative Azimuths

The investigations in this chapter have led us to detail the desirable blade characteristics for application to VAWTs. A parametric study was conducted to identify a suitable dual-element configuration. The performance of the corresponding rotor was then evaluated. Finally, an analysis was conducted to explain the performance enhancement and to interpret the observed features.

After investigating the dynamics, design, and performance of the vertical-axis wind turbine, an economic analysis is put forward as proof of financial viability.

CHAPTER 6

ECONOMIC ANALYSIS

The present chapter discusses the economic viability of the novel dual-element concept. In order to be truly meaningful, the economic analysis need to be contextualized. It will, for instance, depend on the environmental and socio-economic characteristics of the site of operation. Thus this chapter presents the selected site at first. An analysis of the energy needs and the current energy sources and prices is then conducted. The regional wind capacity is then investigated. The local public policy pertaining to renewable energies in general and wind energy in particular is also examined. Thereafter the economic analysis itself is elaborated upon.

6.1 Site Selection

The economic development very often correlates with the access and use of energy. In fact, access to energy and its proper utilization are the main drivers for economic growth. The correlation between energy usage and economic development is an indicator of industrialization and mechanization of primary sector activities. An analysis of world regional energy consumption per capita (Figure 6.1) and regional gross domestic product per capita (Figure 6.2) shows a striking contrast between developed and underdeveloped regions. The situation in Africa is of particular concern. In light of this comparison, its underdevelopment can be associated in part with the little exploitation of the energy resources. We note in passing that the data as expressed per capita is somewhat biased for Asia and Oceania. Indeed, while Asia is highly populated (China and India being the two largest contributors to the world population), Oceania is less populated. Thus the per-capita figures could in some sense misrepresent the actual economic vitality of these regions.

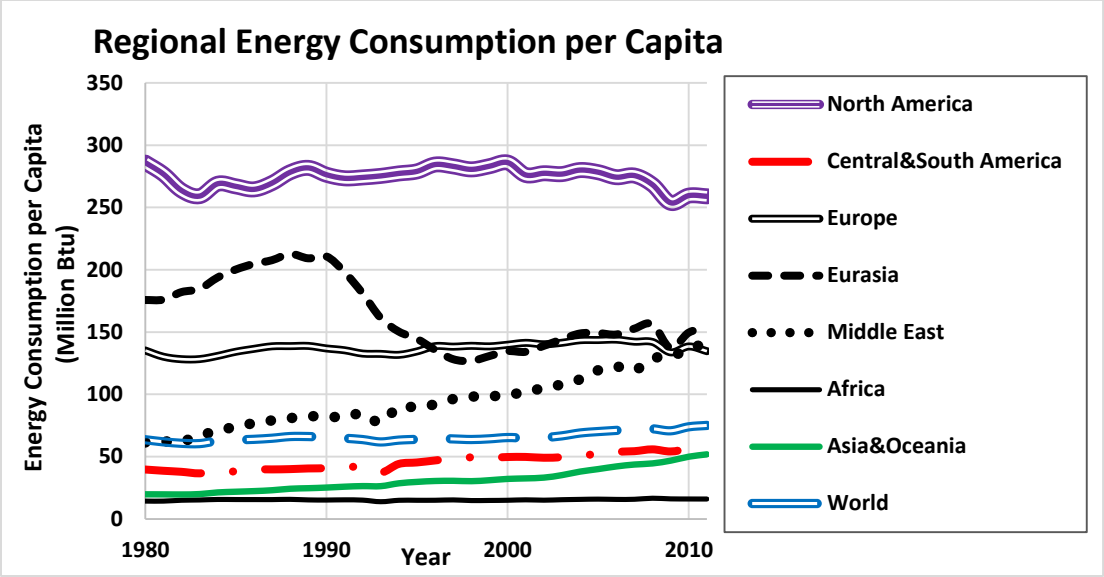

Figure 6.1: World Regional Energy Consumption per Capita

(Source: US Energy Information Administration)

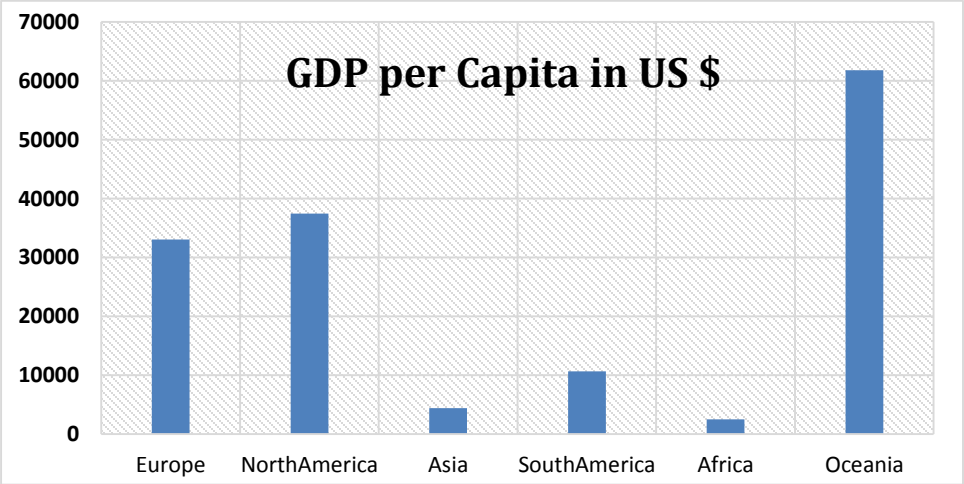

Figure 6.2: Regional GDP per Capita (2013)

Returning to the matter of the African continent, the sub-Saharan region paradoxically concentrates many of the poorest countries and a plethora of natural resources at the same time. These resources are either untouched or mostly exported to industrialized nations. The share that is transformed locally is marginal in most of these countries. No development can be achieved unless the current trend is reversed. This begins with

progressively building a local industry that is capable of transforming the resources. This can only be accomplished with sustained energy production and management. And all available energy sources need to be utilized in the most effective manner. In the present work, we pay special attention to the Western African country of Senegal (see Figure 6.3). The Great Cost – North West region – (see Figure 6.4) has the best wind energy potential in this country. The operation site of the wind turbines will thus be within this region. Before expounding on the wind potential itself, it is important to analyze the energy need and the current energy sources and prices.

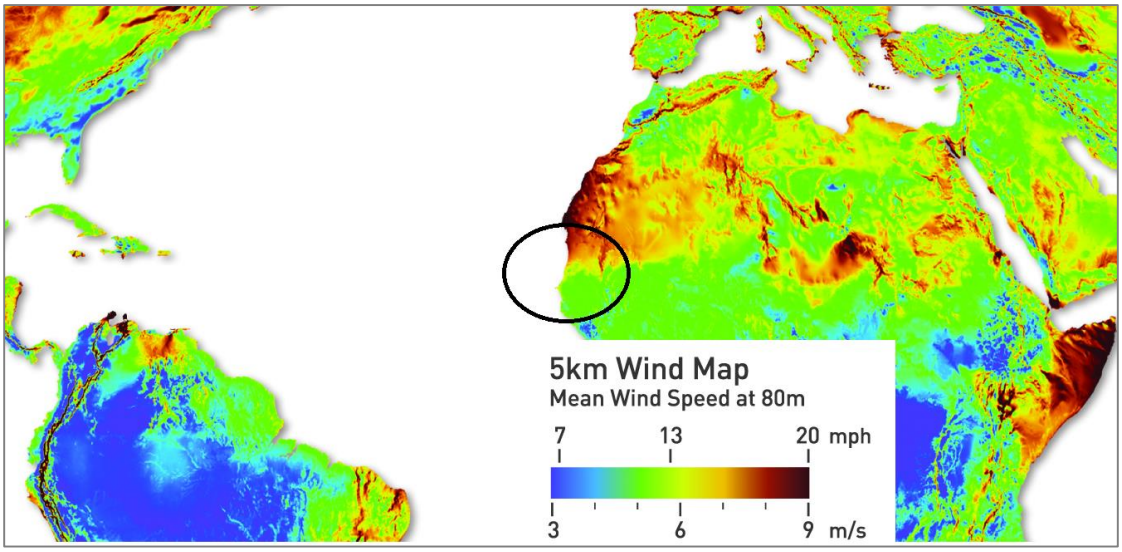

Figure 6.3: Global Wind Map with Senegal Region Circled (Source: 3Tier Wind Map)

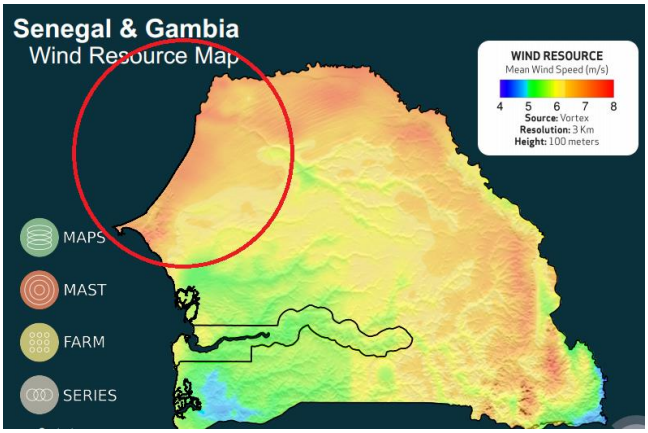

Figure 6.4: Wind Map of Senegal with the Great Coast Circled (Source: Vortex FDC ©2014)

6.2 Energy Need, Current Sources, and Prices

According to the African Development Bank, about one-third of the West African population is now in the middle class. This demographic is defined as the ability to spend between US$2 and US$20 per day [2]. The noted progress is linked to better access to technology and better use of natural resources. It was also noted that these improvements are being stunted by an energy sector that is not performing as it should. For example, a gap of about 40% is noted between the supply and demand of electricity [65].

Bazilian et al. [16] emphasized the need to drastically improve energy production. Thus, in order to meet the 2030 mark for universal energy access, the annual growth rate of power generation should be no less than 13% as opposed to the 2% observed for the last couple of decades. Eberhard et al. [44] noted that sub-Saharan countries spend only about 0.75% of their GDP on power infrastructure, while 2.25% is taken up by operating costs. Because of the obsolescence of the infrastructure, about 21% of the energy is wasted in transmission losses. It is projected here that about 5% of the national GDP needs to be invested in energy-related infrastructure to meet the challenge of the 2030 universal energy access.

In order to meet the aforementioned challenge, it is essential that the energy profile of the region be clearly defined. This will then give an indication of how to approach the problem. An overview of the energy profile of Senegal is given in Table 6.1. The data therein show the great renewable energy potential. Yet this potential is not utilized. The dependence on imported oil is also striking. This dependence puts the economy in a vulnerable position, subjecting it to price increases and by extension to the regional and global geopolitics.

Table 6.1: Senegal Energy Profile (Source: IRENA 2012**)**

Total Primary Energy Supply (TPES)	157.9 PetaJoule
Share of Renewables (RE) in the TPES	54.8%
Electricity Generation	2,858 GWh
Share of RE in the Electricity Generated	10.2%
Electrical Capacity(2008)	548 MW
Share of RE in the Electrical Capacity	0.4%
Energy Self-Sufficiency	55.5%
Fuel Imports	US$ 1.2 Billion (23.2% of exports)

The total primary energy supply (TPES) in 2010 consisted mainly of biomass (47%) and oil products (48%). However, other energy sources such as coal, hydro, natural gas, and solar are progressively being developed since the early 2000s. And more recently, wind energy projects have been designed. All existing wind project are based on the horizontal-axis technology. As can be seen from the table, the use of biomass and petroleum products is still predominant. This jeopardizes already fragile forests on one hand and endangers the environment as a whole on the other; thus the need to invest to cleaner energy solutions is clear.

The main electricity provider remains the national power company SENELEC. Its interconnected grid supplies electricity to about 40% of households. But some industrial complexes produce their own power. This frees them from the instability of the power supply. The electrification rate is growing with new connections to the main grid as well as off-grid stations. In the case of the grid-connected project, the energy is sold to the power company at a wholesale rate of US₡14 per kWh, and the price to the customer is about US₡22 per kWh. This can be put into perspective by comparing it with other regions. For instance, the prices to the customer in South and East Asia is US₡4 per kWh and US₡7 per kWh, respectively [78].

The breakdown of energy consumption by sector is another indicator of economic vitality. Table 6.2 presents this decomposition by activity sector. This breakdown is

indicative of the limited industrial development and little mechanization of the agricultural sector. Renewable energy sources can be developed for local consumption, and the surplus can be made available for sale by connection to the main grid.

Table 6.2: Energy Consumption by Sector (Source IRENA 2012**)**

Households	54%
Transportation	30%
Industry	14%
Agriculture and Public Services	4%

6.3 Renewable Energy Sources

Senegal has great potential for renewable energies, as shown in Table 6.1. With the Senegal and Gambia rivers, the hydropower potential is about 1.4 Giga-Watts. The country also has countrywide solar irradiation. The direct normal and global horizontal irradiations are 1,800 kW/m^2/year and 2,000 kW/m^2/year, respectively. With the 2006 national biofuel strategy, 320,000 ha of land were to be planted with Jatropha by 2012 and produce 1.2 million cubic meters of oil [48]. The wind energy capability is mostly concentrated in the Great Coast region (North West) where the wind speed averages around 6 to 7 meters per second. Although this can be deemed relatively low for conventional horizontal-axis wind turbines, it is still of significant magnitude for small- and medium-size vertical-axis wind turbines.

These various sustainable energy solutions can be developed as off-grid stations for local use. They can also be connected to the grid and the power sold to the main distributor.

The current wholesale purchase price by SENELEC is about US₡14 per kWh. Nowadays, the commercialization of renewable energy solutions becomes viable at prices higher than this price. The currently identified wholesale prices for renewable energy projects are as follows. The viable price for biomass solutions is US₡13 per kWh. Solar and wind power solutions have higher rates at US₡24-26 per kWh and US₡17-19 per kWh,

respectively. These prices can be put into perspective by comparing them to the already mentioned price to customers of US₡22 per kWh. Thus, if the cost-effectiveness of the grid-connected project can be argued, it is undeniable that renewables present a great advantage for local consumption. Furthermore, economic incentives can still make the grid-connected stations attractive.

6.4 Public Policies

Although no feed-in tariff has been set for renewable energy solutions, the authorities have imposed that the share of renewable energy be progressively increase. Decree 2011-2013 has given the legal framework for the power purchase from renewable energy plants and stations and their connection to the grid. The frame for determining the feed-in tariffs is also provided therein. Decree 2011-2014 set the conditions of purchasing renewable-energy based power from self-producers (i.e., households or companies producing power for their own consumption) as well as their connection to the grid.

Alongside the legal framework put into place to facilitate the development of sustainable energy solutions, economic incentives have also been put forward. For instance, a tax rebate of up to 35% against the capital cost is offered for solar heating and other renewable energy equipment. Some import tax exemptions are granted for renewable energy equipment. Low rates of added-value taxes (VAT) are granted for local productions, and investors benefit from fiscal exemptions. Furthermore, biofuel farms are exempted from income taxes for five years. Similar incentives are being worked out for other renewable energy sources for rural development, and all renewable energy installations can claim carbon tax credits. The carbon credit was established to reduce CO_2 emissions. This policy, along with other initiatives, is projected to help reduce emissions by an average annual rate of 196,560 tonnes of CO_2 [157].

6.5 Economic Analysis

The economic analysis consists of two parts. There is the breakdown of the cost of the turbine on the one hand and the economic viability analysis on the other hand. Both components of the analysis depend on the local context. In fact, these are respectively connected to the production costs and the wind potential of the region.

The Senegalese Great Coast region was selected for the present analysis. Thus, the analysis that follows will reflect the local context.

6.5.1 Wind Energy Characteristics

The potential of the Great Coast is analyzed by Youm et al. [215] and Ould Bilal et al. [129]. Wind velocities at different sites were recorded over a one-year period. The data acquisition sensors recorded the average, maximum, and minimum values every 10 minutes. Because of the high coverage rates, the data were deemed reliable enough to construct a wind profile for each site. Weibull distributions were thus built for each site. The Weibull distribution follows the equation below.

$$f(v) = \frac{k}{A}\left(\frac{v}{A}\right)^{k-1} e^{-\left(\frac{v}{A}\right)^{k}} \tag{85}$$

Table 6.3: Great Coast Wind Data

Locality	Height [m]	Coverage Rate [%]	Weibull Characteristics	
			A [m/s]	k [-]
Kayar	20	100	4.85	2.77
Potou	20	100	5.37	3.01
Gondon	20	99	4.85	3.02
Sakhor	12	95	5.07	2.29
Sine Moussa Abdou	12	94	5.04	2.37
Botla	12	86	4.70	2.22
Dara Andel	12	82	4.65	2.47
Nguebeul	12	96	4.91	2.77

A summary of the wind acquisition and Weibull characteristics is given in Table 6.3, and the site-specific Weibull distributions are given in Figure 6.5.

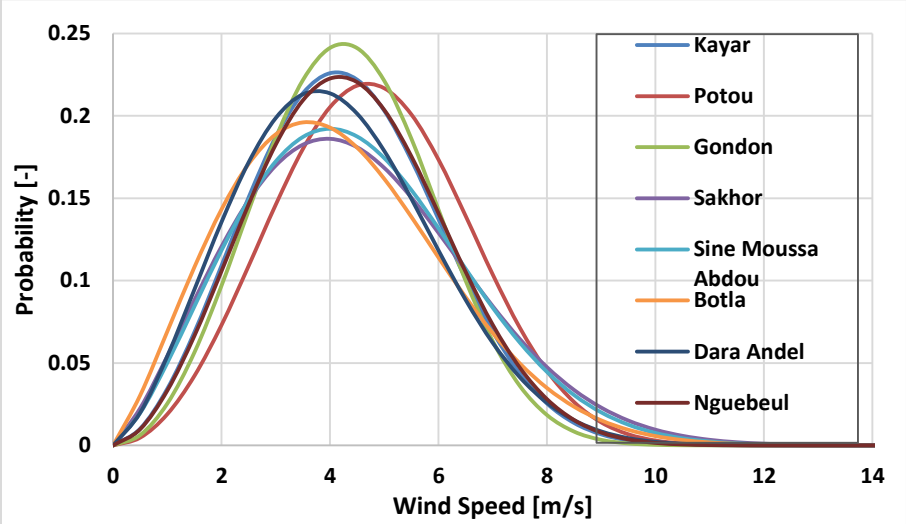

Figure 6.5: Site-Specific Weibull Distributions

The different sites being located within 1.7° latitude and 0.7° longitude, the construction of an average profile for the region is thus pertinent.

The coverage rate is taken as the weight for constructing one meaningful Weibull profile for the region. The result yields the mean Weibull parameters: **A=4.95 m/s** and **k=2.633.**

The corresponding distribution is overplayed in Figure 6.6.

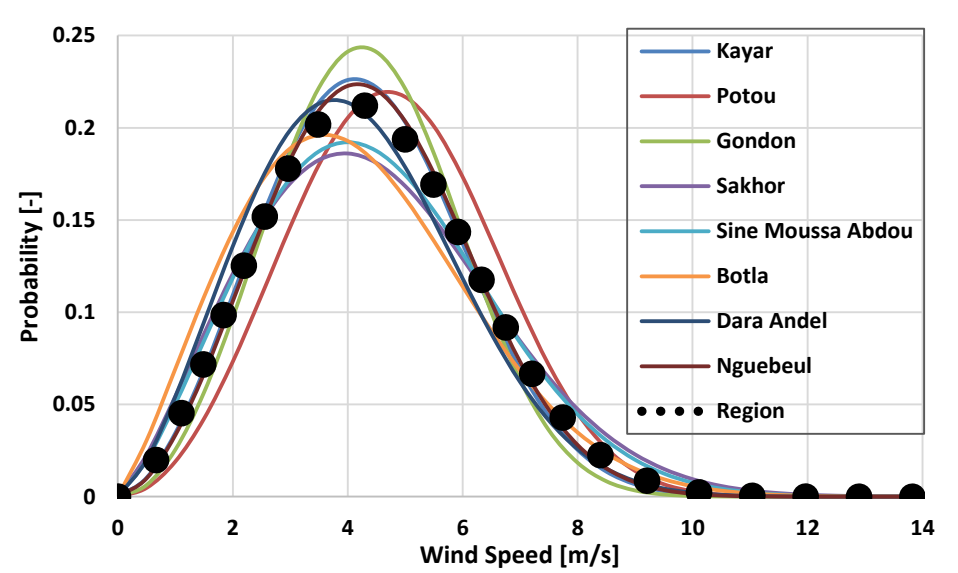

Figure 6.6: Site-Specific and Average Weibull Distributions

These energy probability parameters are complemented by the soiling losses. A soiling loss factor of 2% is retained for SB-VAWTs. No array loss is retained for a single operating turbine. The average coverage rate of 94% obtained by averaging the coverage rates in Table 6.3 is taken as the availability factor. The design parameters for the turbines are grouped in Table 6.4.

Table 6.4: Turbines Design Parameters

	Turbine 1 (Single-Element)	**Turbine 2 (Dual-Element)**
Rated Power (P_R)	10 kW	12 kW
Rotor Diameter (D)	6 m	6 m
Hub Height (Hb)	5 m	5 m
Rotor Height (H)	5 m	5 m
Optimum Cp	0.29	0.35
Averaged Cp	0.18	0.3
Cut-in Wind Speed	3 m/s	2 m/s
Normal Operation Wind Range	3 – 30 m/s	3 – 30 m/s
Cut-out Wind Speed	50 m/s	50 m/s

The rated wind V_R speed is determined following the expression below.

$$V_R = \left(\frac{2.P_R}{\rho.H.D.C_p.\eta}\right)^{1/3} \quad (86)$$

In this expression η denotes the total efficiency after accounting for all the losses.

The intended simplicity and rugged design of the present turbine excluded the use of very sophisticated techniques. Thus, techniques such as the active pitch control mechanisms were dropped. As a direct consequence, a turbine won't achieve its maximum power coefficient all the time. It is instead subject to the changing of the wind conditions.

A variable speed turbine is intended to circumvent this issue. Thus, the turbine operation that results in the achievement of the maximum power coefficient (or near to it) is termed optimal-TSR operation. The non-optimal-TSR operation term is introduced to the represent other operations.

The Weibull-averaged power coefficients ($C_{P,\,WA}$) represents the average non-optimal-TSR operation and define them as:

$$C_{P,WA} = \frac{\sum_{Vmin}^{Vmax}(Weibull\ C_P)}{\sum_{Vmin}^{Vmax}(Weibull)} \quad (86)$$

This is approximated by the average Cp in the given range of tip speed ratios. In the present case, the interval [2, 5] of tip speed ratios is considered.

We refer as rated-speed and second-rated-speed the rated speeds calculated based on the maximum C_P and averaged C_P, respectively. These rated wind speeds are presented in Table 6.5. The rated-speed and second-rated-speed are introduced to evaluate the performance of the variable speed turbines during optimal- and non-optimal-TSR operations, respectively.

Table 6.5: Rated Wind Speeds

	Turbine 1 (Single-Element)	**Turbine 2 (Dual-Element)**
Rated-Speed [m/s]	12.6	12.6
Second-Rated-Speed [m/s]	14.8	13.3

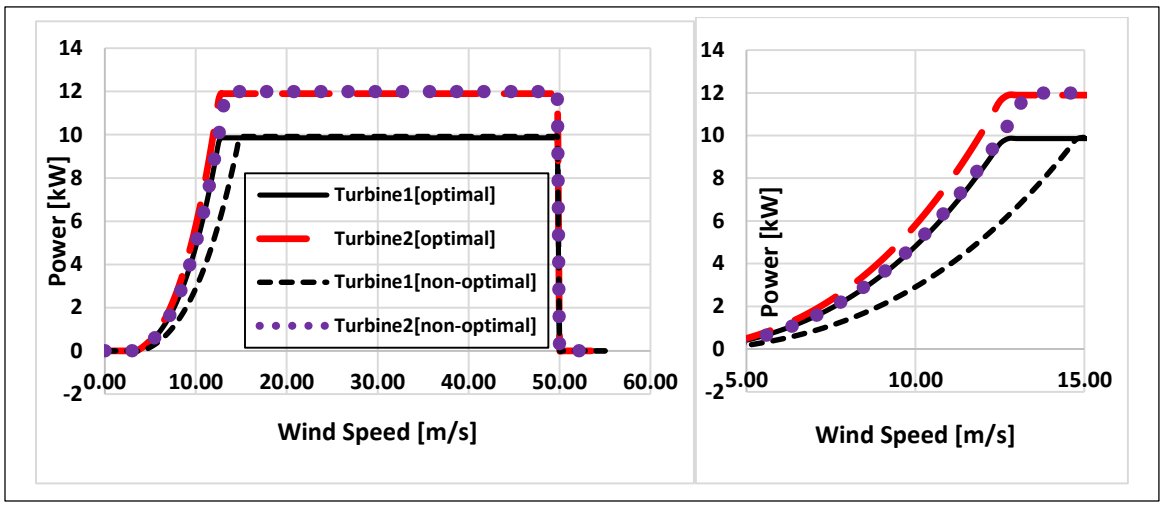

Figure 6.7: Optimal and non-Optimal Turbine Power Curves

The optimal and non-optimal power curves are presented in Figure 6.7 as a function of the wind speed. Although the normal range for the operation wind speed is 3 m/s to 30 m/s, the cut-out wind speed is extended much higher at 50 m/s. This is made possible by the elimination of the gearing and the utilization of the PMAC. Such high cut-out values are all common for small VAWTs. It is noticeable from the power curve that the non-optimal operation of turbine 2 (with dual-element blades) gives a power progression close to its optimal-TSR operation. On the other hand, turbine 1 (with single-element blades) gives a clearer contrast between the optimal- and non-optimal-TSR operations. This is a result of the higher power coefficients obtained with the dual-elements in a wide range of tip speed ratios.

The annual energy production (AEP) and overall Weibull power coefficient (OWCp) are calculated as follows.

$$AEP = \sum_{Cut-in}^{Cut-out} TurbinePower * (1 - soilingLosses) \frac{8760 * availability}{4000} \quad (88)$$

$$OWCp = \sum_{Cut-in}^{Cut-out} C_{P,Weibull} * \frac{8760}{4000} \quad (89)$$

The energy capture ratio (ECR) is then determined using the AEP and OWCp.

$$ECR = \frac{AEP}{OWCp} \tag{90}$$

The energy results are summarized in Table 6.6.

Table 6. 6: Energy Characteristics for Turbines 1 and 2

	Turbine 1 (Single-Element)	**Turbine 2 (Dual-Element)**
Energy Capture [MWh/year]	6.07	7.33
Energy Capture Ratio [-]	73.65	73.65

The aforementioned results are computed using a generic generator efficiency profile. This efficiency being specific to the hardware of generator, a correction factor will be added once the generator hardware characteristics are known.

6.5.2 Cost Evaluation

The overall cost of the turbine depends on the materials used and the manufacturing and installation costs. The cost of ownership also needs to be taken into account in the analysis. Guillaume et al. [66] gave a cost model for small utility SB-VAWTs. They identified four general factors contributing to the cost.

1. The quantity and quality of the materials and the manufacturing (blades, struts, tower),
2. The aerodynamic and centrifugal loads: the RPM and blade chord are used in this component of the model,
3. The characteristics of the electrical system utilizing the torque or power for the model, and
4. The fixed cost related to the installation.

These authors devised a cost formula based on these factors.

$$cost = 500\, N_b cH + 0.3 N_b cHR\omega^2 + 25 C_\tau + constant \tag{91}$$

The fixed component in this formula is in fact proper to the installation.

This formula was checked against the cost breakdown provided by Tota-Maharaj et al. [189] for a larger SB-VAWT. It showed that this cost model is not applicable to larger SB-VAWTs. The turbine investigated by Tota-Maharaj et al. has characteristics (see Table 6.7) close to our reference turbine. Thus, the cost breakdown for the present turbine can borrow certain of its aspects. But the absolute reference will remain the 12 kW turbine described in the previous sections.

Table 6.7: Turbine Characteristics (Source: Tota-Maharaj et al. 2012)

Diameter	6.096 [m]
Blade Profile	NACA 0018
Chord Length	0.55 [m]
Blade Length	3.048 [m]

The prices will be set based on the component specifications and the market prices of hardware of similar characteristics.

In the case of the turbine under investigation, the key elements are the blades, the struts and tower, a permanent magnet synchronous generator, and a system of rectifier-inverters for variable speed operation and grid connection. The cost will also take the foundation into account. The characteristics of the different components are detailed here. The foundation is to be made in concrete. Steel is used for the supporting structure and the tower of the turbine. Fiberglass is utilized for the blades and the struts. Aluminum could be used, but fiberglass is lighter and has a better resistance to fatigue and other structural characteristics. Thus, this composite material is selected for long-term reliability and cost effectiveness. A permanent magnet (AC) is preferred to the induction motor and servomotor because of better efficiency. It also runs cooler under similar load conditions. The low operating temperatures not only reduce the thermal fatigue, but also make it more adapted to hot environments, as is the case for the selected site of operation. In terms of power density, the Rare-Earth permanent magnets produce more flux compared to similar size induction devices. Finally, because of the high efficiency, the full return on the initial

cost of purchase is realized after a shorter period of time. The last set of components consists of the inverter-rectifier and other electrical hardware. A passive-diode inverter is selected for its reliability since it requires no control system.

Average prices of the aforementioned components with specifications that meet the project need were looked up. Either the market price is considered or the overall cost of components and labor if the production and/or assembly can be made locally at a lower price. The costs are detailed as follows:

- **Foundation**

  The cost was estimated based on the local cost of cement, sand, gravel, iron, and labor.

- **Blades**

  The dual-element is given a factor 1.2 compared to the single-element. This choice is justified by the fact that less material will be used by the dual-element but the manufacturing process is more elaborate.

- **Deep Cycle Batteries**

  Low cost DC12-200 (12 Volts, 200 Amp-Hours) series were adopted for the present project. The market provides for this series a unit price of US$10-50. With a conservative price of US$30 per unit, a set of 10 batteries can be acquired.

- **Generator**

  The price of the PMAC is constructed based on the cost breakdown for a 10 kW generator provided by Warlock Engineering[1]. The provided total cost is AU$875 (i.e., ~US$750). A conservative price of US$1,000 is retained in the present analysis for a 10 kW generator. The 12 kW generator is estimated at US$1,200.

---

[1] Warlock Engineering: 10 kW, 15ϕ Axial flux pancake generator for 2-blade Wind Turbine

- **Replacement Cost and Maintenance**

2% of the total cost of the components is added for this item.

- **Warranty**

It was estimated that an additional 5% of the value of the turbine could be paid for the insurance.

- **Transportation and Logistics**

This includes the assembly and installation. Because of the relatively small size of the turbine, it was estimated that this cost should not go beyond 5% of the turbine value as well.

- **Capital Cost**

A capital of 8% over five years was added to the cost breakdown. This rate may be high but is common for underdeveloped countries. For the purpose of this analysis the BCEAO mortgage rates are taken as reference. The 2013 rate was established at 7.44% [218]. The value of 8% is maintained for the present analysis.

The different contributors to the cost are detailed in Table 6.8.

Table 6.8: Cost Breakdown (in US $) for the Studied Turbines

	Single-Element	Dual-Element
Foundation	125	125
PMAC	1000	1200
Supporting Structure	50	50
Struts	200	250
Blades(3)	3x250	3x300
Electrical System	200	200
Deep Cycle Batteries	300	300
Sub-Total 1 (SB1)	**2825**	**3025**
Replacement Cost and Maintenance	2% SB1 = 55	60
Warranty	132	152
Transportation and Logistics	132	152
SB 2	**2944**	**3389**
Capital Cost	1178	1355
TOTAL	**4122**	**4744**

Not added to the cost are:

- **The Land Lease**

  The portion of land to be occupied by the turbine is relatively small. It is perceived that the operator of the turbine will own the land. Otherwise, the local authorities will grant a concession as part of the incentives for developing renewable energy solutions.

- **Roads and Civil Work**

  The turbine is small enough to be transported through existing infrastructures.

- **Engineering Permits**

  Small projects of this size are generally handled at the local level and the permits are generally granted at little or no cost.

- **Grid Connection**

  For the time being, this option was not retained because there are no clear-cut grid feed-in prices. Investing on a grid connection apparatus may be somewhat risky. In addition, given the rate of electrification and the energy need, the power produced can be consumed locally for local electrification and/or small rural projects.

The cost of energy is calculated over the five-year period of the loan. The cost of energy (CoE) over this period is calculated as follows:

$$CoE = \frac{Total\ Cost}{AEP.\ (Number\ of\ Years)} \tag{92}$$

The cost of energy of optimal-TSR operations is summarized in Table 6.9 for the two turbines.

Table 6.9: CoE for Optimal-TSR Operation

	Turbine 1 (Single-Element)	**Turbine 2 (Dual-Element)**
AEP [MWh/year]	6.07	7.33
CoE [US ₵/KWh]	13.6	12.9

These prices show a slight improvement as a result of the dual-element configuration. However, the difference is clearly more striking for the average non-optimal-TSR operations, as shown in Table 6.10. The annual energy production during non-optimal-TSR operations is almost doubled as a result of the change of blade configuration. This is similarly reflected in the prices over the initial five-year period.

Table 6.10: Average non-Optimal Operation: AEP and CoE

	Turbine 1 (Single-Element)	**Turbine 2 (Dual-Element)**
AEP [MWh/year]	3.31	6.06
CoE [US ₵/KWh]	24.9	15.6

As mentioned earlier, the rugged design excludes the use of sophisticated techniques to make the turbine operate with its optimal performance. Thus, it is opted for the construction of a hybrid price by assuming that a turbine will operate about 60% of the time near its optimal operating conditions. The remaining 40% is approximated by the averaged non-optimal values discussed earlier. The result is given in Table 6.11 and compared with other market prices.

Table 6.11: Comparison of Electricity Prices

	CoE [US ₵/KWh]
Turbine 1 (Single-Element)	18.12 = **0.6x13.6+0.4x24.9**
Turbine 2 (Dual-Element)	14.00 = **0.6x12.9+0.4x15.6**
Wholesale Price to SENELEC	14
SENELEC Price to Customer	22
Biomass Viability Price	13
Solar Viability Price	24-26
Wind (HAWT) Viability Price	17-19

The comparison shown in Table 6.11 indicates that the present VAWT (design and cost analysis) yields a price below or equal to all the market sectors except for the biomass. Compared to the existing HAWT solutions, the price difference can be attributed to the design complexity of the HAWTs, the control systems, and other infrastructure and logistics costs. For that matter, even the conventional VAWT (turbine 1) yields a price

comparable to that of the HAWTs. This analysis corroborates the earlier discussion (see Chapter 1) on the advantages and disadvantages of the HAWT and VAWT technologies. In sum, not just the raw power coefficient must be considered. Rather, a careful analysis needs to be conducted on a case-by-case basis to determine which energy solution is most appropriate for a given locality.

The present economic analysis is aimed at establishing the economic viability of not only the dual-element configuration but also the vertical-axis wind turbine in general. The case was conclusive for the designated site in the Senegalese Great Coast region. We also emphasized the need of underdeveloped regions to make good use of the available energy sources. This is indeed one of the main drivers of economic development.

Conclusions can be drawn from the work presented so far and suggestions can be made for future studies.

CHAPTER 7

CONCLUSIONS AND RECOMMENDATIONS

The present work aimed at studying the keys features of straight-bladed vertical-axis wind turbines (SB-VAWTs) and proposing performance enhancement techniques. Emphasis was given to the use of multi-element blades. In order to do this, existing and specially conceived tools were utilized.

Before presenting his research, the author conducted a thorough literature survey of prior works in the areas pertaining to the different aspects of his research. The investigations themselves utilized computational fluid dynamics (CFD) and semi-analytical calculations. ANSYS Fluent® was used for the CFD. A code was developed for the double multiple streamtube (DMST) model. Existing dynamic stall models (e.g., Gormont empirical model) as well as a customized model (modified Sheng model) were utilized in conjunction with the DMST. The theoretical formulation of these approaches and models were detailed in this dissertation. The different tools were then validated against existing open-field and numerical data. Preliminary analyses were conducted to support the present approach and pave the way to the main investigations.

A detailed study of the single-element SB-VAWT was conducted using CFD and DMST. In addition to expounding on the physics of the device, this study had the goal of establishing the DMST as a plausible substitute to the CFD for the preliminary design phase. The Uppsala 12 kW turbine was utilized as a reference. The DMST calculations were conducted first with a static stall setting. The calculations were repeated with dynamic stall using the Gormont empirical model and the modified Sheng model. The dynamic stall of the blades and the aerodynamic performance of the rotor obtained with the different approaches and models were compared. Flow-field analyses were used to explain some of

the most remarkable features. The results were conclusive in regard to the aforementioned goal.

The investigation of the dual-element-blade rotor first focused on detailing the desirable characteristics for the blade. A parametric analysis was then conducted to identify a suitable candidate for the specified application. Calculations of the performance were then performed and the results explained in light of the flow dynamics.

Finally, a cost analysis was conducted to establish the economic viability for the rotor. For this purpose, a site was selected in the Senegalese Great Coast region. A comprehensive picture was given with a description of the local situation, the energy need, the current sources and prices, and public policy issues. The current share of renewable energies in general and wind energy in particular and their potential were also elaborated on. A detailed description of the wind energy characteristics of the region was presented. This was followed by a cost breakdown to determine the potential cost of energy and establish the economic viability.

7.1 Conclusions

Based on the studies performed, the following conclusions can be drawn:

1. The preeminence of the dynamic stall phenomenon was underlined throughout this work. It is of utmost importance to properly model it. A given model should be fine-tuned to fit the conditions of the problem under investigation.
2. As discussed in this work, it was necessary to modify the Sheng dynamic stall model to account for the specific conditions of vertical-axis wind turbine operations. The present formulation was shown to give a better approximation of the CFD results.

3. The DMST model was validated as a means to capture the overall performance of the rotor. Therefore, it is recommended to make use of it as a substitute for the CFD during the preliminary design phase.
4. The findings showed the dual-element blade configuration to be a means for performance enhancement. It is recommended that a proper set of parameters be determined for each design. The enhancements that resulted from the utilization of dual-element blades includes a high power coefficient for all tip speed ratios. The operating range was also broadened. The stability of operation near the optimum TSR was improved. The averaged non-optimal-TSR operation also gave relatively high power output.
5. The economic analysis established the viability of the dual-element turbine. The dual-element solution was found to give prices below, or in the range of, the current market prices. The cost of energy for the VAWTs showed that this technology is of benefit for small energy consumption markets and regions of relatively low wind speeds. This is a result of a less complex technology and fewer costly expenditure.

7.2 Recommendations for Future Work

Based on the investigations and conclusions thereof, the following recommendations can be made for future research:

1. Although the performance predictions by the DMST model are relatively accurate, there is room for improvement. In the present formulation, the upstream and downstream actuator disks are always facing each other, while there is not necessarily a blade at the place of the downstream actuator disk. The calculation of the induction factors uses only the total number of blades. The number of blades should be accounted for in the periodicity of the transcendental function as well so as to represent the phase lag between the blades. Additionally, it was noticed that

the DMST experiences low TSR convergence defect with the use of fixed-point iteration. It is thus recommended that future works use higher order iteration methods such as the Newton methods.

2. The modified Sheng model is currently designed for single-element blades. It is recommended that future studies be dedicated to adapting it to multi-element blades. These studies should then include more exhaustive investigations of the blade/flow interactions between the different elements. Since the studies of blade in tandem are available in the literature, these should be used as a stepping stone.
3. For further performance enhancement, the present technique (dual-element blades) can be associated with other approaches such as twisted blades. This "hybrid" will then use twisted-dual-element blades. However, the manufacturing of such blades will be more costly. It will then be necessary to see whether the performance improvement is worth the added cost.
4. In the course of the parametric studies, some configurations were found to have overall great characteristics. But this was not followed by good performance output. In this regard, the author suggests that a large lift-to-drag ratio at certain angles of attack is not necessarily synonymous with good performance. The author postulates that there is a trade-off between great aerodynamic characteristics and the amount of energy the rotor can harvest under given conditions. Thus, when the system has blades that give it the hypothetic potential to operate beyond the limit, it falls back under more stable conditions. Such conditions may not necessarily yield performance enhancement. The author postulates in this regard that the thickness of the blade needs to be accounted for during the parametric study.

   The pitch of the equivalent dual-element blade should also be introduced as a variable in the parametric study.
5. Finally, in connection with the thickness, the blade elements can be designed to allow a more streamed flow and to optimize the interaction in the region of the gap.

APPENDIX A. CHANNEL BLOCKAGE

Nomenclature

A : rotor frontal section

A_1 : channel cross-section area

A_w : wake cross-section area

F_{rotor} : aerodynamic force on the turbine

P : aerodynamic power delivered by the rotor

P_1 : upstream pressure

P_2 : downstream pressure

v : velocity through the turbine

v_1 : upstream velocity

v_2 : downstream velocity outside the wake

v_w : downstream velocity inside the wake

V_2 : v_2/v_1

V_w : v_w/v_1

α : A/A_1

β : A_w/A

ρ : density

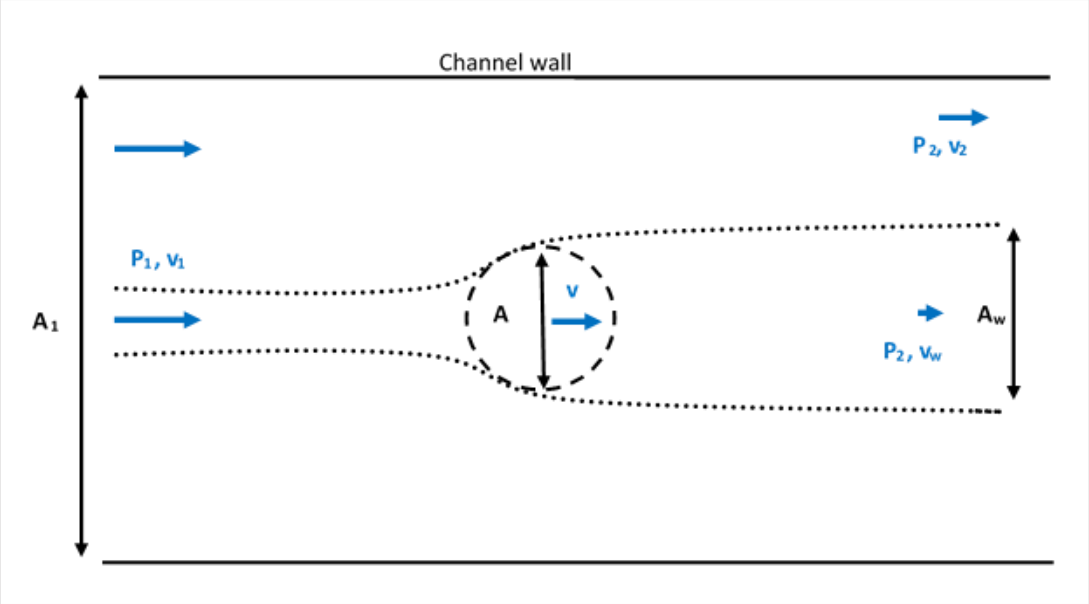

Figure A.1: Sketch of a Turbine in a Channel

Derivation

The flow is considered incompressible. Applying the continuity equation to flow in the entire channel and to the streamtube of the flow through the rotor, we obtain the respective equations:

$$(A_1 - A_w)v_2 + A_w v_w = A_1 v_1 \tag{1}$$

$$Av = A_w v_w \tag{2}$$

Similarly, the momentum equation in the same domains give:

$$F_{rotor} = A[(P_1 - P_2) + {}^1/_2\,\rho(v_1^2 - v_w^2)] \tag{3}$$

$$F_{rotor} = A_1(P_1 - P_2) + \rho A_1 v_1^2 - \rho A_w A_w^2 - \rho(A_1 - A_w)v_2^2 \tag{4}$$

Then, the Bernoulli equation is applied on a streamline that is not affected by the rotor and gives:

$$P_1 + {}^1/_2\,\rho v_1^2 = P_2 + {}^1/_2\,\rho v_2^2 \tag{5}$$

Equations (2), (3), and (5) give, respectively:

$$v = \frac{A_w}{A} v_w = \beta v_w \tag{6}$$

$$F_{rotor} = {}^{1}/_{2}\, \rho A (v_2^2 - v_w^2) \tag{7}$$

$$P_1 - P_2 = {}^{1}/_{2}\, \rho (v_2^2 - v_1^2) \tag{8}$$

Using equations (6) and (7), the power delivered by the rotor can be written as:

$$\boldsymbol{P} = F_{rotor} v = F_{rotor} \frac{A_w}{A} v_w = {}^{1}/_{2}\, \rho A_w v (v_2^2 - v_w^2) \tag{9}$$

and the power coefficient becomes:

$$C_p = \frac{P}{{}^{1}/_{2}\, \rho A v_1^3} = \frac{A_w}{A} \left(\frac{v_2^2 - v_w^2}{v_1^2} \right) \frac{v_w}{v_1} = \beta (V_1^2 - V_w^2) V_w^2 \tag{10}$$

Divided by A_1v_1, equation (1) becomes:

$$(1 - \alpha\beta) V_2 + \alpha\beta = 1 \tag{11}$$

Combining equations (4), (7), and (8), we obtain:

$$(1 + \alpha - 2\beta) V_2^2 + \alpha (2\beta - 1) V_w^2 = 1 \tag{12}$$

Equations (10), (11), and (12) constitute the governing equation for determining the blockage to the performance of the turbine. For given values of α and V_w, equations (11) and (12) are solved for β and V_2. As can be seen with the Betz limit derivation, $V_w = {}^{1}/_{3}$ gives the optimum result.

APPENDIX B. BETZ LIMIT

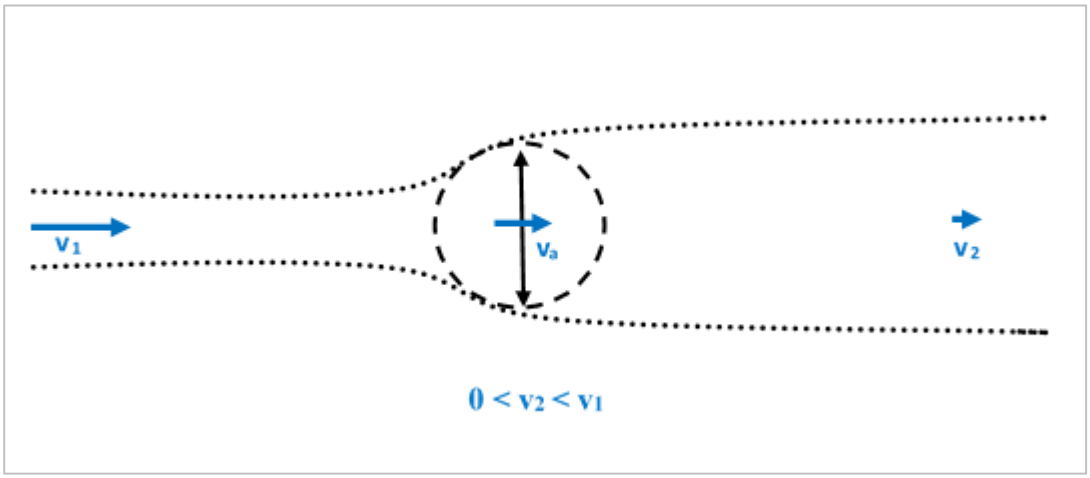

Figure Ap. 2: Sketch of Betz Limit Formulation

Nomenclature

A : disk area

Cp : Power coefficient

K : Wind Kinetic Energy

P : Aerodynamic Power delivered by the turbine

V1 : upstream far-field velocity

V2 : downstream far-field velocity

Va : average velocity in the turbine

$\dot{m}$: Mass flow rate

ρ : air density

Derivation

First, it is worth mentioning that the Betz theoretical formulation does not take into account the non-ideal effects. This theoretical limit is based on the fact that there must be air still flowing through the turbine for it to operate.

The power transferred from the wind to the turbine can be given as:

$$P = \frac{d}{dt}(K) = {}^{1}/_{2}\,\dot{m}(v_1^2 - v_2^2) \text{ where } \dot{m} = \rho A v_a = \rho A \frac{(v_1 + v_2)}{2} \quad (1)$$

The average velocity through the turbine is taken to be the average between the upstream and downstream velocities. The equation for the power is re-arranged in the form:

$$P = {}^{1}/_{2}\,\rho A v_1^3 \left[1 + \left(\frac{v_2}{v_1}\right) - \left(\frac{v_2}{v_1}\right)^2 - \left(\frac{v_2}{v_1}\right)^3\right] \quad (2)$$

The ideal power is obtained for ${}^{v_2}/_{v_1} = {}^{1}/_{3}$, which yields $P_{ideal} = {}^{1}/_{2}\,\rho A v_1^3 \langle\frac{16}{27}\rangle$

Thus, the ideal power coefficient referred to as the Betz Theoretical Limit is:

$$C_p = \frac{P}{{}^{1}/_{2}\,\rho A v_1^3} = {}^{16}/_{27} \sim 0.5926 \quad (3)$$

REFERENCES

[1] ACKERMANN, T., and SODER, L., "Wind energy technology and current status: a review," *Renewable and Sustainable Energy Reviews*, Vol. 4, No. 4, December 2000, pp. 315-374

[2] AfDB., "*The Middle of the Pyramid: Dynamics of the Middle Class in Africa*," African Development Bank Report 2011

[3] AHMAD, K.A., ABDULLAH, M.Z., and WATTERSON, J.K., "Numerical modelling of pitching airfoil," *Jurnal Mekanikal*, June 2010, No. 30, pp. 37-47

[4] AKWA, J. V., VIELMO, H. O., and PETRY, A. P., "A review on the performance of Savonius wind turbines," *Renewable and Sustainable Energy Reviews*, Vol. 16, No 5, June 2012, pp. 3054-3064

[5] ALLET, A., and PARASCHIVOIU, I., "Viscous flow and dynamic stall effects on vertical-axis wind turbines," *International Journal of Rotating Machinery*, Vol. 2, No. 1, pp. 1-14, 1995

[6] ALVIN-PIERCE, J., "*An Experimental Study of Dynamic Stall in an Oscillating Airstream*," Final Report of NASA Research Grant NGR 11-002-185, School of Aerospace Engineering, Georgia Institute of Technology

[7] AMET, E., MAITRE, T., PELLONE, C., and ACHARD, J-L., "2D Numerical simulation of blade-vortex interaction in Darrieus turbine," *Journal of Fluids Engineering*, Vol. 131, No. 11, Nov. 2009

[8] AMIRALAEI, M., "*Computational Fluid Dynamic Simulation of Airfoil in Unsteady Low Reynolds Number Flows*," Ph.D. Dissertation, Ryerson University, Toronto, ON, Canada 2012

[9] ASHWILL, T. D., "*Measured Data for the Sandia 34-Meter Vertical-Axis Wind Turbine*," Sandia Report SAND91-2228, 1992

[10] BAH, E. A. A., SANKAR, L., and JAGODA, J., "Investigations on the use of multi-element airfoils for improving vertical-axis wind turbine performance," *51st AIAA Aerospace Sciences Meeting and Exhibits*, Jan. 7-10, 2013, Grapevine, TX

[11] BAH, E. A. A., SANKAR, L., and JAGODA, J., "Numerical investigations on the use of multi-element airfoils for vertical-axis wind turbine configurations," *Proceedings of the ASME 2013 Gas Turbine India Conference*, Dec. 5-6, 2013, Bangalore, India

[12] BAH, E. A. A., SANKAR, L., and JAGODA, J., "An assessment of computational fluid dynamics and semi-empirical approaches for vertical-axis wind turbine analysis," *Proceedings of the International Conference on Power & Energy Engineering*, Hong Kong, China, August 8-9, 2014

[13] BALAT, A., "A review of modern wind turbine technology," *Energy Sources, Part A: Recovery, Utilization and Environmental Effects*, Vol. 31, issue 17, 2009, pp. 1561-1571

[14] BANGALORE, A and SANKAR, L. N., "Forward flight analysis of slatted rotors using Navier-Stokes methods," *Journal of Aircraft*, Vol. 34, No. 1, January-February 1997, pp. 80-86.

[15] BARTH, T. J., and JESPERSEN, D., "The design and application of upwind schemes in unstructured meshes," Technical Report AIAA-89-0366, AIAA 27th Aerospace Sciences Meeting, Reno, NV 1989

[16] BAZILIAN, M., NUSSBAUME, P., ROGNER, H., B.H. A., FOSTER, B., and PACHAURI, S., "Energy access scenarios to 2030 for the power sector in sub-Saharan Africa," *FEEM Working Paper*, 2011

[17] BENEDICT, M., LAKSHMINARAYAN, V., PINO, J., and CHOPRA, I., "Fundamental understanding of the physics of a small-scale vertical-axis wind turbine with dynamic blade pitching: an experimental and computational approach," *54th AIAA/ASME/ASCE/AHS/ASC Structures, Structural Dynamics and Materials Conference*, April 8-11, 2013, Boston, MA

[18] BENJANIRAT, S., and SANKAR, L., "Evaluation of a two-equation turbulence model for the prediction of wind turbine aerodynamics," *Proceedings of the 22nd Wind Energy Symposium*, Jan. 2003.

[19] BENJANIRAT, S., and SANKAR, L., "Recent improvements to a combined Navier-Stokes full potential methodology for modeling horizontal-axis wind turbines," *AIAA/ASME Wind Energy Symposium*, AIAA Paper 2004-083, Jan. 2004.

[20] BERG, D. E., "An improved double-multiple streamtube model for the darrieus-type vertical-axis wind turbine," *6th Biennial Wind Energy Conference and Workshop*, 1983, pp. 231-233

[21] BERI, H., and YAO, Y., "Double multiple stream tube model and numerical analysis of vertical-axis wind turbine," *Energy and Power Engineering*, 2011, 3, 262-270

[22] BERI, H, and YAO, Y., "Effect of camber airfoil on self-starting of vertical-axis wind turbine," *Journal of Environmental Science and Technology* 4 (3): 302-312, 2011

[23] BJORCK, A., MERT, M., and MADSEN, H. A., "Optimal parameters for the FFA-Beddoes dynamic stall model," *Proceedings of the European Wind Energy Conference*, Nice, France, March 1999

[24] BRAHIMI, M.T., ALLET, A., and PARASCHIVOIU, I., "Aerodynamic analysis models for vertical-axis wind turbine," *International Journal of Rotating Machinery*, Vol. 2, No 1, pp. 15-21, 1995

[25] BROERING, T.M., LIAN, Y., and HENSHAW, W., "Numerical investigation of energy extraction in a tandem flapping wing configuration," *AIAA Journal*, Vol. 50, No. 11, November 2012

[26] BROCHIER, G., FRAUNIE, P., BEGUIER, C., and PARASCHIVOIU, I., "Water channel experiments of dynamic stall on Darrieus wind turbine blades," *Journal of Propulsion and Power*, Vol. 2, 1986, pp. 445-449.

[27] BROERING, T. M., LIAN, Y., HENSHAW, W., "Numerical investigation of energy extraction in a tandem flapping wing configuration," *AIAA Journal*, Vol. 50, No. 11, November 2012

[28] CARR, L. W., "Progress in analysis and prediction of dynamic stall," *Journal of Aircraft*, Vol. 25, No. 1 (1988), pp. 6-17.

[29] CARRIGAN, T-J., "*Aerodynamic Shape Optimization of a Vertical-Axis Wind Turbine*," MS Thesis, University of Texas at Arlington, December 2010

[30] CASTELLI, M. R., De BETTA, S., and BENINI, E., "Effect of blade number on a straight-bladed vertical-axis Darreius wind turbine," *World Academy of Science, Engineering and Technology*, Vol. 6, 2012

[31] CASTILLO, J., "*Small Scale Vertical-Axis Wind Turbine Design*," BS Thesis, Tempere University of Applied Sciences, December 2011

[32] CEBECI, T., BESNARD, E., and CHEN, H-H., "Calculation of multi-element airfoil flows, including flap wells," AIAA 96-0056

[33] CHAITEP, S., CHAICHANA, T., WATANAWANYOO, P., and HIRAHARA, H., "Performance evaluation of curved blades vertical-axis wind turbine," *European Journal of Scientific Research*, Vol. 57, No. 3 (2011) pp. 435-446

[34] CHEN, C.-C., and KUO C.-H., "Simulation on performance of vertical-axis wind turbine," ESDA Paper 2010-24207, *10th Biennial Conference on Engineering Systems Design and Analysis*, July 12-14, 2010, Istanbul, Turkey.

[35] CLAESSENS, M-C., "*The Design and Testing of Airfoils for Application in Small Vertical-Axis Wind Turbines*," MS Thesis, Delft Technical University, November 2006

[36] DAI, J. C., HU, Y. P., LIU, D. S., and LONG, X., "Aerodynamic loads calculation and analysis for large scale wind turbine based on combining BEM modified theory with dynamic stall model," *Renewable Energy*, Vol. 36, No. 3, March 2011, pp. 1095–1104

[37] DABIRI, J. O., "Potential order-of-magnitude enhancement of wind farm power density via counter-rotating vertical-axis wind turbine arrays," *Journal of Renewable and Sustainable Energy*, Vol. 3, No. 4, 2011

[38] DABIRI, J. O., GREER, J. R., KOSEFF, J. R., MOIN, P., and PENG, J., "A new approach to wind energy: opportunities and challenges," *AIP Conference Proceedings*, 2014

[39] D'AMBROSIO, M., and MEDAGLIA, M., "*Vertical-Axis Wind Turbines: History, Technology and Application*," MS Thesis in Energy Engineering, Halmstad University, SWE, 2010

[40] DARRIEUS, G. J. M., "*Turbine Having its Rotating Shaft Transverse to the Flow of the Current*," US Patent 1,835,018, December 1931

[41] DEGLAIRE, P., ENGBLOM, S., AGREN, O., and BERHOFF, H., "Analytical solutions for a single in vertical-axis wind motion in two-dimensions," *European Journal of Mechanics B/Fluids* 28 (2009) 506-520

[42] DEGLAIRE, P., ERIKSSON, S., KJELLIN, J., and BERNHOFF, H., "Experimental results from a 12 kW vertical-axis wind turbine with a direct driven PM synchronous generator," *European Wind Energy Conference & Exhibition*, Milan, Italy, 2007

[43] DEGLAIRE, P., "*Analytical Aerodynamic Simulation Tools for Vertical-Axis Wind Turbines*," PhD. Dissertation, Uppsala University, 2010

[44] D.O.E., "*20% wind energy by 2030. Increasing Wind Energy Contribution to U.S. Electricity Supply*," Department of the Energy, 2008

[45] DYACHUK, E., GOUDE, A., and BERNHOFF, H., "Dynamic stall modeling for the conditions of vertical-axis wind turbines," *AIAA Journal* Vol. 52, No. 1 January 2014

[46] EBERHARD, A., FOSTER, V., CECILIA, B.G., OUEDRAOGO, F., CAMOS, D., and SHKARATAN, M., "*Underpowered: The State of the Power Sector in Sub-Saharan Africa*," Washington, DC: The World Bank, 2008

[47] EBOIBI, O., "*The Influence of Blade Chord on the Aerodynamics and Performance of Vertical-Axis Wind Turbines*," PhD. Dissertation, The University of Sheffield, October 2013

[48] EID. A-M., ABDEL-SALAM, M., and ABDEL-RAHMAN M-T., "Vertical-axis wind turbine modeling and performance with axial-flux permanent magnet synchronous generator for battery charging applications," *The 11th International Middle East Power Systems Conference*, 2006

[49] EKATERINARIS, J. A., and PLATZER, M. F., "Computational prediction of airfoil dynamic stall," *Progress in Aerospace Sciences*, Vol. 33, pp. 759-846, 1997

[50] ENDA: *Energy, Environment, Development Program*, "Biofuels in Senegal: Jatropha Program 2007-2012", Senegal Ministry of Agriculture, March 2007

[51] EPPLER, R., "Turbulent airfoils for general aviation," *Journal of Aircraft*, Vol. 15, No. 2, pp. 93-99, February 1978

[52] ERICKSON, D-W., WALLACE, J-J and PERAIRE, J., "Performance characterization of cyclic blade pitch variation on a vertical-axis wind turbine," *49th AIAA Aerospace Sciences Meeting including the New Horizons Forum and Aerospace Exposition*, 4-7 January 2011, Orlando, FL.

[53] ERIKSSON, S., BERNHOFF, H., and LEIJON, M., "Evaluation of different turbine concepts for wind power," *Renewable and Sustainable Energy Reviews*, Vol. 12, issue 5, 2008, pp.1415-1234

[54] FANUCCI, J. B., and WALTERS, R.E., "*Innovative Wind Machines: The Theoretical Performance of Vertical-Axis Wind Turbine Technology Workshop*," Sandia Laboratories SAND765586, 1976

[55] FAVIER, D., AGNES, A., BARBI, C., and MARESCA, C., "Combined translation/pitch motion: a new airfoil dynamic stall simulation," *Journal of Aircraft*, Vol. 25, No. 9, September 1988

[56] FIEDLER, A-J., and TULLIS, S., "Blade offset and pitch effects on a high solidity vertical-axis wind turbine," *Wind Engineering* Vo.33, No.3, 2009 pp 237-246

[57] FORTUNATO, B., CAMPOREALE, S.M., TORRESI, M., DE FAZIO, D., and GIORDANI, M., "Experimental results of a vertical-axis wind turbine," *Proceedings of the ASME 2010 Biennial Conference on Engineering Systems Design and Analysis ESDA2010*, July 12-14, 2010, Istanbul, Turkey

[58] FRERIS, L., INFIELD, D., "Renewable Energy in Power Systems," *John Wiley and Sons, Ltd* 2008

[59] GAZZANO, R., MARINI, M., and SATTA, A., "Performance calculation for a vertical-axis wind turbine with variable blade pitch," *International Journal of Heat and Technology*, Vol. 28, No. 2, 2010

[60] GEURTS, B., SIMAO-FERREIRA, C-J., and van BUSSEL, G., "Aerodynamic analysis of a vertical-axis wind turbine in a diffuser," *Proceedings of the 3rd EWEA Conference – Torque 2010: The Science of Making Torque from Wind*, Heraklion, Crete, Greece, June 28-30, 2010

[61] GLAZ, B., LIU, L., FRIEDMAN, P. P., BAIN, J., and SANKAR, L. N., "A surrogate-based approach to reduced-order dynamic stall modeling," *Journal of the American Helicopter Society*, Vol. 57, 022002, 2012

[62] GLAZ, B., FRIEDMAN, P. P., CAJIGAS., J. G., BAIN, J., and SANKAR, L. N., "Reduced-order dynamic stall modeling with swept flow effects using a surrogate-based recurrence framework," *AIAA Journal*, Vol. 51, No. 4, April 2013

[63] GORMONT, R. E., "*An Analytical Model of Unsteady Aerodynamics and Radial Flow for Application to Helicopter Rotors*," U.S. Army Air Mobility Research and Development Laboratory Technical Report 72-67, 1973

[64] GOUDE, A., "*Fluid Mechanics of Vertical-Axis Turbines: Simulation and Model Development*," PhD. Dissertation, Uppsala University, 2012

[65] GTZ "*Regional Reports on Renewable Energy 30 Country Analysis on Potentials and Markets in: West Africa (17), East Africa (5) Central Asia (8),"*Eschborn: GTZ 2009

[66] GUILLAUME, C., ALGAZZE, S., and DUC, E., "Economic feasibility of wind turbines for individual households," *European Wind Energy Conference* EWEC 2009

[67] HANSEN, A. C., and BUTTERFIELD, C. P., "Aerodynamics of horizontal-axis wind turbines," *Annual Review of Fluid Mechanics*, Vol. 25: 115-149, January 1993

[68] HEALY, J-V., "The Influence of blade camber in the output of vertical-axis wind turbines," *Wind Engineering* Vol.2, No.3 1978

[69] HEALY, J-V., "The influence of blade thickness on the output of vertical-axis wind turbines," *Wind Engineering*, Vol.2 No.1 1978

[70] HEIER, S., "Grid Integration of Wind Energy Conversion System", *Wiley* 1996

[71] HIRSCH H., and MANDAL, A. C., "A cascade theory for the aerodynamic performance of Darrieus wind turbines," *Wind Engineering*, Vol. 11, No. 3, pp 164-175, 1987

[72] HOLIERHOEK, J. G., de VAAL, J. B., van ZUIJLEN, A. H., and BIJL, H., "Comparing different dynamic stall models," *Wind Energy*, Vol. 16, No. 1, 2013, pp. 139–158

[73] HOLME, O., "A contribution to the aerodynamic theory of vertical-axis wind turbines," *International Symposium of Wind Energy Systems*, Cambridge, England, 1976

[74] HOMICZ, G. F., "*Numerical Simulation of VAWT Stochastic Aerodynamic Loads Produced by Atmospheric Turbulence: VAWT-SAL Code*," Sandia Laboratories SAND91-1124, 1991

[75] HOWELL, R., QIN, N., EDWARDS, J., and DURRANT, N., "Wind tunnel and numerical study of a small vertical-axis wind turbine," *Renewable Energy*, 35 (2010) pp. 412-422

[76] HSIEH, W. C., MIAO, J. M., LAI, C. C., and TAI, C. S., "Wind tunnel analysis on performance of H-rotor, VAWTs with NACA 64xx Blades," *Advanced Materials Research*, Vols. 488-489 (2012) pp. 1213-1218

[77] IIDA, A., MIZUMO, A., and FUKUDOME, K., "Numerical simulation of aerodynamic noise radiated from vertical-axis wind turbines," *Proceedings of the 18th International Congress on Acoustics*, 2004

[78] IRENA (International Renewable Energy Agency), "*Senegal: Renewables Readiness Assessment*," 2012

[79] ISLAM, M., TING, D. S.-K., and FARTAJ, A., "Aerodynamic models for Darrieus-type straight-bladed vertical-axis wind turbines," *Renewable and Sustainable Energy Reviews* 12 (2008) pp. 1087-1109

[80] ISLAM, M., AMIN, M-R., TING, D. S-K, and FARTAJ, A., "Selection of airfoils for straight-bladed vertical-axis wind turbines based on desirable aerodynamic characteristics," *Proceedings of the ASME International Mechanical Engineering Congress and Exposition*, Boston, MA, 2008

[81] ISLAM, M., AMIN, M. R., CARRIVEAU, R., and FATAJ, A., "Investigation of low Reynolds number airfoils for fixed-pitch straight-bladed VAWT," *47th AIAA Aerospace Sciences Meeting Including the New Horizon Forum and Aerospace Exposition*, January 2009, Orlando, FL

[82] ISLAM, M., TING, S. K., and FARTAJ, A., "Design of a special-purpose airfoil for smaller-capacity straight-bladed VAWT," *Wind Engineering*, Vol. 31, No. 6, 2007, pp. 401-424

[83] ISLAM, M., TING, S. K., and FARTAJ, A., "Desirable airfoil features for small-capacity straight-bladed VAWT," *Wind Engineering*, Vol. 31, No. 3, 2007, pp. 165-196

[84] JOSELIN-HERBERT, G. M., INIYAN, S., SREENIVALSAN, E., and RAJAPANDIAN, S., "A review of wind energy technologies," *Renewable and Sustainable Energy Reviews*, Vol. 11, No. 6, August 2007, pp. 1117-1145

[85] KAMOJI, M. A., KEDARE, S. B., and PRABHU, S. V., "Performance test on helical Savonius rotor," *Renewable Energy*, Vol. 34, issue 3, March 2009, pp. 521-529

[86] KANG, S-H., SHIN, E-S., RYU, K-W., and LEE J-S., "Separation blockage-correction method for the airfoil of a wind turbine blade," *Journal of Mechanical Science and Technology*, 27 (5) (2013) 1321-1327

[87] KARTHIKEYAN, D., MCCROSKEY, W.J., and BAEDER, J.D., "Analysis of wind tunnel wall interference effects on subsonic unsteady airfoil flows," *Journal of Aircraft*, Vol. 44, No. 5, September-October 2007

[88] KHAN, M.J., BHUAYN, G., IQBAL, M.T., and QUAICOE, J.E., "Hydrokinetic energy conversion systems and assessment of horizontal- and vertical-axis turbines for river and tidal applications: a technology status review," *Applied Energy* 86 (2009) pp 1893-1835

[89] KLIMAS, P.C., "Darrieus Rotor Aerodynamics," *Journal of Solar Energy Engineering*, Vol. 104, May 1982

[90] KINZEL, M., MULLIGAN, Q., and DABIRI, J. O., "Energy exchange in an array of vertical-axis wind turbines," *Journal of Turbulence*, Vol. 13, No. 38, 2012, pp. 1–13

[91] KIRKE, B.K., "*Evaluation of Self-Starting Vertical-Axis Wind Turbines for Stand-Alone Applications*," PhD thesis, Griffith University, Australia, 1998

[92] KIWATA, T., YAMADA, T., KITA, T., TAKATA, S., KOMATSU, N., and KIMURA, S., "Performance of a vertical-axis wind turbine with variable-pitch straight blades utilizing a linkage mechanism," *Journal of Environment and Engineering*, Vol. 5, No. 1, 2010

[93] KJELLIN, J., BULOW, F., ERIKSSON, S., DEGLAIRE, LEIJON, M., and BERNHOFF, H., "Power coefficient measurement on a 12 kW straight bladed vertical-axis wind turbine," *Renewable Energy* 36 (2011) pp 3050-3053

[94] KJELLIN, J., "*Vertical-Axis Wind Turbines Electrical System and Experimental Results*," Ph.D. Dissertation, Uppsala University, Sweden 2012

[95] KUMAR, V., PARASCIVOIU, M., and PARASCHIVOIU, I., "Low Reynolds number vertical-axis wind turbine for Mars," *Wind Engineering*, Vol. 34, No. 4, pp. 461-476, 2010

[96] KUNZ, D. L, "*Unsteady Drag and Dynamic Stall as Simulated in Varying Freestream*," Ph.D. Thesis, School of Aerospace Engineering, Georgia Institute of Technology, March 1976

[97] KYOZUKA, Y., "An experimental study on the Darrieus-Savonius turbine for the tidal current power generation," *Journal of Fluid Science and Technology*, Vol. 3, No. 3, 2008

[98] LAIN, S., and OSORIO, C., "Simulation and evaluation of a straight-bladed Darrieus type cross flow marine turbine," *Journal of Scientific & Industrial Research*, Vol. 69, December 2010, pp. 906-912

[99] LANEVILLE, A., and VITTECOQ, P., "Effect of turbulence on dynamic stall," *Wind Turbine Aerodynamics Seminar*, Sandia National Laboratories, Albuquerque, NM, 1985

[100] LARSEN, J. W., NIELSEN, S. R. K., and KRENK, S., "Dynamic stall model for wind turbine airfoils," *Journal of Fluids and Structures*, Vol. 23, No. 7, October 2007, pp. 959–982

[101] LEISHMAN, J. G., BEDDOES, T. S., "A generalised model for airfoil unsteady aerodynamic behaviour and dynamic stall using the indicial method", *Proceedings of the 42nd Annual Forum of the American Helicopter Society*, Washington D.C. June 1986

[102] LEISHMAN, J. G., BEDDOES, T. S., "A semi-empirical model for dynamic stall," *Journal of the American Helicopter Society*, July 1989

[103] LI, Y., and CALISAL, S.M., "Three-dimensional effects and arm effects on modeling a vertical-axis tidal current turbine," *Renewable Energy*, 35 (2010) pp. 2325-2334

[104] LI, Y., and CALISAL, S. M., "Numerical analysis of the characteristics of vertical-axis tidal current turbines," *Renewable Energy* 35 (2010) pp. 435-442

[105] LI, Y., FENG, F., TIAN, W., and TAGAWA, K., "Numerical simulation on the static torque performance of vertical-axis wind turbine with different blade airfoils," *Applied Mechanics and Materials,* Vols. 84-85 (2011) pp. 702-705

[106] LI, S., and LI, Y., "Numerical study on the performance effect of solidity on the straight-bladed vertical-axis wind turbine," *Power and Energy Engineering Conference,* 2010

[107] LI, Y., TAGAWA, K., and LIU, W., "Wind tunnel test on a straight wing vertical-axis wind turbine with attachment on blade surface," *The Ontario Sustainable Energy Association,* 2008

[108] LI, C., ZHU, S., XU, Y. L., and XIAO, Y., "2.5D large eddy simulation of vertical-axis wind turbine in high angle of attack flow," *Renewable Energies*, Vol. 51, pp. 317-330, 2013

[109] LISSAMAN, P.B.S., "Some marketing and technical considerations of wind power," In Ljungstrom, O., editor, *Adanced Wind energy Systems*, Vol. 1, pp. 2-37, 1976

[110] LJUNGSTOM, O., "*New Concepts in Vertical-Axis Turbines (VAWT) and Applications to Large Multi-MW Size, Off-Shore Wind Turbine Systems*," FFA The Aeronautical Research Institute of Sweden, 1980

[111] MANANA, M., "Small wind energy systems. State of the art and new challenges," *Proceedings of the International Conference on the Renewable Energies and Power Quality,* Gran Canaria, Spain, 2011

[112] MANDAL, A. C., and BURTON, J. D., "The effect of dynamic stall and flow curvature on the aerodynamics of Darrieus turbines applying the cascade model," *Wind Engineering*, Vol. 18, No. 6, pp. 267-282, 1994

[113] MACPHEE, D., and BEYENE, A., "Recent advances in rotor design of vertical-axis wind turbines," *Wind Engineering*, Vol. 36, No. 6, 2012, pp. 647-666

[114] MASSE, B., "Description de deux programmes d'ordinateur pour le calcul des performances et des charges aérodynamiques pour les éoliennes à axe vertical," *IREQ*-2379, 1981

[115] MASSON, C., LECLERC, C., and PARASCHIVOIU, I., "Appropriate dynamic-stall models for performance predictions of VAWTs with NFL blades," *International Journal of Rotating Machinery*, 1998, Vol. 4, No. 2, pp. 129-139

[116] McGLUMPHY, J., "*Numerical Investigation of Subsonic Axial-Flow Tandem Airfoils foe a Core Compressor Rotor*," PhD Dissertation, Virginia Polytechnic Institute and State University, Blacksburg, VA, January 2008

[117] McCROSKEY, W-J., CARR L-W., and McALISTER, K-W., "Dynamic stall experiments on oscillating airfoils," *AIAA Journa*l, Vol. 14, No. 1, January 1976

[118] McLAREN, K., TULLIS, S., and ZIADA, S., "CFD simulation of dynamic thrust and radial forces on a vertical-axis wind turbine blade," *15th Annual Conference of the CFD Society of Canada*, Toronto, ON, Canada, 2007

[119] McLAREN, K., TULLIS, S., and ZIADA, S., "Computational fluid dynamics simulation of the aerodynamics of a high solidity, small-scale vertical-axis wind turbine," *Wind Energy*, Vol. 15, 2012, pp. 349-361

[120] MENTER, F. R., "Zonal two-equation k-ω turbulence models for aerodynamic flows," *AIAA Paper* 93-2906, 1993

[121] MENTER, F. R., "Two-equation eddy-viscosity turbulence models for engineering applications," *AIAA Journal*, Vol. 32, No. 8, pp. 1598-1605, 1994

[122] MERTENS, S., van KUIK, G., and van BUSSEL, G., "Performance of an H-Darrieus in the skewed flow on a roof," *Journal of Solar Energy Engineering*, Vol. 125, November 2003

[123] MUHAMED, M. H., JANIGA, G., PAP, E., and THEVENIN, D., "Optimization of Savonius turbines using an obstacle shielding the returning blade," *Renewable Energy*, Vol. 35, No. 11, November 2010, pp. 2618-2626

[124] MUKHERJEE, S., and ROY, S., "Enhancement of lift and drag characteristics of an oscillating airfoil in deep dynamic stall using plasma actuation," *AIAA_ASM* 2012

[125] NEWMAN, B. G., "Multiple actuator disc theory for wind turbines," *Journal of Wind Engineering and Industrial Aerodynamics*, Vol. 24, issue 3, 1986, pp.215-225

[126] OLER, J.W., STRICKLAND, J.H., IM, B.J., and GRAHAM, G.H., "*Dynamic Stall Regulation of the Darrieus Turbine*," SANDIA Report SAND83-7029

[127] OMIJEH, B.O., NMOM, C.S., and NLEWEM, E., (2013), "Modeling of a vertical-axis wind turbine with permanent magnet synchronous generator for Nigeria international," *Journal of Engineering and Technology*, Vol. 3 No. 2, February, 2013

[128] OSTERBERG, D., "*Multi-Body Unsteady Aerodynamics in 2D Applied to a Vertical-Axis Wind Turbine Using a Vortex Method*," Thesis, Uppsala University October 2010

[129] OULD BILAL, B., NDONGO, M., KEBE, C. M. F., SAMBOU, V., and NDIAYE, P. A., "Feasibility study of wind energy potential for electricity generation in the northern coast of Senegal," *Energy Procedia*, Vol. 36, pp 1119-1129, 2013

[130] PAILLARD, B., ASTOLFI, J. A., and HAUVILLE, F. "CFD simulation and experimental validation of a vertical-axis turbine: toward variable pitch cross-flow marine turbine for maximizing hydropower extraction, the Shiva project," *Proceedings of the ASME 2011 30th International Conference on Ocean, Offshore and Arctic Engineering OMAE2011*, June 19-24, 2011, Rotterdam, The Netherlands

[131] PANDA J., and ZAMAN, K. B. M. Q., "Experimental investigation of the flowfield of an oscillating airfoil" *NASA Technical Memorandum 105675, 10th Applied Aerodynamics Conference sponsored by the American Institute of Aeronautics and Astronautics*, Palo Alto, California, June 22-24, 1992

[132] PANTAKAR, S. V., and SPALDING, D. B., "A calculation procedure for heat, mass and momentum transfer in three-dimensional parabolic flows," *International Journal of Heat and Mass Transfer*, Vol. 15, No. 10, 1972 pp. 1787-1806

[133] PARASCHIVOIU, I., "Aerodynamic loads and performance of the Darrieus rotor," *J. Energy*, Vol. 6, No. 6, 1981

[134] PARASHIVIOU, I., "Aerodynamic loads and performance of Darrieus rotor," *AIAA Paper 81-2582R, 2nd AIAA Terrestrial Energy Systems Conference*, Dec. 1981, Colorado Springs, CO.

[135] PARASCHIVOIU, I., "Predicted and experimental aerodynamic forces on the Darrieus rotor," *J. Energy*, Vol. 7, No. 6, 1983

[136] PARASHIVIOU, I., DELCAUX, F., "Double multiple streamtube model with recent improvement," *Journal of Energy*, Vol. 7, No 3, 1982, pp. 250-254.

[137] PARASHIVIOU, I., "Double multiple streamtube model for studying vertical-axis wind turbines," *Journal of Propulsion*, Vol. 4, No. 4, 1988, pp. 370-377.

[138] PARASHIVIOU, I., "Wind turbine design: with emphasis on Darrieus concept," *Polytechnic International Press*, 2002

[139] PARASCHIVOIU, I., TRIFU, O., and SAEED, F., "H_Darrieus wind turbine with blade pitch control," *International Journal of Rotating Machinery*, 2009-505343

[140] PARASCHIVOIU, I., FRAUNIE, P., and BEGUIER, C., "Streamtube expansion effect on the Darrieus wind turbine," *Journal of Propulsion and Power*, Vol. 1, No. 2, 1985

[141] PATEL, B., and KEVAT, V., "Performance prediction of straight bladed Darrieus wind turbine by single streamtube model," *International Journal of Advanced Engineering Technology*, Vol. 4, No. 2, April-June 2013

[142] PETOT, D., and LOISEAU, H., "*Successive Smoothing Algorithm for Constructing the Semi-Empirical Model Developed at ONERA to Predict Unsteady Aerodynamic Forces*," NASA Technical Memorandum TM-76681, 1982

[143] POPE, K., DINCER, I., and NATERER, G. F., "Energy and exergy efficiency comparison of horizontal- and vertical-axis wind turbines," *Renewable Energy*, Vol. 35, No. 9, September 2010, pp. 2102-2113

[144] QU, J., MEI, Y., and XU, M., "Investigation on performance influence of maximum thickness position on a vertical-axis wind turbine airfoil," 978-1-4244-6255-1/11, 2011 IEEE

[145] RACITI CASTELLI, M., ENGLARO, A., and BENINI, E., "The Darrieus wind turbine: proposal for a new performance prediction model based on CFD," *Energy* 36 (2011) pp. 4919-4934

[146] RAGHEB, A., and SELIG, M.S., "Multi-element airfoil configurations for wind turbines," *28th AIAA Applied Aerodynamics Conference*, 27-30 June 2013, Honolulu, HI AIAA-2013-3971

[147] RATHI, D., "*Performance Prediction and Dynamic Model Analysis of Vertical-Axis Wind Turbine Blades with Aerodynamically Varied Blade Pitch*," MS Thesis, North Carolina State University, Raleigh, NC, 2012

[148] REUSS RAMSAY, R., and GREGOREK, G.M., "*Effects of Grit Roughness and Pitch Oscillations on the S824 Airfoil*," The Ohio State University, October 1998

[149] RHIE, C. M., and CHOW, W. L., "Numerical study of the turbulent flow past an airfoil with trailing edge separation," *AIAA Journal*, Vol. 10, No. 11, November 1983 pp. 1525-1532

[150] RIVAL, D., DRUMOND, J., and TROPEA, C., "Lift augmentation for two pitching and plunging airfoils in tandem formation," *46th AIAA Aerospace Sciences Meeting and Exhibit* (AIAA 2008-1441) 7-10 January 2008, Reno NV

[151] RUEGER, M.L., and GREGOREK, G.M., "*An Experimental Investigation of the Effect of Vortex Generator on the Aerodynamic Characteristics of a NACA 0021 Airfoil Undergoing Large Amplitude Pitch Oscillations*," Sandia National Laboratories, SAND90-7111, April 1991

[152] SAEED, F., PARASCHIVOIU, I., TRIFU, O., HESS, M., and GABRYS, C., "Inverse airfoil design method for low-speed straight-bladed Darrieus type VAWT applications," *Wind Engineering*, Vol. 35, pp. 357-368, 2011

[153] SABAEIFARD, P., RAZZAGHI, H., and FOROUZANDEH, A., "Determination of vertical-axis wind turbines optimal configuration through CFD simulations," *2012 International Conference on Future Environment and Energy ICPBEE*, Vol. 28 (2012)

[154] SAEIDI, D., SEDAGHAT, A., ALAMDART, P., and ALEMRAJABI, A. A., "Aerodynamic design and economical evaluation of site specific small scale vertical-axis wind turbines," *Applied Energy*, 101 (2013) pp. 765-775

[155] SAHIN M., SANKAR L., CHANDRASEKHRA, M.S. and TUNG C., "Dynamic stall alleviation using a deformable leading edge concept - a numerical study", *AIAA Journal of Aircraft*, 40 (1), 2003, pp.77-85.

[156] SCHEURISH, F., FLETCHER, T. M., and BROWN, R. E., "Effect of blade geometry on the aerodynamic loads produced by vertical-axis wind turbines," *Proceedings of the Institution of Mechanical Engineers*, Vol. 225 Part A: J. Power and Energy, 2011

[157] SCHLERNITZAUER, J., VIGNERON, B., and RONAYNE, A., "*Clean Development Mechanism: Taiba N'Diaye Wind Energy Project*," United Nations Framework Convention on Climate Change, 2011

[158] SELIG, M. S., DONOVAN, J. F., and FRASER D. B., "Airfoils at Low speed," 1989, *H.A Stokely, Publisher*

[159] SELIG, M.S., and MCGRANAHAN, B.D., "*Wind Tunnel Aerodynamic Tests of Six Airfoils for Use on Small Wind Turbines*," NREL Report NREL/SR-500-34515, 2004

[160] SHAMSODDIN, S., and PORTE-AGEL, F., "Large eddy simulation of vertical-axis wind turbine wakes," *Energies*, Vol. 7, pp. 890-912, 2014

[161] SHANKARAN, S., "*Numerical Analysis and Design of Upwind Sails*," PhD. Dissertation, Stanford University, April 2005

[162] SHARMA, D.M., and PODDAR, K., "Investigation of dynamic stall characteristics for flow past an oscillating airfoil at various reduced frequencies by simultaneous PIV and surface pressure measurements," *10th International Symposium on Particle Image Velocimetry – PIV13*, Delft, The Netherlands, July 1-3, 2013

[163] SHELDAHL, R.E., and KLIMAS, P.C., "*Aerodynamic Characteristics of Seven Symmetrical Airfoil Sections through 180-Degree Angle of Attack for Use in Aerodynamic Analysis of Vertical-Axis Wind Turbines*," SANDIA Report, SAND80-2114

[164] SHENG, W., McD. GALBRAITH, R. A., and COTON, F. N., "Improved dynamic-stall-onset criterion at low Mach numbers," *Journal of Aircraft*, Vol. 44, No. 3, 2007

[165] SHENG, W., GALBRAITH, R. A. McD., and COTON, F. N., "A modified dynamic stall model for low Reynolds numbers," *Journal of Solar Energy Engineering*, Vol. 130, August 2008

[166] SHIONO, M., SUZUKI, K., and KIHO, S., "Output characteristics of Darrieus turbine with helical blades for tidal current generations," *Proceedings of the 12th International Offshore and Polar Engineering Conference*, Kitakyushu, Japan, May 26031, 2002

[167] SHIONO, M., SUZUKI, K., and KIHO, S., "An experimental study of the characteristics of a Darrieus turbine for tidal power generation," *Electrical Engineering in Japan*, Vol. 132, No. 3, 2000, pp. 38-47

[168] SHIRES, A., "Development and evaluation of an aerodynamic model for a novel vertical-axis wind turbine concept," *Energies* 2013, 6, pp. 2501-2520

[169] SHIRSATH, R. A., and MUKHERJEE R., "Unsteady aerodynamics of tandem airfoils pitching in phase," *Proceedings of the 2nd International Conference on Mechanical, Production and Automobile Engineering (ICMPAE'2012)*, Singapore April 28-29, 2012

[170] SHIRSATH, R. A., AZIZ, H., and MUKHERJEE R., "A Numerical study of tandem pitching airfoils," *51st AIAA Aerospace Sciences Meeting including the New Horizons Forum and Aerospace Exposition*, 07 - 10 January 2013, Grapevine (Dallas/Ft. Worth Region), Texas

[171] SIMAO FERREIRA, C.J, van BUSSEL, G.J.W., and van KUIK, G.A.M., "Wind tunnel hotwire measurements, flow visualization and thrust measurement of a VAWT in skew," *Journal of Solar Energy Engineering*, Vol. 128, November 2006

[172] SIMAO FERREIRA,C.J., van BUSSEL, G., and van KUIK, G.A.M., "An analytical method to predict the variation in performance of a H-Darrieus in skewed flow and its experimental validation," *Proceedings of the European Wind Energy Conference,* Athens, Greece, 2006

[173] SIMAO FERREIRA, C.J., SCARANO, F., van KUIK, G., and van BUSSEL G., "Aerodynamic force on a VAWT in dynamic stall by integration of the velocity field from 3D particle image velocimetry," *European Academy for Wind Energy*, 2007

[174] SIMAO FERREIRA, C.J., BIJL, H., van BUSSEL, G., and van KUIK, G., "Simulating dynamic stall in a 2D VAWT: modeling strategy, verification and validation with particle image velocimetry data," *The Science of Making Torque from Wind; Journal of Physics: Conference Series* 75 (2007)

[175] SIMAO FERREIRA, C. J., "*The Near Wake of the VAWT: 2D and 3D Views of the VAWT Aerodynamics*", Ph.D. Dissertation, Delft Technical University, Delft, The Netherlands, 2009

[176] SIMAO-FERREIRA, C., AAGAARD MADSEN, H. A., BARONE, M., ROSCHER, B., DEGLAIRE, P., and ARDUIN, I., "Comparison of aerodynamic models for vertical-axis wind turbines," *The Science of Making Torque from Wind 2014, Journal of Physics Conference Series* 524 (012125)

[177] SLOOTWEG, J.G., POLINDER, H., and KLING, W.L., "Representing wind turbine electrical generating systems in fundamental frequency simulations," *IEEE Transactions on Energy Conversion*, Vol. 18, No. 4, December 2003

[178] SOLUM, A., DEGLAIRE, P. ERIKSSON, S., STALBERG, M., LEIJON, M., and BERNHOFF, H., "Design of a 12 kW vertical-axis wind turbine equipped with a direct driven PM synchronous generator," *European Wind Energy Conference*, Athens, Greece, 2006

[179] SORAGHAN, C-E., LEITHEAD, W-E., YUE, H., and FEUCHTWANG, J., "Double multiple streamtube model for variable pitch vertical-axis wind turbines," *31st AIAA Applied Aerodynamics Conference*, San Diego, 2013

[180] STAELENS, Y., SAEED, F., and PARASHIVIOU, I., "A straight-bladed variable-pitch VAWT concept for improved power generation," *AIAA Paper 2003-0524, 22nd ASME Wind Energy Symposium held in conjunction with the 41st Aerospace Sciences Meeting & Exhibit*, Jan. 2003, Reno, NV.

[181] STRICKLAND, J. H., "*The Darrieus Turbine: A Performance Prediction Model Using Multiple Streamtube,"* Sandia Laboratories, SAND75-0431, October 1975

[182] STICKLAND, J. H., WEBSTER, B. T., and NGUYEN, T., "A vortex model of the Darrieus turbine: an analytical and experimental study," *Journal of Fluids Engineering*, Vol. 101, issue 4, 1979

[183] TAKAO, M., TAKITA, H., SAITO, Y., MAEDA, T., KAMADA, Y., and TOSHIMITSU, K., "Experimental study of a straight-bladed vertical-axis wind turbine with a directed guide vane row," *Proceedings of the ASME 2009 28th International Conference on Ocean, Offshore and Artic Engineering*, OMAE2009, May 31 – June 5, 2009, Honolulu, HI

[184] TATINEMI, M., and ZHONG, X., "Numerical simulation of unsteady low-Reynolds-number separated flows over airfoils," *AIAA Journal*, Vol. 38, No. 7: Technical Notes, 2000

[185] TEMPLIN, R. J., "*Aerodynamic Performance Theory for NRC Vertical-Axis Wind Turbine*," National research Council of Canada, LTR-160, 1974

[186] *The ANSYS Fluent® Theory Guide*. Release 14.5, October 2012

[187] TONGCHTPAKDEE, C., BENJANIRAT, S., and SANKAR, L., "Numerical simulation of the aerodynamics of horizontal- axis wind turbines under yaw conditions," *Journal of Solar Energy*, Vol. 127, 2005.

[188] TONGCHTPAKDEE, C., BENJANIRAT, S., and SANKAR, L., "Numerical studies of the effects of active and passive circulation enhancement concepts on wind Turbine performance," *Journal of Solar Energy Eng*. 128 432, 2006

[189] TOTA-MAHARAJ, K., RAMKISSOON, R., and MANOHAR, K., "Economical Darrieus straight bladed vertical-axis wind turbine for renewable energy applications," *Journal of the Energy Institute*, Vol. 85, No. 3, pp. 156-162, 2012

[190] TRAN, C. T., and PETOT, D., "Semi-empirical model for the dynamic stall of airfoils in view of the application to the calculation of responses of a helicopter blade in forward flight," *Vertica*, Vol. 5, No. 1, 1981, pp. 35-53 (Also available in ONERA TP No. 1980-103, 1980)

[191] TROLDBORG, N., BAK, C., SORENSEN, N.N., MADESN, H.A., RETHORE, P-E., and ZAHLE, F., "Experimental and numerical investigation of 3D aerofoil characteristics on a MW wind turbine," *Proceedings of the 2013 European Wind Energy Association Annual Event*

[192] TUNCER, I-H., and PLATZER, M-F., "Computational study of flapping airfoil aerodynamics," *Journal of Aircraft*, Vol. 37, No.3 May-June 2000

[193] TUNCER, I. H. and SANKAR, L. N., "Unsteady aerodynamic characteristics of a dual-element airfoil," *Journal of Aircraft*, Vol. 31, No. 3, May-June 1994

[194] TUNCER, I.H., WALZ, R., and PLATZER, M.F., "A computational study on the dynamic stall of a flapping airfoil," AIAA 98-2519

[195] TVEITERAS, V., "*Numerical Study of the Interaction of Flow over Two Airfoils in Relative Motion*," Master of Science in Physics and Mathematics, Norwegian University of Science and Technology, June 2011

[196] VISBAL, M.R., SHANG, J.S., "Investigation of flow structure around a rapidly pitching airfoil," *AIAA Journal*, Vol. 27, No. 8, August 1989

[197] WAHL, M., "*Designing an H-rotor type Wind Turbine for Operation on Amundsen-Scott South Pole Station*," Thesis Uppsala University, December 2007

[198] WAKUI, T., TANZAWA, Y., HASHIZUME, T., and NAGAO, T., "Hybrid configuration of Darrieus and Savonius rotors for stand-alone wind turbine-generator systems," *Electrical Engineering in Japan*, Vol. 150, No. 4, pp. 13-22, March 2005

[199] WANG, S., INGHAM, D.B., MA, L., POURKASHANIAN, M.M and TAO, Z., "Numerical investigations on dynamic stall of low Reynolds number flow around oscillating airfoils," *Computers & Fluids* (2010) pp. 1529-1451

[200] WASYNCZUK, O., MAN, D. T., and SULLIVAN, J. P., "Dynamic behavior of a class of wind turbine generators during random wind fluctuations," *IEEE Transactions on Power Apparatus and Systems*, Vol. PAS-100, No. 6, June 1981

[201] WEEKES, S.M., and TOMLIN, A.S., "Evaluation of a semi-empirical model for predicting the wind energy resource relevant to small-scale wind turbines," *Renewable Energy*, 50 (2013) pp. 280-288

[202] WHITTLESEY, R. W., LISKA, S., and DABIRI, J. O., "Fish schooling as a basis for vertical-axis wind turbine farm design," *Bioinspiration & Biomimetics*, Vol. 5, 2010

[203] WILLIAMSON, G. A., "*Experimental Wind Tunnel Study of Airfoils with Large Flap Deflections at Low Reynolds Numbers*," MS Thesis, University of Illinois at Urbana-Champaign, 2012

[204] WILSON R. E., and LISSAMAN, P. B. S., "*Applied Aerodynamics of Wind Turbines*," Oregon State University, 1974

[205] WILSON, R. "Wind turbine aerodynamics," *Journal of Wind Engineering and Industrial Aerodynamics*, Vol. 5, No. 3-4, pp. 357-372, 1980

[206] WISON, D. G., "*Horizontal-Axis Wind Turbine*," US Patent 20130015666 A1, 2013

[207] WOLFE, W.P., and OCHS, S.S., "*Predicting Aerodynamic Characteristics of Typical Wind Turbine Airfoils Using CFD*," SANDIA Report SAND96-2345

[208] WORSTELL, M. H., "*Aerodynamic Performance of the 17 Meter Diameter Darrieus Wind Turbine*," Sandia Report SAND78-1737, 1978

[209] XU, G., and SANKAR, L., "Effects of transition, turbulence and yaw on the performance of horizontal- axis wind turbines," *AIAA Paper* 2000-0048.

[210] XU, G., and SANKAR, L., "Computational study of horizontal- axis turbines" *J. of Solar Energy Engineering*, Vol. 122, No. 1, Feb. 2002, pp. 35-39.

[211] XU, G., and SANKAR, L., "Application of a viscous flow methodology to NREL phase VI wind turbine", *J. of Wind Engineering*, 2002.

[212] YLILAMMI, N., "*Experimental and Computational Study of two Flapped Airfoils at Low Reynolds Numbers*," MS Thesis, Helsinki University of technology, Espoo, March 2009

[213] YOSHIDA, S., "*Horizontal-Axis Wind Turbine*," US Patent 8647060 B2, 2008

[214] YOSHIDA, S., "*Horizontal-Axis Wind Turbine*," US Patent 7365447 B2, 2014

[215] YOUM, I., SARR, J., SALL, M., NDIAYE, A., and KANE, M. M., "Analysis of wind data and wind energy potential along the northern coast of Senegal," *Revue des Energies Renouvelables,* Vol. 8, No. 2, pp. 95-108, December 2005

[216] ZANON, A., GIANNATTASIO, P., and SIMAO FERREIRA, C.J., "A vortex panel model for the simulation of the wake flow pasta vertical-axis wind turbine in dynamic stall," *Wind Energy,* Vol. 16, No 5, pp. 661-680, July 2013

[217] ZHANG, L.X., LIANG, Y.B., LIU, X.H., JIAO, Q.F., and GUO, J., "Aerodynamic performance prediction of straight-bladed vertical-axis wind turbine based on CFD," *Advanced Mechanical Engineering,* Vol. 2013 ID.905379

[218] BCEAO, "*Note d'analyse sur les conditions de financement bancaire de l'habitat dans les pays de 'UEMOA*," Octobre 2014

VITA

ELHADJI ALPHA A. BAH

Elhadji Alpha Amadou was born in Dakar, Senegal to Elhadji Alhassane and Fatoumata Binta BAH. [My Lord, have Mercy on the both of them as they brought me with utmost love and care when I was little]. He grew up in Toubbou, Timbi-Tounni, Pita, Guinea where he attend the primary school of Wansan. He continued his education in Dakar, Senegal where he attended middle and high school at Papa Gueye FALL and Lamine GUEYE, respectively. He started his undergraduate curriculum with the Classes Preparatoroires aux Grandes Ecoles at Lycee Montesquieu, Le Mans, France with major in Physics and Chemistry and Mathematics as secondary major. He was admitted to Engineering school at the Ecole Nationale Superieure de Mecanique et d'Aerotechnique (ENSMA) and received his Engineering Diploma in 2008. He later joined the Georgia Institute of Technology where he graduated with an M.S in Aerospace Engineering in 2011 and is pursuing doctoral studies in the same field. He has regularly completed Jobs and internships alongside the academic work. When he is not working and even while working, Elhadji Alpha likes to reflect on the magnificence of the creation for the mind of ours cannot grasp the Magnificence of the Creator.